NASA/TP—2013–216518

Method for Estimating Operational Loads on Aerospace Structures Using Span-wisely Distributed Surface Strains

William L. Ko and Van Tran Fleischer
Dryden Flight Research Center, Edwards, California

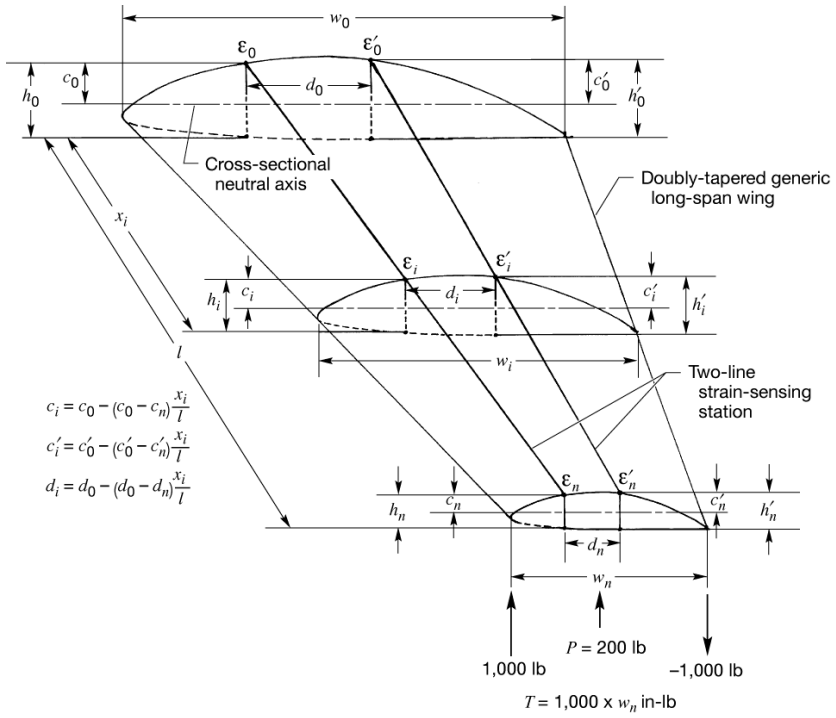

April 2013

NASA STI Program ... in Profile

Since its founding, NASA has been dedicated to the advancement of aeronautics and space science. The NASA scientific and technical information (STI) program plays a key part in helping NASA maintain this important role.

The NASA STI program operates under the auspices of the Agency Chief Information Officer. It collects, organizes, provides for archiving, and disseminates NASA's STI. The NASA STI program provides access to the NASA Aeronautics and Space Database and its public interface, the NASA Technical Reports Server, thus providing one of the largest collections of aeronautical and space science STI in the world. Results are published in both non-NASA channels and by NASA in the NASA STI Report Series, which includes the following report types:

- TECHNICAL PUBLICATION. Reports of completed research or a major significant phase of research that present the results of NASA Programs and include extensive data or theoretical analysis. Includes compilations of significant scientific and technical data and information deemed to be of continuing reference value. NASA counter-part of peer-reviewed formal professional papers but has less stringent limitations on manuscript length and extent of graphic presentations.

- TECHNICAL MEMORANDUM. Scientific and technical findings that are preliminary or of specialized interest, e.g., quick release reports, working papers, and bibliographies that contain minimal annotation. Does not contain extensive analysis.

- CONTRACTOR REPORT. Scientific and technical findings by NASA-sponsored contractors and grantees.

- CONFERENCE PUBLICATION. Collected papers from scientific and technical conferences, symposia, seminars, or other meetings sponsored or co-sponsored by NASA.

- SPECIAL PUBLICATION. Scientific, technical, or historical information from NASA programs, projects, and missions, often concerned with subjects having substantial public interest.

- TECHNICAL TRANSLATION. English-language translations of foreign scientific and technical material pertinent to NASA's mission.

Specialized services also include organizing and publishing research results, distributing specialized research announcements and feeds, providing information desk and personal search support, and enabling data exchange services.

For more information about the NASA STI program, see the following:

- Access the NASA STI program home page at http://www.sti.nasa.gov

- E-mail your question to help@sti.nasa.gov

- Fax your question to the NASA STI Information Desk at 443-757-5803

- Phone the NASA STI Information Desk at 443-757-5802

- Write to:
  STI Information Desk
  NASA Center for AeroSpace Information
  7115 Standard Drive
  Hanover, MD 21076-1320

NASA/TP—2013–216518

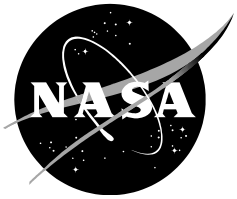

Method for Estimating Operational Loads on Aerospace Structures Using Span-wisely Distributed Surface Strains

William L. Ko and Van Tran Fleischer
Dryden Flight Research Center, Edwards, California

National Aeronautics and
Space Administration

Dryden Flight Research Center
Edwards, CA 93523-0273

April 2013

Patent Notice

The method for structure operational load estimations using distributed surface strains described in this technical paper is protected under **"*Process for Using Surface Strain Measurements to Obtain Operational Loads for Complex Structures*"**, U.S. Patent No. 7,715,994, issued May 11, 2010. Therefore, those interested in using the invention should contact the NASA Innovative Partnership Program Office at the Dryden Flight Research Center for more information.

Available from:

NASA Center for AeroSpace Information
7115 Standard Drive
Hanover, MD 21076-1320
443-757-5802

TABLE OF CONTENTS

ABSTRACT

This report presents a new method for estimating operational loads (bending moments, shear loads, and torques) acting on slender aerospace structures using distributed surface strains (unidirectional strains). The surface strain-sensing stations are to be evenly distributed along each span-wise strain-sensing line. A depth-wise cross section of the structure along each strain-sensing line can then be considered as an imaginary embedded beam. The embedded beam was first evenly divided into multiple small domains with domain junctures matching the strain-sensing stations. The new method is comprised of two steps. The first step is to determine the structure stiffness (bending or torsion) using surface strains obtained from a simple bending (or torsion) loading case, for which the applied bending moment (or torque) is known. The second step is to use the strain-determined structural stiffness (bending or torsion), and a new set of surface strains induced by any other loading case to calculate the associated operational loads (bending moments, shear loads, or torques). Performance of the new method for estimating operational loads was studied in light of finite-element analyses of several example structures subjected to different loading conditions. The new method for estimating operational loads was found to be fairly accurate, and is very promising for applications to the flight load monitoring of flying vehicles with slender wings.

NOMENCLATURE

c	depth factor (vertical distance from neutral surface to outermost fiber of bottom surface of uniform beam), in
$c(x)$	depth factor (vertical distance from neutral surface to bottom surface outermost fiber of nonuniform beam) at axial location, x, in
c_i	$\equiv c\ (x_i)$, value of $c\ (x)$ at strain-sensing station, x_i, in
c_0	value of c_i at fixed end (wing root), $x = x_0 = 0$, in
c_n	value of c_i at free end (wing tip), $x = x_n = l$, in
d_i	separation distance of front and rear strain sensors for $\{\varepsilon_i, \varepsilon_i'\}$ at $x = x_i$
d_n	value of d_i at wing tip, $x = x_n = l$, in
d_0	value of d_i at wing root, $x = x_0 = 0$, in
E	Young's modulus, lb/in^2
$(EI)_i$	bending stiffness at strain-sensing station, x_i, lb-in^2
F_i	resultant force of distributed load lying outboard of wing cross section at $x = x_i$, lb
G	shear modulus, lb/in^2
$(GK)_i$	torsional stiffness of the i-th domain lying between two adjacent strain-sensing stations $\{x_{i-1}, x_i\}$, lb-in^2
$(GK)_i^N$	torsional stiffness referred to x_N-axis system, lb-in^2
h_n	wing tip depth at front strain-sensing line, in
h_0	wing root depth at front strain-sensing line, in
I	moment of inertia, in^4
i	= 0,1,2,3....,n, strain sensor identification number
j	dummy index
J	polar moment of inertia, in^4
K	twisting moment of inertia ($K = J$, polar moment of inertia for circular cross section), in^4
l	length of slender structure, in
$M(x)$	bending moment at axial location, x, in-lb
M_i	$\equiv M\ (x_i)$, bending moment at strain-sensing station, x_i , in-lb
M_i^{P+T}	bending moment at strain-sensing station, x_i, induced by bending and torsion, in-lb
M_i^P	bending moment at strain-sensing station, x_i, induced by bending only, in-lb

M_i^T bending moment at strain-sensing station, x_i, induced by torsion only, in-lb
n index for the last span-wise strain-sensing station (or discretized domain number)
P applied point load, lb
P_i operational shear load at strain-sensing station, x_i, lb
P_i^{P+T} total shear load at strain-sensing station, x_i, induced by bending and torsion, lb
P_i^P shear load at strain-sensing station, x_i, induced by bending only, lb
P_i^T shear load at strain-sensing station, x_i, induced by torsion only, lb
T applied torque, in-lb
T_i torque at strain-sensing station, x_i, in-lb
T_i^{P+T} torque at strain-sensing station, x_i, induced by combined bending and torsion, in-lb
T_i^P bending-induced torque at strain-sensing-station, x_i, in-lb
T_i^T torsion-induced operational torque at strain-sensing station, x_i, in-lb
t wall thickness, in
w_i width of wing box at strain-sensing station, x_i, in
w_n wing tip chord length (width), in
w_0 wing root chord length (width), in
x, y Cartesian coordinates (x in beam axial direction, y in lateral direction), in
x_i axial coordinate of i-th strain sensor (called strain-sensing station), in
$y(x)$ beam deflection in y direction at axial location, x, in
y_i $\equiv y(x_i)$, value of $y(x)$ at strain-sensing station, x_i, in
Δl $= (x_i - x_{i-1}) = l/n$, domain length [distance between two adjacent strain-sensing stations, $\{x_{i-1}, x_i\}$], in
β swept angle of wing-box front edge, deg
ε_i $\equiv \varepsilon(x_i)$, value of $\varepsilon(x)$ at strain-sensing station x_i, in/in
$\bar{\varepsilon}_i$ $\equiv (\varepsilon_i + \varepsilon_i')/2$, averaged surface strain at strain-sensing station x_i, in/in
$\bar{\varepsilon}_i^{P+T}$ value of $\bar{\varepsilon}_i$ associated with combined bending and torsion loading, in/in
$\bar{\varepsilon}_i^T$ value of $\bar{\varepsilon}_i$ associated torsion loading only, in/in
θ slope of embedded beam, rad or deg
ν Poisson's ratio
ϕ_i cross sectional twist angle at axial location, $x = x_i$ rad or deg
ϕ_i^{P+T} cross-sectional twist angle at axial location, $x = x_i$, due to combined bending and torsion, rad or deg.
ϕ_i^P cross-sectional twist angle at axial location, $x = x_i$, due to bending only, rad or deg
ϕ_i^T cross-sectional twist angle at axial location, $x = x_i$, due to torsion only, rad or deg
σ_i surface stress associated with surface strain, ε_i, lb/in^2
$(\ )'$ quantity associated with rear strain-sensing line

INTRODUCTION

The strain sensors (for example, conventional strain gages or fiber optic sensors) installed on the surface of a structure (for example, aircraft wings), can only sense the surface strains, and cannot sense the out-of-plane deflections and cross-sectional rotation of a structure. However, after the formulations of the Displacement Transfer Functions (refs. 1–9), one can now convert the surface strains (unidirectional bending strains) into out-of-plane deflections for mapping out the overall structure deformed shapes for visual display. The displacement theory, combined with any strain-sensing system, thus created a revolutionary powerful new structure deformed shape-sensing technology, "Method of Real-Time Structure Shape-Sensing" [U.S. Patent No. 7,520,176, (ref. 10)], which is very attractive for applications

to the in-flight structure deformed shape monitoring of unmanned and manned flight vehicles, and other aerospace structures.

For flight vehicles, the structure operational load estimations are as important as the structure deformed shape predictions. The flight loads can come from air loads and inertia loads, and the deformation is the response to external loads based on cross-sectional stiffness, which in turn is a function of mass, moment of inertia, and material properties.

Similar to the structure deformed shape calculations, the span-wisely distributed surface strains can also be used to calculate operational loads (bending moments, shear loads, and torques) acting on complex slender structures (for example, high-aspect-ratio aircraft wings). This new method is called, "Process for Using Surface Strain Measurements to Obtain Operational Loads for Complex Structures" [U.S. Patent No 7,715,994, (ref. 11)]. To apply this new method to estimate operational loads, structural stiffness (bending and torsion) must be determine first.

For nonuniform cantilever slender structures such as high-aspect-ratio aircraft wings with complex internal structural configurations, the structural stiffness varies in the span-wise direction. One method to determine the structural stiffness is to perform finite-element analysis of the structure. Because of internal structural complexity (for example, aircraft wings), it is extremely cumbersome and time-consuming to generate an accurate finite-element model for the calculations of stiffness at multiple span-wise locations. Keep in mind that finite-element analysis is conventionally used for classical load calibrations and finding the load paths.

An alternative simple way to determine the structural stiffness (bending or torsion) is to conduct a simple bending (or torsion) test, and use the induced surface strains (obtained at span-wisely distributed strain-sensing stations) to calculate the structural stiffness at each strain-sensing station. Once the bending and torsion stiffness are determined, one can then use those strain-determined stiffness and a new set of surface strains, induced by another type of loading condition, to calculate the associated operational loads (bending moments, shear loads, and torques) at all the strain-sensing stations for mapping out the overall operational load profile.

This report describes the new method for estimating the operational loads (bending moments, shear loads, and torques) acting on slender structures (beam-like structures) using span-wisely distributed surface strains. Several slender structures were chosen to demonstrate the new method. The structures considered were: 1) tapered cantilever tubular beam; 2) depth-tapered un-swept wing box; 3) depth-tapered swept wing box; and 4) doubly-tapered generic long-span wing. The new method of estimating the operational load was found to be reasonably accurate, and is very promising for applications to flight load monitoring of flying vehicles with slender wings.

STRUCTURE DISCRETIZATION

To use the distributed surface strains (unidirectional strains) to estimate structural operational loads (moments, shear loads, and torques), the strain-sensing stations are to be evenly distributed in the span-wise direction of a slender structure (fig. 1). A line along which the strain-sensing stations are to be distributed is called a strain-sensing line (fig. 1). A narrow strip of structure beneath each surface strain-sensing line can then be considered as an imaginary embedded beam. In developing the stiffness transfer functions and load transfer functions, the embedded beam was first evenly divided into multiple small domains, with domain junctures matching the strain-sensing stations.

The surface strains can be obtained from the conventional strain sensors, from fiber optic strain-sensors (light weight), or generated from finite-element analysis. In the earlier finite-element shape

predictions of Ikhana wings [360-inch long per wing, (ref. 4)], a two-line strain-sensing system was used for each wing. Using only nine strain-sensing stations for each strain-sensing line, quite accurate deformed-shape predictions could be achieved (ref. 4). If the conventional strain gages are used, the lead-wires for just 18 strain gages per wing are unlikely to add significant weight to the Ikhana vehicle.

TWO-LINE STRAIN-SENSING SYSTEM

For the operational load estimations of a slender structure under combined bending and torsion loading, a two-line strain-sensing system can be used if the location of the neutral surface is known. Figure 2 shows a typical two-line strain-sensing system located on the lower surface of a double-tapered wing box (neutral surface at half depth) subjected to combined bending and torsion.

If the location of the neutral surface is unknown, then a four-line strain-sensing system (two lines on lower skin, two lines on upper skin) must be used to locate the neutral surface based on pairs of lower and upper surfaces strains at the same strain-sensing cross section (ref. 4).

The surface strains, $\{\varepsilon_i, \varepsilon_i'\}$, of the front and rear strain-sensing lines can be used to sense both bending and torsion (fig. 2). However, for sensing the torsion, the Displacement Transfer Functions (duplicated in Appendix A) developed earlier (ref. 1–9), are needed to convert the surface strains, $\{\varepsilon_i, \varepsilon_i'\}$, into out-of-plane deflections, $\{y_i, y_i'\}$, of the front and rear strain-sensing line for determining the cross-sectional twist angles, ϕ_i (see Appendix B). Thus, the two-line strain-sensing system with embodied Displacement Transfer Functions totally eliminates the need for the conventional distortion (shear) strain sensors to sense torsions.

For wider structures (low aspect ratios), multiple strain-sensing lines are needed on both upper and lower surfaces because the bending and torsion stiffness can vary, not only in the span-wise direction, but also in the chord-wise direction. The feasibility of this approach is currently under investigation.

METHOD FOR OPERATIONAL LOAD ESTIMATIONS

The method for estimating operational loads using distributed surface strains requires the foreknowledge of structural stiffness (bending and torsion). The method consists of two steps as described below.

Step One–Determinations of Structural Stiffness, $\{(EI)_i, (GK)_i\}$

Step one is to determine the bending and torsion stiffness, $\{(EI)_i, (GK)_i\}$. It must be understood that in the discretized cantilever beam system (figs. 1, 2), the bending stiffness, $(EI)_i$, is evaluated at the strain-sensing station, x_i (i=0,1,2,3,....,n), but the torsion stiffness, $(GK)_i$, is constant over the i-th domain lying between the two adjacent strain-sensing stations $\{x_{i-1}, x_i\}$ (fig 1). Keep in mind that there is no $i = 0$ domain (figs. 1, 2).

When using a two-line strain-sensing system (fig. 2), the values of $(EI)_i$ can be determined by using the surface strains induced by a specified bending loading test (or finite-element generated) for which $(\varepsilon_i = \varepsilon_i')$. The values of $(GK)_i$ can be determined from the cross-sectional twist angle, ϕ_i, induced by a specified torsion test (or finite-element generated) for which $(\varepsilon_i \neq \varepsilon_i')$. For torsion, the Displacement Transfer Functions must be introduced to convert the surface strains, $\{\varepsilon_i = \varepsilon_i'\}$, into deflections, $\{y_i, y_i'\}$, from which the cross-sectional twist angles, ϕ_i, can be determined.

The simplest loading case to determine the values of $(EI)_i$ is to apply a point load, P, at the beam tip (no torsion). Also, the simplest loading case to find the values of $(GK)_i$ is to apply a torque, T, at the beam tip (no bending). As will be seen shortly, the values of $\{(EI)_i, (GK)_i\}$ calculated from different loading conditions remain practically the same (that is, invariant to loading conditions).

Step Two–Estimations of Operational Loads, $\{M_i, P_i, T_i\}$

Step two for bending is to use the values of $(EI)_i$, pre-determined in step one, and a new set of averaged surface strains, $\bar{\varepsilon}_i\left[=(\varepsilon_i+\varepsilon_i')/2\right]$ (fig. 2), induced by other type of loading condition to estimate the associated operational loads (moments, shear loads), $\{M_i, P_i\}$, at the strain-sensing stations, x_i (i = 0,1,2,3,….,n).

Step two for torsion is to use the values of $(GK)_i$ pre-determined in step one, and the values of the cross-sectional twist angles, ϕ_i, calculated from the Displacement Transfer Functions using a new set of surface strains, $\{\varepsilon_i, \varepsilon_i'\}$ (fig. 2), induced by another type of loading condition to estimate the associated operational torques, T_i , at the strain-sensing stations, x_i (i = 0,1,2,3,….,n) .

BASIC EQUATIONS FOR BENDING

For a cantilever beam structure discretized into n small domains (fig. 1), the bottom surface bending strain, ε_i, induced by the bending moment, M_i, at strain-sensing station, x_i, can be related through the following moment equation (refs. 11, 12):

$$M_i = (EI)_i \frac{\varepsilon_i}{c_i} \quad ; \quad (i = 0,1,2,3,....,n) \tag{1}$$

In equation (1), c_i is the depth factor (distance from the neutral surface to beam bottom surface outermost fiber) at strain-sensing station, x_i (fig 1). Equation (1) is written in such a way that the positive bending moment, M_i, (bending the cantilever beam upward) will induce positive (tensile) strain, ε_i, on the bottom surface (fig.1).

Equation (1) can be rewritten in the following form (called bending-stiffness equation):

$$(EI)_i = M_i \frac{c_i}{\varepsilon_i} \quad ; \quad (i = 0,1,2,3,....,n) \tag{2}$$

If the right-hand side of equation (2) is known, one can then use equation (2) to determine the unknown bending stiffness, $(EI)_i$, at strain-sensing station, x_i. For a given slender structure, the depth factor, c_i, can be determined by using pairs of strains obtained from lower and upper surfaces (ref. 4). If the bending moment, M_i, is specified in a simple bending loading case, then the M_i-induced surface strains, ε_i, will be known from actual measurements, or ε_i can be calculated analytically from finite-element analysis (used in the present report). Thus, based on the known values of $\{M_i, \varepsilon_i\}$, the values of bending stiffness, $(EI)_i$, can be calculated from equation (2) as described in the following section.

Determination of Bending Stiffness, $(EI)_i$

To determine the bending stiffness, $(EI)_i$, the bending moment, M_i, must be specified. The simplest way to specify M_i is to consider a simple bending case of a cantilever beam of length, l, subjected to an

upward point load, P, at the beam tip. The bending moment, M_i, for such a bending case is a linearly decreasing function of x_i ($x_0 = 0$ at fixed end), and can be can be expressed as:

$$M_i = M_0\left(1-\frac{x_i}{l}\right) = M_0\left(1-\frac{i}{n}\right) \quad ; \quad (i = 0,1,2,3,....,n) \tag{3}$$

in which $M_0 (= Pl)$ is the maximum bending moment at the fixed end, $x = x_0 = 0$.

With the bending moment, M_i, thus specified from equation (3), the induced surface strains, ε_i, will be known. Then the known values of $\{M_i,\varepsilon_i,c_i\}$ can be input to the bending stiffness equation (2) to determine $(EI)_i$, which is needed for the calculations of operational moments and shear loads, $\{M_i, P_i\}$, as described in the following section.

Estimations of Operational Moments and Shear Loads, $\{M_i, P_i\}$

Once the cross-sectional bending stiffness, $(EI)_i$, is determined from equation (2), the strain-determined $(EI)_i$ and a new set of surface strains, ε_i, induced by another type of loading condition, can be used as inputs to calculate the current operational moment, M_i, at strain-sensing station, x_i, from equation (1), and the current operational shear loads, P_i, at strain-sensing station, x_i, from the following shear-load equation (or load-transfer function) (ref. 11):

$$P_i = -\left(\frac{dM}{dx}\right)_i \approx -\frac{M_i - M_{i-1}}{\Delta l} = \frac{1}{\Delta l}\left[(EI)_{i-1}\frac{\varepsilon_{i-1}}{c_{i-1}} - (EI)_i\frac{\varepsilon_i}{c_i}\right] \quad ; \quad (i = 1,2,3,....,n) \tag{4}$$

in which the moment equation (1) was used. Because the x-axis originated from the fixed end, equation (4) is written in such a way that decreasing bending moment in the span-wise direction (x direction) will produce positive shear load, P_i.

If the two-line strain-sensing system is used for sensing bending moments and shear loads (fig. 2), then $\{c_i, \varepsilon_i\}$ in equations (1), (2), and (4) must be replaced respectively with averaged depth factors, $\bar{c}_i\left[\equiv (c_i + c_i')/2\right]$, and averaged strains, $\bar{\varepsilon}_i\left[\equiv (\varepsilon_i + \varepsilon_i')/2\right]$, where $\left\{(c_i, \varepsilon_i)\right.$, $\left.(c_i', \varepsilon_i')\right\}$ are the depth factor and strain associated respectively with the front and rear strain-sensing lines (see Appendix B).

BASIC EQUATIONS FOR TORSION

In the estimations of operational torques, T_i, at the strain-sensing station, x_i, the two-line (or four-line) strain-sensing system (fig. 2) can be used to sense the cross-sectional rotations. The front and rear strain-sensing line strains, $\{\varepsilon_i, \varepsilon_i'\}$, at the strain-sensing station, x_i, can be first converted into front and rear strain-sensing-line deflections, $\{y_i, y_i'\}$, using the Displacement Transfer Functions (Appendix A). Then the differentials of $\{y_i, y_i'\}$, can be used to calculate cross-sectional twist angles, ϕ_i, for the estimations of operational torques, T_i.

Before the estimations of operational torques, T_i, using the cross-sectional twist angles, ϕ_i, one must first determine the torsion stiffness, $(GK)_i$, for the small domain, $x_{i-1} \le x \le x_i$, bounded by the two adjacent strain-sensing stations, $\{x_{i-1}\ ,\ x_i\}$. Here, G is the shear modulus and K is the twisting moment of inertia for a non-circular cross sections [for a circular cross section, $K = J$, the polar moment of inertia (ref. 11)].

Determination of Torsion Stiffness, $(GK)_i$

The torsion stiffness, $(GK)_i$, for a small domain, $x_{i-1} \le x \le x_i$, can be expressed in terms of the torque, T_i, and cross-sectional twist angle differential, $(\phi_i - \phi_{i-1})$, at the strain-sensing station, x_i, using the following torsion-stiffness equation (ref. 12):

$$(GK)_i = \frac{T_i(\Delta l)}{\phi_i - \phi_{i-1}} \quad ; \quad (i = 1,2,3,....,n) \tag{5}$$

In equation (5), $\Delta l (\equiv l/n)$ is the small domain length, and $\{\phi_i, \phi_{i-1}\}$ are the cross-sectional twist angles respectively at the strain-sensing stations, $\{x_i, x_{i-1}\}$, and which can be calculated from the following cross-sectional twist-angle equation (refs. 1 and 2) (see Appendix B):

$$\phi_i = \sin^{-1}\left(\frac{y_i - y_i'}{d_i}\right) \quad ; \quad (i = 0,1,2,3,....,n) \tag{6}$$

In equation (6), d_i is the chord-wise separation distance between the front and rear strain-sensing lines at $x = x_i$, and $\{y_i, y_i'\}$ are respectively the deflections of the front and rear strain-sensing lines at $x = x_i$ (fig. 2). Using the surface strains, $\{\varepsilon_i, \varepsilon_i'\}$, as inputs, the deflections $\{y_i, y_i'\}$, in equation (6) can be calculated from any of the Displacement Transfer Functions (listed in Appendix A) depending on the type of structure under consideration. For example, for the case of a doubly-tapered slender structure like a long span aircraft wing, the following Nonuniform Displacement Transfer Functions [eqs. (7) and (8)] can be used:

For front strain-sensing line:

$$\begin{aligned} y_i = & \underbrace{(\Delta l)^2 \sum_{j=1}^{i} \left\{ \frac{\varepsilon_{j-1} - \varepsilon_j}{2(c_{j-1} - c_j)} - \frac{\varepsilon_{j-1} c_j - \varepsilon_j c_{j-1}}{(c_{j-1} - c_j)^3} \left[c_j \log_e \frac{c_j}{c_{j-1}} + (c_{j-1} - c_j) \right] \right\}}_{\text{Contributions from deflection terms}} \\ & + \underbrace{(\Delta l)^2 \sum_{j=1}^{i-1} \left\{ (i-j) \left[\frac{\varepsilon_{j-1} - \varepsilon_j}{c_{j-1} - c_j} + \frac{\varepsilon_{j-1} c_j - \varepsilon_j c_{j-1}}{(c_{j-1} - c_j)^2} \log_e \frac{c_j}{c_{j-1}} \right] \right\}}_{\text{Contribution from slope terms}} + \underbrace{y_0 + (i)\Delta l \tan\theta_0}_{=0 \text{ for cantilever beams}} \end{aligned} \tag{7}$$

$$(i = 1,2,3,....,n)$$

For rear strain-sensing line:

$$y'_i = \underbrace{(\Delta l)^2 \sum_{j=1}^{i} \left\{ \frac{\varepsilon'_{j-1} - \varepsilon'_j}{2(c'_{j-1} - c'_j)} - \frac{\varepsilon'_{j-1}c'_j - \varepsilon'_j c'_{j-1}}{(c'_{j-1} - c'_j)^3} \left[c'_j \log_e \frac{c'_j}{c'_{j-1}} + (c'_{j-1} - c'_j) \right] \right\}}_{\text{Contributions from deflection terms}}$$
$$+ \underbrace{(\Delta l)^2 \sum_{j=1}^{i-1} \left\{ (i-j) \left[\frac{\varepsilon'_{j-1} - \varepsilon'_j}{c'_{j-1} - c'_j} + \frac{\varepsilon'_{j-1}c'_j - \varepsilon'_j c'_{j-1}}{(c'_{j-1} - c'_j)^2} \log_e \frac{c'_j}{c'_{j-1}} \right] \right\}}_{\text{Contribution from slope terms}} + \underbrace{y'_0 + (i)\Delta l \tan\theta'_0}_{=0 \text{ for cantilever beams}} \qquad (8)$$

$$(i = 1,2,3,....,n)$$

By considering a simple torsion loading case of applying a torque, T, at the beam tip, the cross-sectional torque, T_i, at the strain-sensing station, x_i, will be known (that is, $T_i = T$), and the cross-sectional twist angle, ϕ_i, can be calculated from equation (6) using the T-induced surface strains $\{\varepsilon_i, \varepsilon'_i\}$. Then, the torsion stiffness, $(GK)_i$, for the small domain, $x_{i-1} \le x \le x_i$, can be calculated from the torsion stiffness equation (5).

Estimations of Operational Torques, T_i

Once the torsion stiffness, $(GK)_i$, is determined from a simple torsion loading case mentioned above, a new set of cross-sectional twist angles, ϕ_i, induced by other types of torsion loading cases, can be used to calculate the operational torque, T_i, at strain-sensing station, x_i, using the following torque equation [rewritten form of equation (5)]:

$$T_i = (GK)_i \frac{\phi_i - \phi_{i-1}}{\Delta l} \quad ; \quad (i = 1,2,3,....,n) \qquad (9)$$

In equation (9), the values of ϕ_i are to be calculated from the twist angle equation (6) using the deflections, $\{y_i, y'_i\}$, converted from the new sets of surface strains, $\{\varepsilon_i, \varepsilon'_i\}$, induced by other types of torsion loading cases using equations (7) and (8). Keep in mind that the operational torque, T_i, remains constant over domain, $x_{i-1} \le x \le x_i$, of the discretized system.

FLOW CHART FOR OPERATIONAL LOADS ESTIMATIONS

For easy understanding of the new method of using distributed surface strain data to estimate both structure stiffness (bending, torsion) and operational loads (bending moments, shear loads, torques), a flow chart was constructed and is presented in Appendix-B for graphical illustration of the new method.

ANALYTICAL OPERATIONAL LOAD ESTIMATIONS

The new method of structural operational load estimations presented in this report is called the analytical method of operational load estimations. Namely, without using experimentally measured surface strains, the Structural Performance And Resizing (SPAR) finite-element computer program (ref. 13) was used to analytically calculate the surface strains and deflections. The surface strains, ε_i ($i = 1,2,3\ldots,n$), at the strain-sensing station, x_i, needed for inputs to calculate deflections [eqs. (7) and (8)] were obtained by converting the SPAR nodal stresses at the strain-sensing station, x_i, into bending strains, ε_i, through stress-strain law. Alternatively, the bending strains, ε_i, could also be calculated from

the axial length changes of the finite elements where the bending strains, ε_i, are evaluated. However, this method was found to lose accuracy near the highly bent regions of the deformed beam and, therefore, it was used only in the low slope region near the fixed end (refs. 1 and 2).

The SPAR-generated surface strains, $\{\varepsilon_i, \varepsilon_i'\}$, can then be input to the Displacement Transfer Functions [eqs. (7) and (8)] for the calculations of the deflections, $\{y_i, y_i'\}$, from which the cross-sectional twist angles, ϕ_i, could be calculated from equation (6). However, in the present report, the values of ϕ_i were calculated directly from equation (6) using the already existing SPAR-generated deflections, $\{y_i, y_i'\}$, instead of using the deflections calculated from equations (7) and (8). It is important to mention that the deflections calculated from equations (7) and (8), and from the SPAR-program were found to be amazingly close beyond expectations (refs. 1– 9). This high degree of accuracies of the Displacement Transfer Functions [for example, equations (7) and (8)], were also experimentally verified by large-scale ground loads tests of a full-scale long span wing (175-ft wingspan) (ref. 14).

EXAMPLES OF OPERATIONAL LOAD ESTIMATIONS

To show how to actually use the new method of operational load estimations, several example structures were chosen. The structures considered were:

1. Tapered cantilever tubular beam,
2. Depth-tapered un-swept wing box,
3. Depth-tapered swept wing box (bending-torsion coupling),
4. Doubly-tapered generic long-span wing.

Tapered Cantilever Tubular Beam

The first example structure used in the operational load estimation analysis is the aluminum- tapered cantilever tubular beam (fig. 3) with dimensions listed in table 1.

Table 1. Dimensions of aluminum tapered cantilever tubular beam.

l, in (length)	c_0, in (root radius)	c_n, in (tip radius)	t, in (wall thickness)
100.5	4.0	1.0	0.02296

As shown in figure 1, a single strain-sensing line is located on the bottom generatrix of the tapered cantilever tubular beam. The single-line strain-sensing system can only sense the bending-induced moments and shear loads, $\{M_i, P_i\}$. The strain-sensing line has n = 8 evenly spaced strain-sensing domains (that is, $n + 1 = 9$ strain-sensing stations). Figure 3 shows the un-deformed and deformed shapes of the SPAR model generated for the tapered cantilever tubular beam subjected to upward point load of P = 100 lb at the beam-tip disk center. This SPAR model has:

3,673 nodes---------- 101 nodes in axial direction
36 nodes in circumferential direction
37 nodes on the beam-tip disk
3,636 four-nodes elements----3,600 elements for tube wall
36 elements for beam-tip disk
36 three-nodes elements----- beam-tip disk central region

1. Determination of Bending Stiffness, $(EI)_i$

In the first step of determining the bending stiffness, $(EI)_i$, the tapered cantilever tubular beam (SPAR model) was subjected to an upward point load of P=100 lb at the beam tip (applied at disk center, fig. 3). This point load will produce the applied bending moments of $M_i = Pl(1 - i/n) = 10{,}050\times(1 - i/n)$ in-lb [eq. (3)].

Figure 4 shows the plot of the SPAR-generated surface strains, ε_i, induced by the present loading case. Unlike the straight-line strain distribution for a uniform cantilever beam (ref. 2), the strain curve for the tapered beam is highly nonlinear and bow shaped.

Using the known depth factor, c_i, the known applied bending moments, $M_i = 10{,}050\times(1 - i/n)$ in-lb [eq. (3)], and the induced surface strains, ε_i, shown in figure 4, the values of the bending stiffness, $(EI)_i$, at strain-sensing station, x_i, were calculated from bending stiffness equation [eq. (2)], and are listed in table 2.

Table 2. Bending stiffness, $(EI)_i$, for tapered cantilever tubular beam determined from surface strains, ε_i, induced by point load, P = 100 lb, at beam tip; n = 8, l = 100.5 in, Δl = 12.5625 in, $M_0 = Pl$ = 10,050 in-lb.

i	c_i, in	ε_i , $\times10^{-3}$ in/in (SPAR)	M_i/M_0 (known)	$(EI)_i$, $\times10^7$ lb-in^2 [from eq. (2)]	(elasticity)	(error, %)	$M_i[=(EI)_i(\varepsilon_i/c_i)]$, in-lb [calculated, eq. (1) = applied]	P_i, lb [calculated, eq. (4) = applied]
0	4.000	0.837143	1.0	4.802047	(4.847201)	(0.9316)	10,050.00	100.00
1	3.625	0.889524	7/8	3.583641	(3.607740)	(0.6680)	8,793.75	100.00
2	3.250	0.948571	6/8	2.582503	(2.599928)	(0.6702)	7,537.50	100.00
3	2.875	1.010476	5/8	1.787137	(1.799802)	(0.7037)	6,281.25	100.00
4	2.500	1.068571	4/8	1.175635	(1.183399)	(0.6561)	5,025.00	100.00
5	2.125	1.109524	3/8	0.721804	(0.726755)	(0.6812)	3,768.75	100.00
6	1.750	1.090476	2/8	0.403207	(0.405906)	(0.6649)	2,512.50	100.00
7	1.375	0.882857	1/8	0.195654	(0.196888)	(0.7307)	1,256.25	100.00
8	1.000	0.000000	0/8	0.099145*	(0.072131)	(37.4513)	0.00	100.00

*Three-points extrapolation [eq. (10)].

In table 2 the values of $(EI)_i$ calculated from the theory of elasticity are also listed (in parenthesis) for comparison. In the first column of $(EI)_i$, the strain-determined $(EI)_8$ at beam-tip $(i = 8)$ was extrapolated using the following three-points extrapolation formula:

$$(EI)_8 = (EI)_5 - 3(EI)_6 + 3(EI)_7 \tag{10}$$

Note from table 2 that the percent errors of strain-determined $(EI)_i$ are in the negligible range of (0.6561 ~ 0.9316) percent except for the extrapolated value of $(EI)_8$. The large 37.4513 percent error of $(EI)_8$ at beam-tip $(i = 8)$ can be attributed to a small number divided by another small number.

For checking the accuracy of the strain-determined bending stiffness, $(EI)_i$, the moment equation (1) and shear-load equation (4) were used to calculate the operational moments and shear loads, $\{M_i, P_i\}$, associated with the applied point load of, P=100 lb. The results are listed in the last two columns of table 2. Note that the values of $\{M_i, P_i\}$ are all identical to the applied moments, $M_i = 10{,}050\times(1 - i/n)$ in-lb and applied shear loads, $P_i = P = 100$ lb, confirming the accuracies of the strain-determined $(EI)_i$.

Figure 5 shows the plots of both strain-determined $(EI)_i$ and elasticity-calculated $(EI)_i$ based on the data of table 2. The strain-determined and elasticity-calculated values of $(EI)_i$ are practically coincidental, giving confidence in the new method for determining $(EI)_i$ from equation (2) using surface strains as inputs.

2. Estimations of Operational Moments and Shear Loads, $\{M_i, P_i\}$

Step 2 is to calculate the operational moments and shear loads, $\{M_i, P_i\}$, using the strain-determined $(EI)_i$, and the surface strains, ε_i, associated with a new loading case, for which the tapered cantilever tubular beam was subjected to point load, $P = 100$ lb, at the beam midpoint, and a second point load, $P = 100$ lb, at the beam tip. For the present two-points loading case, the applied bending moment can be expressed as:

For inboard region:

$$M_i = \frac{Pl}{2} + Pl\left(1 - 2\frac{i}{n}\right) = 5{,}025 + 10{,}050 \times \left(1 - 2\frac{i}{n}\right) \text{ (in-lb)} \quad ; \quad (0 \le i \le n/2) \tag{11}$$

For outboard region:

$$M_i = Pl\left(1 - \frac{i}{n}\right) = 10{,}050 \times \left(1 - \frac{i}{n}\right) \text{ (in-lb)} \quad ; \quad (n/2 \le i \le n) \tag{12}$$

Figure 6 shows the SPAR-generated surfaced strains, ε_i, induced by the present two-points loading case. The strain curve is consisted of two bent curves because of two-points loading.

Using the known beam depth factors, c_i, the surface strains, ε_i, of figure 6, and the pre-determined values of $(EI)_i$ listed in table 2, operational moments and shear loads, $\{M_i, P_i\}$, for the two-points loading case were calculated from equations (1) and (4), and are listed in table 3(a).

Table 3(a). Estimated operational moments and shear loads, $\{M_i, P_i\}$ for tapered cantilever tubular beam subjected to point load, $P = 100$ lb, at beam midpoint and second point load, $P = 100$ lb, at beam tip; $n = 8$; $l = 100.5$ in, $\Delta l = 12.5625$ in.

i	c_i, in	ε_i, $\times 10^{-3}$ in/in (SPAR)	$(EI)_i$, $\times 10^7$ lb-in^2 (from table 2)	$M_i[=(EI)_i(\varepsilon_i/c_i)]$, in-lb (estimated)	(applied)	(error, %)	P_i, lb (estimated)	(applied)	(error, %)
0	4.000	1.253333	4.802047	15,046.41	(15,075.00)	(0.1897)	197.94	(200.00)	(1.0300)
1	3.625	1.270476	3.583641	12,559.81	(12,562.50)	(0.2141)	197.94	(200.00)	(1.0300)
2	3.250	1.264762	2.582503	10,050.01	(10,050.00)	(0.0001)	199.79	(200.00)	(0.1050)
3	2.875	1.212381	1.787137	7,536.32	(7,537.50)	(0.0157)	200.09	(200.00)	(0.0450)
4	2.500	1.073810	1.175635	5,049.63	(5,025.00)	(0.4902)	197.95	(200.00)	(1.0250)
5	2.125	1.109524	0.721804	3,768.75	(3,768.75)	(0.0000)	101.96	(100.00)	(1.9600)
6	1.750	1.090476	0.403207	2,512.50	(2,512.50)	(0.0000)	100.00	(100.00)	(0.0000)
7	1.375	0.882857	0.195654	1,256.25	(1,256.25)	(0.0000)	100.00	(100.00)	(0.0000)
8	1.000	0.000000	0.099145*	0.00	(0.00)	(0.0000)	100.00	(100.00)	(0.0000)

* Three-points extrapolation [eq. (10)].

In table 3(a), the applied moments, M_i (induced by point load, $P = 100$ lb at beam midpoint, and second point load, $P = 100$ lb, at the beam-tip, fig. 6), were calculated from equations (11) and (12). In

table 3(a), the estimation errors of $\{M_i, P_i\}$ are also listed within the parentheses. The estimation error is defined as the percent difference between the estimated and applied values. The estimation errors of $\{M_i, P_i\}$ are extremely small, in the ranges of (0 ~ 0.4902) percent for M_i, and (0 ~ 1.9600) percent for P_i. The estimated shear loads, P_i, are nearly equal to the applied load of $P = 200$ lb in the inboard half region ($0 \le i \le 4$), and suddenly dropped to almost $P = 100$ lb in the outboard half region ($4 < i \le 8$) because of decreasing loading.

Figure 7 shows the plots of the estimated and applied $\{M_i, P_i\}$ data listed in table 3(a) for graphical comparisons. The estimated $\{M_i, P_i\}$ curves (dashed curves with open circular and diamond symbols) agreed nicely with the applied $\{M_i, P_i\}$ curves (solid lines with solid circular and diamond symbols). The high proximity of the estimated and applied moments and shear-loads gives confidence in the accuracies of the new method for structural operational load estimations.

3. Current Bending Stiffness, $(EI)_i$

For the current two-point loading (first point load, $P = 100$ lb, at beam midpoint, second point load, $P = 100$ lb, at beam tip), the bending moments, M_i, are known, and are expressed by equations (11) and (12). Therefore, the values of $(EI)_i$ can be re-calculated and compared with the pre-determined $(EI)_i$ listed in table 2. The results are compared in table 3(b).

Table 3(b). Bending stiffness, $(EI)_i$, for tapered cantilever tubular beam determined from surface strains, ε_i, induced by point load, $P = 100$ lb, at beam midpoint and second point load, $P = 100$ lb, at beam tip; $n = 8$, $l = 100.5$ in, $\Delta l = 12.5625$ in, $M_0 = Pl = 15{,}075$ in-lb.

i	c_i, in	ε_i, $\times 10^{-3}$ in/in (SPAR)	M_i, in-lb (known)	$(EI)_i$, $\times 10^7$ lb-in^2 [from eq. (2)]	$(EI)_i$, $\times 10^7$ lb-in^2 (from table 2)	(diff., %)	$M_i[=(EI)_i(\varepsilon_i/c_i)]$, in-lb [from eq. (1) = applied]	P_i, lb [from eq. (4) = applied]
0	4.000	1.253333	(15,075.00)	4.811171	(4.802047)	(0.1900)	15,075.00	200.00
1	3.625	1.270476	(12,562.50)	3.584410	(3.583641)	(0.0215)	12,562.50	200.00
2	3.250	1.264762	(10,050.00)	2.582502	(2.582503)	(0.0000)	10,050.00	200.00
3	2.875	1.212381	(7,537.50)	1.787418	(1.787137)	(0.0157)	7,337.50	200.00
4	2.500	1.073810	(5,025.00)	1.169900	(1.175635)	(0.4878)	5,025.00	200.00
5	2.125	1.109524	(3,768.75)	0.721804	(0.721804)	(0.0000)	3,768.75	100.00
6	1.750	1.090476	(2,512.50)	0.403207	(0.403207)	(0.0000)	2,512.50	100.00
7	1.375	0.882857	(1,256.25)	0.195654	(0.195654)	(0.0000)	1,256.25	100.00
8	1.000	0.000000	(0.00)	0.099145*	(0.099145*)	(0.0000)	0.00	100.00

* Three-points extrapolation [eq. (10)].

Note from table 3(b) that the values of $(EI)_i$ re-calculated from equation (2) based on the current two-points loading condition are extremely close to the pre-determined $(EI)_i$ values of table 2, with percent differences in the negligible range of (0 ~ 0.4878) percent. This proximity implies that $(EI)_i$ is practically invariant to the loading conditions, and giving confidence in the values of the pre-determined $(EI)_i$. If the current $(EI)_i$ is used, the estimation errors will become zero, and the estimated and the applied moments and shear loads, $\{M_i, P_i\}$, will be identical [last two columns of table 3(b)].

Depth-Tapered Un-swept Wing Box

The second example structure used in the operational load estimation analysis is the aluminum depth-tapered wing box with dimensions listed in table 4.

Table 4. Dimensions of aluminum depth-tapered un-swept wing box.

l, in (length)	c_0, in (root half depth)	c_n, in (tip half depth)	w_0, in (root width)	w_n, in (tip width)	t, in (wall thickness)
100.0	2.0	0.5	17.0	17.0	0.02296

Figure 8 shows the SPAR model generated for the depth-tapered wing box, with size indicated. This wing-box model was generated from the tubular beam model (fig. 3) by distorting the circular cross sections into rectangular cross sections. Each skin (upper or lower) was modeled with 1,700 four-node elements (100 elements in span-wise direction and 17 elements in chord-wise direction).

Because the neutral surface for the present depth-tapered wing box is located at half depth, a two-line strain-sensing system (inset of figure 8) was used for sensing the surface strains induced by bending and torsion. The front and rear strain-sensing lines are respectively located along the wing box lower front and rear edges. Each strain-sensing line has $n = 8$ evenly spaced domains (that is, $n + 1 = 9$ strain-sensing stations (inset of figure 8).

1. Determination of Bending Stiffness, $(EI)_i$

In step 1 of determining the bending stiffness, $(EI)_i$, the depth-tapered wing box was subjected to point load, $P = 100$ lb, at the wing-box tip (50 percent chord point). For the present loading case, the applied moment, M_i, at the strain-sensing station, x_i, in view of equation (3), is given by $M_i = M_0(1 - i/n) = 10{,}000\times(1 - i/n)$ in-lb.

Figure 9 shows the plot of surface strains, $\varepsilon_i\left(=\varepsilon_i'\right)$, and the associated deflections, $y_i\left(=y_i'\right)$, for the current loading case. Note that the bow-shaped strain curves and the deflection curves associated with the front and rear strain lines are identical.

Using the given depth factor, c_i, the known cross-sectional moments, $M_i = 10{,}000\times(1 - i/n)$ in-lb, and the strains, $\varepsilon_i\left(=\varepsilon_i'\right)$, shown in figure 9, the values of the bending stiffness, $(EI)_i$, were calculated from equation (2), and are listed in table 5.

Table 5. Bending stiffness, $(EI)_i$, for depth-tapered un-swept wing box determined from surface strains, $\varepsilon_i\left(=\varepsilon_i'\right)$, induced by point load, $P = 100$ lb, at wing-box tip; $n = 8$, $l = 100$ in, $\Delta l = l/n = 12.5$ in, $M_0 = Pl = 10{,}000$ in-lb.

i	c_i, in	$\varepsilon_i, \times 10^{-3}$ in/in (SPAR)	M_i/M_0 (known)	[from eq.(2)]	$(EI)_i, \times 10^7$ lb-in^2 (elasticity)	(error, %)	$M_i[=(EI)_i(\varepsilon_i/c_i)]$, lb-in [calculated, eq. (1) = applied]	P_i, lb [calculated, eq. (4) = applied]
0	2.000	0.358095	1.0	5.585110	(5.476832)	(1.9038)	10,000.00	100.00
1	1.8125	0.363810	7/8	4.359247	(4.316765)	(0.9893)	8,750.00	100.00
2	1.625	0.362857	6/8	3.358761	(3.323538)	(1.0598)	7,500.00	100.00
3	1.4375	0.356190	5/8	2.522355	(2.485710)	(1.4742)	6,250.00	100.00
4	1.25	0.341905	4/8	1.827993	(1.791836)	(2.0179)	5,000.00	100.00
5	1.0625	0.316190	3/8	1.260120	(1.230478)	(2.4090)	3,750.00	100.00
6	0.875	0.269048	2/8	0.813052	(0.790190)	(2.8932)	2,500.00	100.00
7	0.6875	0.187619	1/8	0.458043	(0.459531)	(0.3238)	1,250.00	100.00
8	0.500	0.000000	0/8	0.195093*	(0.227059)	(14.0783)	0.00	100.00

* Three-points extrapolation [eq. (10)].

In table 5 the values of $(EI)_i$ calculated from the theory of elasticity are also listed (in parenthesis) for comparison. Note that the percent errors of strain-determined $(EI)_i$ are in the small range of (0.9893 ~ 1.9038) percent, except for the extrapolated value of $(EI)_8$. The large 14.0783 percent error of $(EI)_8$ at beam-tip $(i = 8)$ can be attributed to a small number divided by another small number. Note also from table 5 that the values of $\{M_i, P_i\}$, calculated respectively from equations (1) and (4) using the strain-determined values of $(EI)_i$ are identical to the applied moments, $M_i = Pl(1 - i/n) = 10{,}000\times(1 - i/n)$ in-lb [eq. (3)] and applied shear loads, $P_i = P = 100$ lb. This agreement implies that the values of the strain-determined $(EI)_i$ are correct based on the present strain data.

Figure 10 shows the plots of both strain-determined $(EI)_i$ (dashed curve with open circular symbols) and elasticity-calculated $(EI)_i$ (solid curve with solid circular symbols) using data listed in table 5. Note from figure 10 that the strain-determined $(EI)_i$ curve and the elasticity- calculated $(EI)_i$ curve are almost coincidental except for the wing-box root where the strain-determined $(EI)_i$ is only 1.9038 percent larger than the elasticity-calculated $(EI)_i$.

2. Estimations of Operational Moments and Shear Loads, $\{M_i, P_i\}$

Step 2 is to use the strain-determined values of $(EI)_i$ listed in table 5 to calculate the operational moments and shear loads, $\{M_i, P_i\}$, associated with other loading case, for which the depth-tapered wing box was subjected to point load, $P = 200$ lb and clockwise torque, $T = 100\times w = 1{,}700$ in-lb at wing-box tip. The clockwise direction (looking toward the wing-box root from the wing-box tip) is defined as a positive torque in the present report. For the present loading condition, the applied moments, M_i, can be calculated from equation (3) by setting $M_0 = Pl = 200\times100 = 20{,}000$ in-lb in the form of equation (13):

$$M_i = M_0\left(1-\frac{i}{n}\right) = 20{,}000\times\left(1-\frac{i}{n}\right)\text{ (in-lb)} \quad ; \quad (i = 1,2,3,....,n) \tag{13}$$

Figure 11 shows the SPAR-generated surface strains, $\{\varepsilon_i, \varepsilon_i'\}$, and the associated deflections, $\{y_i, y_i'\}$, induced by the present combined bending and torsion loading case. The shapes of the two strain-curves are quite similar, and diverged in opposite directions toward the wing-box root due to intensified torsion effect at the fixed end.

Using the known beam depth factor, c_i, the averaged strains, $\bar{\varepsilon}_i\left[\equiv\left(\varepsilon_i + \varepsilon_i'\right)/2\right]$ (to eliminate torsion effect) obtained from strains $\{\varepsilon_i, \varepsilon_i'\}$ given in figure 11, and the strain-determined values of $(EI)_i$, listed in table 5, the operational moments and shear loads, $\{M_i, P_i\}$, were calculated respectively from equations (1) and (4). The results are listed in table 6(a).

Table 6(a). Estimated operational moments, shear loads $\{M_i, P_i\}$, using pre-determined $(EI)_i$ for depth-tapered un-swept wing box subjected to combined point load, $P = 200$ lb, and torque, $T = 100\times w = 1{,}700$ in-lb, at wing-box tip; $n = 8$, $l = 100$ in, $\Delta l = 12.5$ in, $M_0 = Pl = 20{,}000$ in-lb.

i	c_i, in	$\varepsilon_i,\times 10^{-3}$ in/in (SPAR)	$\varepsilon_i',\times 10^{-3}$ in/in (SPAR)	$\bar{\varepsilon}_i,\times 10^{-3}$ in/in (averaged)	$(EI)_i,\times 10^7$ lb-in^2 (from table 5)	$M_i[=(EI)_i(\bar{\varepsilon}_i/c_i)]$, in-lb (estimated)	(applied)	(error, %)	P_i, lb (estimated)	(error, %)
0	2.000	0.822857	0.570476	0.696667	5.737712	19,986.37	(20,000.00)	(0.0682)	197.99	(1.0050)
1	1.8125	0.749524	0.706667	0.728096	4.359247	17,511.44	(17,500.00)	(0.0654)	197.99	(1.0050)
2	1.625	0.740952	0.710000	0.725476	3.358761	14,995.08	(15,000.00)	(0.0328)	201.31	(0.6550)
3	1.4375	0.730476	0.693333	0.711905	2.522355	12,491.67	(12,500.00)	(0.0666)	200.27	(0.1350)
4	1.25	0.708095	0.659048	0.683572	1.827993	9,996.51	(10,000.00)	(0.0666)	199.61	(0.1950)
5	1.0625	0.664762	0.598095	0.631429	1.260120	7,488.71	(7,500.00)	(0.1505)	200.62	(0.3100)
6	0.875	0.587619	0.490000	0.538810	0.813052	5,006.63	(5,000.00)	(0.1326)	198.57	(0.7150)
7	0.6875	0.447619	0.301905	0.374762	0.458043	2,496.83	(2,500.00)	(0.1268)	200.78	(0.3900)
8	0.500	0.000000	0.000000	0.000000	0.195093*	0.00	(0.00)	(0.0000)	199.75	(0.1250)

* Three-points extrapolation [eq. (10)].

Note from Table 6(a) that the estimation errors are in the negligible ranges of (0 ~ 0.1505) percent for M_i, and (0.1250 ~ 1.0050) percent for P_i.

In figure 12, the estimated operational moments and shear loads, $\{M_i, P_i\}$, listed in Table 6-a are plotted for graphical comparisons with the applied $\{M_i, P_i\}$, values. The estimated $\{M_i, P_i\}$, curves (dashed curve with open circular and diamond symbols) practically fell on top of the respective applied $\{M_i, P_i\}$, curves (solid lines with solid circular and diamond symbols). Again, the high degree of proximity of the predicted and applied values of $\{M_i, P_i\}$, implies the accuracies of the new method for operational load estimations.

3. Current Bending Stiffness, $(EI)_i$

For the current combined bending and torsion loading case, the applied bending moments, M_i, are known and given by equation (13). Therefore, the values of $(EI)_i$ can be re-calculated and compared with the pre-determined $(EI)_i$ listed in table 5. The results are compared in table 6(b).

Table 6(b). Comparison of pre-determined $(EI)_i$ and current $(EI)_i$ for depth-tapered un-swept wing box subjected to combined point load, $P = 200$ lb, and torque, $T = 100\times w = 1{,}700$ in-lb, at wing-box tip; $n = 8$, $l = 100$ in, $\Delta l = 12.5$ in, $M_0 = Pl = 20{,}000$ in-lb.

i	c_i, in	$\varepsilon_i,\times 10^{-3}$ in/in (SPAR)	$\varepsilon_i',\times 10^{-3}$ in/in (SPAR)	$\bar{\varepsilon}_i,\times 10^{-3}$ in/in (averaged)	M_i/M_0	$(EI)_i,\times 10^7$ lb-in^2 (current)	(from table 5)	(diff., %)	$M_i[=(EI)_i(\bar{\varepsilon}_i/c_i)]$, in-lb (estimated = applied)	P_i, lb (estimated = applied)
0	2.000	0.822857	0.570476	0.696667	8/8	5.741624	(5.737712)	(0.0682)	20,000.00	200.00
1	1.8125	0.749524	0.706667	0.728096	7/8	4.356397	(4.359247)	(0.0654)	17,500.00	200.00
2	1.625	0.740952	0.710000	0.725476	6/8	3.359863	(3.358761)	(0.0328)	14,000.00	200.00
3	1.4375	0.730476	0.693333	0.711905	5/8	2.524038	(2.522355)	(0.0667)	12,500.00	200.00
4	1.25	0.708095	0.659048	0.683572	4/8	1.828630	(1.827993)	(0.0348)	10,000.00	200.00
5	1.0625	0.664762	0.598095	0.631429	3/8	1.262018	(1.260120)	(0.1506)	7,500.00	200.00
6	0.875	0.587619	0.490000	0.538810	2/8	0.811975	(0.813052)	(0.1325)	5,000.00	200.00
7	0.6875	0.447619	0.301905	0.374762	1/8	0.458624	(0.458043)	(0.1268)	2,500.00	200.00
8	0.500	0.000000	0.000000	0.000000	0/8	0.201965*	(0.195093)*	(3.5224)	0.00	200.00

* Three-points extrapolation [eq. (10)].

Note from table 6(b) that the values of $(EI)_i$ re-calculated from equation (2) based on the current loading condition are extremely close to the pre-determined $(EI)_i$ values, with percent differences in the negligible range of (0.0328 ~ 3.5224) percent. This proximity implies that $(EI)_i$ is practically invariant to the loading conditions, and one can feel confident in using the pre-determined $(EI)_i$. If the current $(EI)_i$ is used, table 6(b) shows that the estimation errors will become zero, causing the estimated operational moments and shear loads, $\{M_i, P_i\}$, to have exactly the same values as the applied $\{M_i, P_i\}$.

For complex loading conditions (for example, during flights), the applied moments, M_i, are unknown and constantly changing. Therefore, one has to rely upon the pre-determined $(EI)_i$ for estimating the operational moments and shear loads, $\{M_i, P_i\}$.

4. Determination of Torsion Stiffness, $(GK)_i$

To determine the domain torsion stiffness, $(GK)_i$, a clock-wise torque (positive, leading edge up) of $T = 50\times w = 850$ in-lb was applied at the un-swept wing-box tip. Figure 13 showed the plots of the front and rear deflections, $\{y_i, y_i'\}$, and the cross-sectional twist angles, ϕ_i [calculated from equation (6)]. Using the given beam depth factor, c_i, the known cross-sectional torques, $T_i[= T = 50\times w = 850$ in-lb], and the cross-sectional twist angles, ϕ_i, induced by the current torsion loading (fig. 13), the domain torsion stiffness, $(GK)_i$, are calculated from equation (5), and are listed in table 7.

Table 7. Torsion stiffness, $(GK)_i$, for depth tapered un-swept wing box determined from loading case of clock-wise torque (positive), $T = 50\times w = 850$ in-lb., at the wing box tip; $n = 8$, $l = 100$ in, $\Delta l = l/n = 12.5$ in.

i	c_i, in	$\phi_i,\times 10^{-3}$ rad [eq. (6)]	$(\phi_i - \phi_{i-1}),\times 10^{-3}$ rad	$(GK)_i,\times 10^7$ lb-in^2 [calculated, eq. (5)]	T_i, in-lb [calculated, eq. (9) = applied]
0	2.00	0.000000	----------	5.059234	850
1	1.8125	0.210012	0.210012	5.059234	850
2	1.625	0.504714	0.317650	3.344876	850
3	1.4375	0.914116	0.409402	2.595249	850
4	1.25	1.442358	0.528242	2.011389	850
5	1.0625	2.151171	0.708813	1.498985	850
6	0.875	3.155293	1.004122	1.058138	850
7	0.6875	4.686488	1.531195	0.693902	850
8	0.5	7.203585	2.517097	0.422113	850

In table 7, the value of $(GK)_i$ at $i = 1$ was used for $i = 0$ (not calculated) because $(GK)_i$ stays constant within the domain $x_0 \le x \le x_1$. In table 7, the torques, T_i, (last column) were calculated from equation (9) for the purpose of checking the accuracy of the strain-determined $(GK)_i$. Note that the calculated values of T_i are all exactly the same as the applied beam tip torque (that is, $T_i = T = 850$ in-lb), implying that the values of the strain-determined $(GK)_i$ are all correct.

In figure 14, the strain-determined values of $(GK)_i$ listed in table 7 are plotted for graphical display of the shape of the $(GK)_i$ curve. Because $(GK)_i$ is constant within each small domain, a dashed stepwise plot was used for the present finite number of domains. In the limit when the domain density becomes infinity (that is, $n \to \infty$), the stepwise curve will degenerate into a smooth solid curve shown in figure 14.

5. Estimations of Operational Torques, T_i

The strain-determined values of $(GK)_i$ listed in table 7, are to be used to estimate the operational torques, T_i, for a combined loading case of the depth-tapered wing box subjected to point load, $P = 200$ lb, and clock-wise torque, $T = 100 \times w = 1{,}700$ in-lb, at the wing-box tip.

Figure 15 shows the plots of the front and rear deflections, $\{y_i, y_i'\}$, and cross-sectional twist angles, ϕ_i, for the current combined loading case. Using the strain-determined values of $(GK)_i$ listed in table 7, and the values of ϕ_i, shown in figure 15, the operational torques, T_i, were calculated from the torque equation (9), and are listed in table 8(a).

Table 8-a. Estimated operational torques, T_i, using strain-determined $(GK)_i$ for depth-tapered un-swept wing box subjected to combined point load, $P = 200$ lb., and clockwise torque, $T = 100 \times w = 1{,}700$ in-lb, at wing tip; $n = 8$, $l = 100$ in, $\Delta l = l/n = 12.5$ in.

i	c_i, in	$\phi_i, \times 10^{-3}$ rad [eq. (6)]	$(\phi_i - \phi_{i-1}), \times 10^{-3}$ rad	$(GK)_i, \times 10^7$ lb-in^2 (from table 7)	T_i, in-lb (estimated)	(applied)	(error, %)
0	2.000	0.000000	0.000000	5.059234	1,699.89	(1,700.00)	(0.0065)
1	1.8125	0.419996	0.419996	5.059234	1,699.89	(1,700.00)	(0.0065)
2	1.625	1.055296	0.635300	3.344876	1,700.00	(1,700.00)	(0.0000)
3	1.4375	1.873524	0.818228	2.595249	1,698.80	(1,700.00)	(0.0706)
4	1.25	2.930006	1.056482	2.011389	1,700.00	(1,700.00)	(0.0000)
5	1.0625	4.348243	1.418237	1.498985	1,700.73	(1,700.00)	(0.0429)
6	0.875	6.355337	2.007094	1.058138	1,699.03	(1,700.00)	(0.0571)
7	0.6875	9.418076	3.062739	0.693902	1,700.20	(1,700.00)	(0.0118)
8	0.5	14.454031	5.035955	0.422113	1,700.59	(1,700.00)	(0.0347)

In table 8(a), the values of $\{(GK)_i, T_i\}$ at $i = 1$ were used for $i = 0$ (not calculated) because $\{(GK)_i, T_i\}$ at $i = 1$ is for the domain $x_0 \le x \le x_1$. The estimation errors of operational torques, T_i, are in the negligible range of (0.000 ~ 0.0706) percent.

In figure 16, the estimated operational torques, T_i, listed in table 8(a) are plotted for comparison with the applied torque, $T = 1{,}700$ in-lb. Note that, the estimated operational torques, T_i (dash curve with open circular symbols), practically fell on top of the applied torque line of $T = 1{,}700$ in-lb (solid line with solid circular symbols), showing the new method is promising for the structure operational load estimations.

6. Current Torsion Stiffness, $(GK)_i$

For the current loading condition, values of applied torques and cross-sectional twist angles, $\{T_i, \phi_i\}$, are known; therefore, the values of $(GK)_i$ can be recalculated from equation (5) for comparison with the pre-determined $(GK)_i$ listed in table 7. The results are compared in table 8(b).

Table 8-b. Comparison of pre-determined $(GK)_i$ and current $(GK)_i$ for depth-tapered un-swept wing box subjected to combined point load, $P = 200$ lb, and clockwise torque, $T = 100 \times w = 1{,}700$ in-lb, at wing tip; $n = 8$, $l = 100$ in, $\Delta l = l/n = 12.5$ in.

i	c_i, in	$\phi_i \times 10^{-3}$ rad [eq. (6)]	$(\phi_i - \phi_{i-1}) \times 10^{-3}$, rad	$(GK)_i \times 10^7$ lb-in^2 [current, eq. (5)]	$(GK)_i \times 10^7$ lb-in^2 (from table 7)	(diff., %)	T_i, in-lb (estimated = applied)
0	2.000	0.000000	0.000000	5.059572	(5.059234)	(0.0067)	1,700.00
1	1.8125	0.419996	0.419996	5.059572	(5.059234)	(0.0067)	1,700.00
2	1.625	1.055296	0.635300	3.344876	(3.344876)	(0.0000)	1,700.00
3	1.4375	1.873524	0.818228	2.597076	(2.595249)	(0.0704)	1,700.00
4	1.25	2.930006	1.056482	2.011393	(2.011389)	(0.0002)	1,700.00
5	1.0625	4.348243	1.418237	1.498339	(1.498985)	(0.0431)	1,700.00
6	0.875	6.355337	2.007094	1.058745	(1.058138)	(0.0574)	1,700.00
7	0.6875	9.418076	3.0062739	0.693823	(0.693902)	(0.0114)	1,700.00
8	0.5	14.454031	5.035955	0.421966	(0.422113)	(0.0348)	1,700.00

Note from table 8(b) that the values of $(GK)_i$ re-calculated from equation (5) based on ϕ_i of the current loading condition are amazingly close to the pre-determined $(GK)_i$ of table 7, with percent differences only in the negligible range of (0.0000 ~ 0.0704) percent. This proximity implies that, similar to $(EI)_i$, the pre-determined $(GK)_i$ are also practically invariant to the loading conditions, and thus confirming the accuracy of the pre-determined $(GK)_i$.

Depth-Tapered Swept Wing Box

The third example structure used in the operational load estimation analysis was the aluminum depth-tapered swept wing box (fig. 17) with dimensions listed in table 9.

Table 9. Dimensions of depth-tapered swept wing box.

l, in (length)	c_0, in (root half depth)	c_n, in (tip half depth)	w_0, in (root width)	w_n, in (tip width)	t, in (wall thickness)	β, deg (swept angle)
100.00	2.0	0.5	17.0	17.0	0.02296	10.0

Except for the swept angle, the dimensions of the swept wing box are identical to those of the un-swept wing box (table 4). The SPAR model (figs. 17, 18) of the depth-tapered swept wing box was generated from the SPAR model of the depth-tapered un-swept wing box (fig. 8) by simply distorting the rectangular skin shape of the un-swept wing box into a parallelogram skin shape by the swept angle, β.

Similar to the un-swept wing box case (fig. 8), the front and rear strain-sensing lines for the swept wing box are located respectively along the front and rear lower edges of the wing box (inset of fig.17). Each strain-sensing line has $n = 8$ evenly spaced domains (that is, $n + 1 = 0$ strain-sensing stations) (inset of fig. 17). Thus, the strain-sensing cross sections (formed by the pairs of front and rear strain-sensing stations) are parallel to the wing-box root chord and are, therefore, slanted with respect to the x-axis of the wing box by swept angle, β (in deg, fig. 17). Keep in mind that for the swept wing box, bending will induce torsion and vice versa (that is, bending and torsion are coupled).

1. Determination of Bending Stiffness, $(EI)_i$

For the swept wing box, the strain-sensing cross sections are slanted by β deg with respect to the wing box axis (x-axis, fig. 17). Therefore, the strain-determined $(EI)_i$ will not be the true $(EI)_i$, but must be considered as apparent $(EI)_i$ associated with the current particular strain-sensing station configurations. Because the values of the apparent $(EI)_i$ are to be used only as stepping-stones to calculate the operational moments and shear loads, $\{M_i, P_i\}$, it is not required to obtain the true $(EI)_i$ by re-arranging the strain-sensing cross sections to be normal to the x-axis (fig. 17).

In step 1 of determining the apparent bending stiffness, $(EI)_i$, the depth-tapered swept wing box was subjected to upward point load of $P = 100$ lb at the wing-box tip (50 percent chord, fig. 18). For the current loading condition, the applied moments will be $M_i = Pl(1 - i/n) = 10{,}000 \times (1 - i/n)$ in-lb [eq. (3)].

As shown in figure 18, the upward bending of the swept wing box induced slight counterclockwise rotation (defined as negative = decreasing angle of attack) when looking toward the wing box root from the wing-box tip. Keep in mind that for the swept wing box, bending and torsion are coupled. Namely, bending will induce torsion and vice versa.

Figure 19 shows the plots of surface strains $\{\varepsilon_i, \varepsilon_i'\}$, deflections $\{y_i, y_i'\}$, and cross-sectional twist angle, ϕ_i [calculated from eq. (6)] induced by a point load, $P = 100$ lb at the swept wing-box tip (50 percent chord). Note that, under bending, the rear deflections, y_i', are slightly larger than the associated front deflections, y_i (that is, $y_i' > y_i$), indicating slight counterclockwise cross-sectional rotations (that is, $\phi_i < 0$), with maximum cross-sectional twist angle of only $\phi_i = \phi_n = -0.2642$ deg at the wing-box tip. Note also from figure 19 that the differences between the pairs of front and rear strains, $\{\varepsilon_i, \varepsilon_i'\}$, are graphically inconspicuous except for the wing box root region where the rear train, ε_i', is markedly larger than the front strain, ε_i, because of increasing stress differentials caused by the swept effect.

In order to eliminate the bending-induced torsion components containing in the surface strains, $\{\varepsilon_i , \varepsilon_i'\}$ (fig.19), averaged strains, $\bar{\varepsilon}_i \left[\equiv (\varepsilon_i + \varepsilon_i')/2\right]$, were used in the calculations of the apparent $(EI)_i$.

Using the given depth factor, c_i, the averaged strains, $\bar{\varepsilon}_i$, and the known bending moments, $M_i = Pl(1 - l/n)$ in-lb, the apparent bending stiffness, $(EI)_i$, were calculated from equation (2) and are listed in table 10.

Table 10. Apparent bending stiffness, $(EI)_i$, for depth-tapered swept wing box determined from surface strains, $\{\varepsilon_i, \varepsilon_i'\}$, induced by point load, $P = 100$ lb, at wing-box tip; $n = 8$, $l = 100$ in, $\Delta l = l/n = 12.5$ in, $M_0 = Pl = 10.000$ in-lb.

i	c_i, in	$\varepsilon_i, \times 10^{-3}$ in/in (SPAR)	$\varepsilon_i', \times 10^{-3}$ in/in (SPAR)	$\bar{\varepsilon}_i, \times 10^{-3}$ in/in (averaged)	M_i/M_0 (known)	$(EI)_i, \times 10^7$ lb-in^2 [eq. (2), swept]	(table 5, un-swept)	(diff., %)	$M_i[=(EI)_i(\bar{\varepsilon}_i/c_i)]$, in-lb [from eq. (1)] = applied	P_i, lb [from eq. (4) = applied]
0	2.000	0.260000	0.448571	0.354286	1.0	5.645157	(5.737712)	(1.6131)	10,000.00	100.00
1	1.8125	0.345714	0.377143	0.361429	7/8	4.387964	(4.359247)	(0.6588)	8,750.00	100.00
2	1.625	0.356190	0.368095	0.362143	6/8	3.365383	(3.358761)	(0.1972)	7,500.00	100.00
3	1.4375	0.351429	0.360952	0.356191	5/8	2.522348	(2.522355)	(0.1972)	6,250.00	100.00
4	1.25	0.338095	0.345714	0.341905	4/8	1.827993	(1.827993)	(0.0000)	5,000.00	100.00
5	1.0625	0.313333	0.318095	0.315714	3/8	1.262020	(1.260120)	(0.1508)	3,750.00	100.00
6	0.875	0.270952	0.267619	0.269286	2/8	0.812333	(0.803152)	(1.1431)	2,500.00	100.00
7	0.6875	0.194286	0.180952	0.187619	1/8	0.461558	(0.458043)	(0.7674)	1,250.00	100.00
8	0.500	0.000000	0.000000	0.000000	0/8	0.209695*	(0.195093)	(7.4877)	0.00	100.00

* Three-points extrapolation [eq. (10)].

In table 10 the values of $(EI)_i$ for the un-swept wing box (taken from table 5) are also listed (in parenthesis) for comparison. The two sets of $(EI)_i$ are quite close with percent differences in the negligible range of (0.0000 ~ 1.6131) percent, except wing-box tip. The large difference (7.4877 percent) at the wing-box tip is due to a small number divided by another small number. In the last two columns of table 10, the values of operational moments and shear loads, $\{M_i, P_i\}$, were calculated respectively from equations (1) and (4) using the strain-determined apparent $(EI)_i$. The calculated values of $\{M_i, P_i\}$ are exactly the same as the applied values of $\{M_i, P_i\}$. This perfect agreement indicates that the calculated apparent $(EI)_i$ associated with the present strain-sensing station configuration can be used with confidence as stepping-stones in the estimations of the operational loads on the swept wing-box.

Figure 20 shows the plots of the strain-determined apparent $(EI)_i$ curve (solid curve with solid circular symbols) for the swept wing box and the elasticity-calculated $(EI)_i$ curve (dashed curve with open circular symbols) for the un-swept wing box (table 5). The two $(EI)_i$ curves are quite close except for the slight difference near the wing-box root (see table 10).

2. Estimations of Operational Moments and Shear Loads, $\{M_i, P_i\}$

Based on the pre-determined apparent bending stiffness, $(EI)_i$, listed in table 10, the operational moments and shear loads, $\{M_i, P_i\}$, were calculated for two different loading cases:

1) Bending load, $P = 200$ lb, applied at wing-box tip (to study bending-induced torsion)
2) Combined bending load, $P = 200$ lb, and counterclockwise torque, $T = -100 \times w = -1{,}700$ in-lb, applied at the wing-box tip (to study bending-torsion coupling).

2.1. Bending Only ($P = 200$ lb)

For step 2, the pre-determined apparent $(EI)_i$ listed in table 10 were used to calculate the operational moments and shear loads, $\{M_i^P, P_i^P\}$, for the depth-tapered swept wing box subjected to point load of $P = 200$ lb at the wing-box tip (50 percent chord). For the current loading condition, the applied moments will be $M_i^P = Pl\left(1 - \frac{i}{n}\right) = 20{,}000(1 - i/n)$ in-lb.

Figure 21 shows the plots of SPAR-generated strains, $\{\varepsilon_i, \varepsilon_i'\}$, deflections, $\{y_i, y_i'\}$, and cross-sectional twist angle, ϕ_i^P [eq. (6)], induced by the point load of $P = 200$ lb at the wing-box tip. Note that the values

of the rear strains, ε_i', are slightly larger than the corresponding front strains, ε_i, indicating that the upward bending induced counterclockwise rotation ($\phi_i^P < 0$). The data of ϕ_i^P are to be used to calculate the bending-induced torque components, T^P, in the subsequent combined bending and torsion analysis. The difference between the two strains is greatly magnified toward the wing-box root because of swept effect.

Using the known depth factor, c_i, the averaged strains, $\bar{\varepsilon}_i^P \left[\equiv (\varepsilon_i + \varepsilon_i')/2 \right]$ (to eliminate torsion effect) based on the strains, $\{\varepsilon_i, \varepsilon_i'\}$, of figure 21, and the strain-determined apparent $(EI)_i$ listed in table 10, the operational moments and shear loads, $\{M_i^P, P_i^P\}$ were calculated respectively from equations (1) and (4), and are listed in table 11.

Table 11. Estimated operational moments and shear loads, $\{M_i^P, P_i^P\}$, based on strain-determined apparent $(EI)_i$ for depth-tapered swept wing box subjected to point load, $P = 200$ lb, at wing-box tip; $n = 8$, $l = 100$ in, $\Delta l = l/n = 12.5$ in, $M_0 = Pl = 20{,}000$ in-lb.

i	c_i, in	ε_i, $\times 10^{-3}$ in/in (SPAR)	ε_i', $\times 10^{-3}$ in/in (SPAR)	$\bar{\varepsilon}_i^P$, $\times 10^{-3}$ in/in (averaged)	ϕ_i^P, $\times 10^{-3}$ rad [eq. (6)]	$(EI)_i$, $\times 10^7$ lb-in^2 (from table 10)	$M_i^P \left[= (EI)_i (\bar{\varepsilon}_i^P / c_i) \right]$, in-lb (estimated)	(applied)	(error, %)	P_i^P, lb (estimated)	(applied)	(error, %)
0	2.000	0.520000	0.898095	0.709048	0.000000	5.645157	20,013.42	(20,000)	(0.0671)	206.61	(200)	(3.3050)
1	1.8125	0.688571	0.751429	0.720000	-0.602941	4.387964	17,430.81	(17,500)	(0.3954)	206.61	(200)	(3.3050)
2	1.625	0.712381	0.736667	0.724524	-1.589412	3.365383	15,004.93	(15,000)	(0.0329)	194.07	(200)	(2.9650)
3	1.4375	0.702587	0.720952	0.711770	-2.717941	2.522348	12,489.26	(12,500)	(0.0859)	201.25	(200)	(0.6250)
4	1.25	0.675714	0.691429	0.683572	-3.961765	1.827993	9,996.52	(10,000)	(0.0048)	199.42	(200)	(0.2900)
5	1.0625	0.627619	0.636190	0.631905	-5.310882	1.262020	7,505.66	(7,500)	(0.0755)	199.27	(200)	(0.3650)
6	0.875	0.541429	0.535714	0.538572	-6.725294	0.812333	5,000.00	(5,000)	(0.0000)	200.45	(200)	(0.2250)
7	0.6875	0.387619	0.362857	0.375238	-8.071176	0.461558	2,519.19	(2,500)	(0.7676)	198.46	(200)	(0.7700)
8	0.500	0.000000	0.000000	0.000000	-9.214706	0.209695*	0.00	(0.00)	(0.0000)	201.54	(200)	(0.7700)

The errors of the estimated $\{M_i^P, P_i^P\}$ listed in table 11 are in reference respectively to the applied moments, $M_i^P = M_0(1 - i/n) = 20{,}000 \times (1 - i/n)$ in-lb, and applied shear loads, $P_i^P = 200$ lb. Note from table 11 that the errors of estimated M_i^P are in the negligible ranges of (0 ~ 0.7676) percent, and the errors of estimated P_i^P are in the small range of (0.2250 ~ 3.3050). Table 11 also lists the cross-sectional twist angles, ϕ_i^P (< 0), induced by the bending load of $P = 200$ lb because of swept effect. The values of ϕ_i^P listed in table 11 will be used to calculate the bending-induced torque components, T^P, in the subsequent combined bending and torsion analysis after the values of apparent torsion stiffness, $(GK)_i$ have been determined.

In figure 22, the estimated operational moments and shear loads, $\{M_i^P, P_i^P\}$, listed in the last two columns of table 11 are plotted for graphical comparison with the applied moments and applied shear loads, $\{M_i^P, P_i^P\}$ (table 11). Note that the estimated M_i^P curve (dashed line with open circular symbols) is practically coincidental to the applied M_i^P curves (solid straight line with solid circular symbols). On the other hand, the estimated P_i^P curve (dashed curve with open diamond symbols) agreed nicely with the applied P_i^P curve (solid straight line with solid diamond symbols) in the outboard region, but slightly off near the wing box root. The good correlations between the estimated and applied $\{M_i^P, P_i^P\}$ thus give the confidence in the new method for operational load predictions using surface strains.

2.2. Combined bending and Torsion ($P = 200$ lb, $T = -1{,}700$ in-lb)

For step 2, the values of strain-determined apparent $(EI)_i$ listed in table 10 were used to estimate the operational moments and shear loads, $\{M_i^{P+T},\ P_i^{P+T}\}$, for the combined loading case of the depth-tapered swept wing box subjected to point load, $P = 200$ lb, and counterclockwise torque, $T = -1{,}700$ in-lb, at the wing-box tip. For the current combined bending and torsion loading, the applied moment, M_i^{P+T}, induced by the applied point load , P, and torque, T, can be expressed as:

$$M_i^{P+T} = \underbrace{Pl\left(1-\frac{i}{n}\right)}_{\substack{P\text{-induced}\\ \text{bending moment}}} + \underbrace{T\sin\beta}_{\substack{T\text{-induced}\\ \text{bending}\\ \text{moment}}} = \underbrace{20{,}000\times\left(1-\frac{i}{n}\right)}_{P\text{-induced}} + \underbrace{295.20}_{T\text{-induced}} \qquad (14)$$

$$(i = 0,1,2,3,....,n)$$

Note from equation (14) that the torque-induced bending moments are constant along the x-axis of the swept wing box axis (fig. 17), implying that the applied torque, T, induces only pure bending for which shear loads are zero. The estimations of operational torque, T_i^{P+T}, induced by the current combined bending and torsion loading case will be delayed until the values of torsion stiffness, $(GK)_i$, are determined.

Figure 23 shows the plots of strains, $\{\varepsilon_i,\ \varepsilon_i'\}$, the total averaged strains, $\bar{\varepsilon}_i^{P+T}\left[\equiv(\varepsilon_i+\varepsilon_i')/2\right]$, deflections, $\{y_i,\ y_i'\}$, and cross-sectional twist angle, $\phi_i^{P+T}(<0)$, induced by the current combined bending and torsion loading. Also in figure 23, the averaged surface strains, $\bar{\varepsilon}_i^{T}$, induced by the counterclockwise torque, $T = -1{,}700$ in-lb only are also plotted for comparison. Note that the values of $\bar{\varepsilon}_i^{T}$ are almost negligible in comparison with the values of $\bar{\varepsilon}_i^{P+T}$. Because of counterclockwise twist, the rear bending strains and deflections, $\{\varepsilon_i',\ y_i'\}$, are somewhat larger than the front bending strains and deflections, $\{\varepsilon_i,\ y_i\}$. Note that the difference between ε_i and ε_i' is greatly magnified (greater than bending case in fig. 21) toward the swept wing-box root because of added torsion and swept effect.

In view of the known depth factor, c_i, and the values of strain-determined apparent $(EI)_i$ listed in table 10, the operational moments and shear loads, $\{M_i^{P+T},\ P_i^{P+T}\}$, were calculated respectively from equations (1) and (4) using the averaged strains, $\bar{\varepsilon}_i^{P+T}$. The resulting values of the estimated total operational bending moments and shear loads $\{M_i^{P+T},\ P_i^{P+T}\}$ for the current combined bending and torsion loading case are listed in table 12.

Note in table 12 that the errors of estimated M_i^{P+T} are in the negligible range of (0.0437 ~ 0.8765) percent except for the wing-box tip (22.5847 percent error). On the other hand, the errors of estimated P_i^{P+T} are also in the negligible range (0.025 ~ 2.7450) percent except for the fixed end region (3.7550 percent error).

Table 12. Estimated operational moments and shear loads, $\{M_i^{P+T}, P_i^{P+T}\}$, based on strain-determined apparent $(EI)_i$ for depth tapered swept wing box subjected to point load, $P = 200$ lb, and counterclockwise torque, $T = -100 \times w = -1{,}700$ in-lb, at wing box tip; $n = 8$, $l = 100$ in, $\Delta l = l/n = 12.5$ in.

i	c_i, in	$\varepsilon_i, \times 10^{-3}$ in/in (SPAR)	$\varepsilon_i', \times 10^{-3}$ in/in (SPAR)	$\bar{\varepsilon}_i^{P+T}, \times 10^{-3}$ in/in (averaged)	$(EI)_i, \times 10^7$ lb-in^2 (from table 10)	$M_i^{P+T}[=(EI)_i(\bar{\varepsilon}_i^{P+T}/c_i)]$, in-lb (estimated)	(applied)	(error, %)	P_i^{P+T}, lb (estimated)	(applied)	(error, %)
0	2.000	0.393333	1.047619	0.720476	5.645157	20,336.00	(20,295.20)	(0.2010)	207.51	(200)	(3.7550)
1	1.8125	0.680000	0.785714	0.732857	4.387964	17,742.07	(17,795.20)	(0.2986)	207.51	(200)	(3.7550)
2	1.625	0.711429	0.767143	0.739286	3.365383	15,310.65	(15,295.20)	(0.1007)	194.51	(200)	(2.7450)
3	1.4375	0.700952	0.758095	0.729524	2.522348	12,800.79	(12,795.20)	(0.0437)	200.79	(200)	(0.3950)
4	1.25	0.674286	0.737619	0.705953	1.827993	10,323.82	(10,295.20)	(0.2780)	198.16	(200)	(0.9240)
5	1.0625	0.619048	0.697143	0.658096	1.262020	7,816.76	(7,795.20)	(0.2766)	200.56	(200)	(0.2800)
6	0.875	0.525238	0.620000	0.572619	0.812333	5,316.08	(5,295.20)	(0.3943)	200.05	(200)	(0.0250)
7	0.6875	0.358095	0.481905	0.420000	0.461558	2,819.70	(2,795.20)	(0.8765)	199.71	(200)	(0.1450)
8	0.500	0.021952	0.150619	0.086286	0.209695*	361.87	(295.20)	(22.5847)	196.63	(200)	(1.6850)

In figure 24, the estimated operational moments and shear loads, listed in table 12 are plotted for graphical comparison with the applied moments [eq. (14)] and applied shear loads, $P_i^{P+T} = P_i^P = 200$ lb. Note that the estimated M_i^{P+T} curve (dashed curve with open circular symbols) are graphically coincidental with applied M_i^{P+T} curve (solid straight lines with solid circular symbols). On the other hand, the estimated P_i^{P+T} curve (dashed curve with open diamond symbols) agreed with the applied P_i^{P+T} curves (solid straight lines with solid diamond symbols), but is slightly off in the fixed and free end regions. Such satisfactory performance gives confidence in the new method for estimating the operational loads using surface strains. The accuracies of the components contained in the total estimated loads $\{M_i^{P+T}, P_i^{P+T}\}$ will also be investigated in the following sections.

2.3. Bending-induced Components, $\{M_i^P, P_i^P\}$

To calculate the P-induced operational load components, $\{M_i^P, P_i^P\}$, the averaged strains, $\bar{\varepsilon}_i^T$, induced by the counterclockwise torque, $T = -1{,}700$ in-lb (fig. 23) must be abstracted from the total averaged strains, $\bar{\varepsilon}_i^{P+T}$. Namely, to eliminate T-induced components, $\{M_i^T, P_i^T\}$, the strain differentials, $\bar{\varepsilon}_i^{P+T} - \bar{\varepsilon}_i^T$, must be used to calculate $\{M_i^P, P_i^P\}$.

In view of the known depth factor, c_i, and the values of strain-determined apparent $(EI)_i$ listed in table 10, the P-induced operational load components, $\{M_i^P, P_i^P\}$ were calculated respectively from equations (1) and (4) using the averaged strain differentials, $\bar{\varepsilon}_i^{P+T} - \bar{\varepsilon}_i^T$. The resulting estimated values of $\{M_i^P, P_i^P\}$ are listed in table 13.

Table 13. Bending induced components $\{M_i^P, P_i^P\}$, of estimated operational moments and shear loads, $\{M_i^{P+T}, P_i^{P+T}\}$, based on strain-determined apparent $(EI)_i$ for depth-tapered swept wing-box subjected to point load, $P = 200$ lb, and counter-clockwise torque, $T = -100 \times w = -1{,}700$ in-lb, at wing-box tip; $n = 8$, $l = 100$ in, $\Delta l = l/n = 12.5$ in.

i	c_i, in	$\bar{\varepsilon}_i^{P+T}$, $\times 10^{-3}$ in/in (P+T)	$\bar{\varepsilon}_i^{T}$, $\times 10^{-3}$ in/in (T only)	$(\bar{\varepsilon}_i^{P+T} - \bar{\varepsilon}_i^{T})$, $\times 10^{-3}$ in/in (differential)	$(EI)_i$, $\times 10^7$ lb-in^2 (from table 10)	$M_i^P\{=(EI)_i[(\bar{\varepsilon}_i^{P+T} - \bar{\varepsilon}_i^{T})/c_i]\}$, in-lb (estimated)	(applied)	(error, %)	P_i^P, lb (estimated)	(applied)	(error, %)
0	2.00	0.720476	0.011905	0.708571	5.645157	20,001.44	(20,000.00)	(0.0072)	200.12	(200)	(0.0600)
1	1.8125	0.732857	0.010000	0.722857	4.387964	17,499.98	(17,500.00)	(0.0001)	200.12	(200)	(0.0600)
2	1.625	0.739286	0.014762	0.724542	3.365383	15,005.30	(15,000.00)	(0.0353)	195.57	(200)	(2.2150)
3	1.4375	0.729524	0.017619	0.711905	2.522348	12,491.63	(12,500.00)	(0.0670)	201.09	(200)	(0.5450)
4	1.25	0.705953	0.021190	0.684763	1.827993	10,013.94	(10,000.00)	(0.1394)	198.22	(200)	(0.8900)
5	1.0625	0.658096	0.026667	0.630667	1.262020	7,490.96	(7,500.00)	(0.1206)	201.84	(200)	(0.9200)
6	0.875	0.572619	0.034286	0.538333	0.812333	4,997.78	(5,000.00)	(0.0444)	199.45	(200)	(0.2750)
7	0.6875	0.420000	0.038573	0.381429	0.461558	2,560.75	(2,500.00)	(2.4000)	194.96	(200)	(2.5200)
8	0.500	0.086286	0.042857	0.043429	0.209695*	182.14	(0.00)	----------	190.29	(200)	(4.8550)

* Three-points extrapolation [eq. (10)].

In table 13, the applied moments, M_i^P, listed in parentheses, were calculated from $M_i^P = M_0(1 - i/n) = 20{,}000 \times (1 - i/n)$ in-lb [eq. (3)]. Note from table 13 that the estimation errors of P-induced operational moment, $\mathrm{M_i^P}$, are in the small range of (0.0001 ~ 2.4000) percent. The estimation errors of P -induced operational shear loads, P_i^P, are also in the small range of (0.0600 ~ 2.5200) percent except for the free end (4.8550 percent error). Note also that the values of $\{M_i^P, P_i^P\}$ extracted from combined bending and torsion loading (table 13) are reasonably close to the values of $\{M_i^P, P_i^P\}$ determined from bending loading only (table 11).

In view of equation (14), the torsion-induced applied moment, $M_i^T = 295.20$ in-lb, is constant along the span, and such pure bending does not induce any shear loads. Therefore, the applied shear loads for both P_i^{P+T} (table 12) and P_i^P (table 13) are identical to the applied point load, $P = 200$ lb.

2.4. Torsion-induced Components, $\{M_i^T, P_i^T\}$

The torsion-induced components of operational moments and shear loads, $\{M_i^T, P_i^T\}$, can be calculated using the combined-load induced averaged surface strains, $\bar{\varepsilon}_i^{P+T}$ (table 12). However, the bending-induced averaged strains, $\bar{\varepsilon}_i^P$ (table 11), must be subtracted from $\bar{\varepsilon}_i^{P+T}$.

In view of the known depth factor, c_i, and the values of strain-determined apparent $(EI)_i$ listed in table 10, the torsion-induced operational moments and shear loads, $\{M_i^T, P_i^T\}$ were calculated respectively from equations (1) and (4) using the averaged strain differentials, $(\bar{\varepsilon}_i^{P+T} - \bar{\varepsilon}_i^{P})$, to eliminate P-induced components, $\{M_i^P, P_i^P\}$. The resulting estimated values of $\{M_i^T, P_i^T\}$ are listed in table 14.

Table 14. Torsion induced components $\{M_i^T, P_i^T\}$ of estimated operational moments and shear loads, $\{M_i^{P+T}, P_i^{P+T}\}$, based on strain-determined apparent $(EI)_i$ for depth-tapered swept wing box subjected to point load, $P = 200$ lb, and counterclockwise torque, $T = -100 \times w = -1{,}700$ in-lb, at wing-box tip; $n = 8$, $l = 100$ in, $\Delta l = l/n = 12.5$ in.

i	c_i, in	$\bar{\varepsilon}_i^{P+T}, \times 10^{-3}$ in/in (combined load)	$\bar{\varepsilon}_i^{P}, \times 10^{-3}$ in/in (P-induced, from table 11)	$(\bar{\varepsilon}_i^{P+T} - \bar{\varepsilon}_i^{P}), \times 10^{-3}$, in/in (differential)	$(EI)_i, \times 10^7$ lb-in^2 (from table 10)	$M_i^T\{=(EI)_i[(\bar{\varepsilon}_i^{P+T} - \bar{\varepsilon}_i^{P})/c_i]\}$, in-lb (estimated)	(applied)	(error, %)	P_i^T, lb (estimated)	(applied)
0	2.000	0.720476	0.709048	0.011428	5.645157	322.56	(295.20)	(9.2683)	0.90	(0.00)
1	1.8125	0.732857	0.720000	0.012857	4.387964	311.26	(295.20)	(5.4404)	0.90	(0.00)
2	1.625	0.739286	0.724524	0.014762	3.365383	305.72	(295.20)	(3.5637)	0.44	(0.00)
3	1.4375	0.729524	0.711770	0.017754	2.522348	311.53	(295.20)	(5.5318)	-0.46	(0.00)
4	1.25	0.705953	0.683572	0.022381	1.827993	327.30	(295.20)	(10.8740)	-1.26	(0.00)
5	1.0625	0.658096	0.631905	0.026191	1.262020	311.09	(295.20)	(5.3828)	1.29	(0.00)
6	0.875	0.572619	0.538572	0.034047	0.812333	316.09	(295.20)	(7.0766)	-0.40	(0.00)
7	0.6875	0.420000	0.375238	0.044762	0.461558	300.51	(295.20)	(1.7988)	1.25	(0.00)
8	0.500	0.086286	0.000000	0.086286	0.209695*	361.87	(295.20)	(22.5847)	-4.91	(0.00)

* Three-points extrapolation [eq. (10)].

In table 14, the torsion-induced applied moments are constant and were calculated from $M_i^T = T \sin\beta = 295.20$ in-lb [last term in equation (14)]. The errors of estimated torque-induced moment, M_i^T, are in the range of (1.7988 ~ 9.2683) percent excluding the wing-box tip (22.5947 percent error). Because the torsion-induced bending moments are constant (pure bending) along the wing box span, no applied shear loads were induced (that is, $P_i^T = 0$). Note that the torque-induced components of the estimated operational shear loads, P_i^T, in the last column are very close to the theoretical zero value. Alternatively, the torsion-induced components $\{M_i^T, P_i^T\}$ can be obtained from the total estimated operational moments and shear loads, $\{M_i^{P+T}, P_i^{P+T}\}$ (table 12) by subtracting the P-induced components, $\{M_i^P, P_i^P\}$ (table 11). Namely, using the formulae, $M_i^T = M_i^{P+T} - M_i^P$ and $P_i^T = P_i^{P+T} - P_i^P$. The results are listed in table 15.

Table 15. Estimated operational moments and shear loads, $\{M_i^T, P_i^T\}$, based on strain-determined apparent $(EI)_i$ for depth tapered swept wing box subjected to point load, $P = 200$ lb, and counterclockwise torque, $T = -100 \times w = -1{,}700$ in-lb, at wing box tip; $n = 8$, $l = 100$ in, $\Delta l = l/n = 12.5$ in.

i	c_i, in	M_i^{P+T}, in-lb (table 12)	M_i^P, in-lb (table 11)	$M_i^T\left(=M_i^{P+T} - M_i^P\right)$, in-lb (estimated)	(applied)	(error, %)	P_i^{P+T}, lb (table 12)	P_i^P, lb (table 11)	$P_i^T\left(=P_i^{P+T} - P_i^P\right)$, lb (estimated)	(applied)
0	2.000	20,336.00	20,013.42	322.58	(295.20)	(9.2752)	207.51	206.61	0.90	(0.00)
1	1.8125	17,742.07	17,430.81	311.26	(295.20)	(5.4404)	207.51	206.61	0.90	(0.00)
2	1.625	15,310.65	15,004.93	305.72	(295.20)	(3.5637)	194.51	194.07	0.44	(0.00)
3	1.4375	12,800.79	12,489.26	311.53	(295.20)	(5.5318)	200.79	201.25	-0.46	(0.00)
4	1.25	10,323.82	9,996.52	327.30	(295.20)	(10.8740)	198.16	199.42	-1.26	(0.00)
5	1.0625	7,816.76	7,505.66	311.10	(295.20)	(5.3862)	200.56	199.27	1.29	(0.00)
6	0.875	5,316.08	5,000.00	316.08	(295.20)	(7.0732)	200.05	200.45	-0.40	(0.00)
7	0.6875	2,819.70	2,519.19	300.51	(295.20)	(1.7988)	199.71	198.46	1.25	(0.00)
8	0.50	361.87	0.00	361.87	(295.20)	(22.5847)	196.63	201.54	-4.91	(0.00)

Note that the estimated values of the torsion-induced components, $\{M_i^T, P_i^T\}$, listed in table 15 are practically identical to the values of $\{M_i^T, P_i^T\}$ listed in table 14. This result shows that either method can be used to obtain the torsion-induced components, $\{M_i^T, P_i^T\}$.

3. Determination of Torsion Stiffness, $(GK)_i$

For determination of the cross-sectional torsion stiffness, $(GK)_i$, a clockwise (positive) torque of $T = 50 \times w = 850$ in-lb was applied at swept wing-box tip. It is important to mention that the counterclockwise (negative) torque of $T = -50 \times w = -850$ in-lb did also produce identical values of $(GK)_i$.

Figure 25 shows the plots of the front and rear deflections, $\{y_i, y_i'\}$, averaged deflection, $\bar{y}_i = (y_i + y_i')/2$, and cross-sectional twist angles, $\phi_i^T (> 0)$, induced by the clockwise torque of $T = 50 \times w = 850$ in-lb. The non-zero averaged deflection, $\bar{y}_i$, indicates the magnitude of bending deflections induced by torsion because of the swept effect.

Using the given beam depth factor, c_i, the applied torques, T_i[$= T = 50 \times w = 850$ in-lb], and the cross-sectional twist angles, ϕ_i^T (in reference to surfaces slanted by β deg with respect to x-axis (fig. 18) given in figure 25, the apparent torsion stiffness, $(GK)_i$ were calculated from equation (5), and are listed in table 16.

Table 16. Apparent torsion stiffness $(GK)_i$ for depth-tapered swept wing box determined from the loading condition of clockwise torque, $T = 50 \times w = 850$ in-lb, at wing box tip; $n = 8$, $l = 100$ in, $\Delta l = l/n = 12.5$ in.

i	c_i, in	$\phi \times 10^{-3}$, rad [eq. (6)]	$(\phi_i - \phi_{i-1}) \times 10^{-3}$, rad	$(GK)_i \times 10^7$, lb-in^2 [eq. (5), swept]	(table 7, un-swept)	(diff., %)	T_i, in-lb [from eq. (9)] = applied
0	2.000	0.000000	----------	5.073052	(5.059234)	(0.2731)	850
1	1.8125	0.209440	0.209440	5.073052	(5.059234)	(0.2731)	850
2	1.625	0.537649	0.328209	3.237266	(3.344876)	(3.2172)	850
3	1.4375	0.950594	0.412945	2.572982	(2.595249)	(0.8580)	850
4	1.25	1.485293	0.534699	1.987099	(2.011389)	(1.2076)	850
5	1.0625	2.206183	0.720890	1.473873	(1.498985)	(1.6753)	850
6	0.875	3.230011	1.023828	1.037772	(1.058138)	(1.9247)	850
7	0.6875	4.798556	1.568545	0.677379	(0.693902)	(2.3812)	850
8	0.5	7.379479	2.580923	0.411674	(0.422113)	(2.4730)	850

In table 16 the values of $(GK)_i$ for un-swept wing box taken from table 7 are also listed (in parentheses) for comparison. Note that the values of the apparent $(GK)_i$ of the swept wing box are quite close to the corresponding values of the strain-determined $(GK)_i$ of the un-swept wing box. Note also from table 16 that the operational torques, T_i, listed in the last column were calculated from equation (9) using the apparent $(GK)_i$. The estimated values of T_i are exactly the same as the applied beam tip torque (that is, $T_i = T = 850$ in-lb), implying that one can have confidence in using the apparent $(GK)_i$ for estimating the operational torques.

Figure 26 shows the stepwise plot of the apparent $(GK)_i$ listed in table 16, because of a finite number of small domains. The continuous curve shown in figure 26 is for the limit case when the domain number reaches infinity (that is, $n \to \infty$).

4. Estimations of Operational Torques, T_i^{P+T}

In this section, the pre-determined apparent shear stiffness, $(GK)_i$ listed in table 16, were used to estimate the operational torques, T_i^{P+T}, for combined loading case of bending load, $P = 200$ lb, and counterclockwise torque, $T = -100 \times w = -1{,}700$ in-lb, applied at the wing-box tip.

The combined-load-induced operational torques, T_i^{P+T}, contain the P-induced torques, T_i^P, and T-induced torques, T_i^T [that is, $T_i^{P+T} = T_i^P + T_i^T$]. In reality, T_i^{P+T} are actually felt by the structure, however, in checking the accuracies the estimated operational torques, T_i^{P+T}, the accuracies of component torques, T_i^P, T_i^T were also checked.

4.1. T-Induced Torques, T_i^T

In this section, the pre-determined apparent $(GK)_i$ (table 16) were used to calculate the operational torque components, T_i^T, induced by the torque, $T = -100 \times w = -1{,}700$ in-lb.

Figure 27 shows the plots of the total cross-sectional twist angles, $\phi_i^{P+T} (< 0)$ induced by the current combined bending and torsion loading (taken from figure 23), and the cross-sectional twist angles, $\phi_i^P (< 0)$, induced by the upward bending load, $P = 200$, only (taken from figure 21).

Because of the bending-induced cross-sectional twist angle, ϕ_i^P (fig. 27), in the calculations of the torsion-induced torque components, T_i^T, for the current combined loading case, the bending-induced cross-sectional twist angle, ϕ_i^P, must be removed from the total cross-sectional twist angle, ϕ_i^{P+T}. Namely the twist angles differential, $\phi_i^T \left(= \phi_i^{P+T} - \phi_i^P \right) (< 0)$ were used in equation (9) to calculate the values of T_i^T. The results are listed in table 17.

Table 17. Estimated T-induced operational torques, T_i^T, based on pre-determined apparent $(GK)_i$ for depth-tapered swept wing box subjected to counterclockwise torque, $T = -100 \times w = -1{,}700$ in-lb, at wing tip; $n = 8$, $l = 100$ in, $\Delta l = l/n = 12.5$ in.

i	c_i, in	ϕ_i^{P+T}, $\times 10^{-3}$ rad (P+T)	ϕ_i^P, $\times 10^{-3}$ rad (P only, table 11)	$\phi_i^T \left(= \phi_i^{P+T} - \phi_i^P \right)$, $\times 10^{-3}$ rad	$\left(\phi_i^T - \phi_{i-1}^T \right)$, $\times 10^{-3}$ rad	$(GK)_i \times 10^7$ lb-in^2 [from table 16]	T_i^T, in-lb (estimated)	(applied)	(error, %)
0	2.0	0.000000	0.000000	0.000000	0.000000	5.073052	-1,766.62	(-1,700)	(3.9188)
1	1.8125	-1.038235	-0.602941	-0.435294	-0.435294	5.073052	-1,766.62	(-1,700)	(3.9188)
2	1.625	-2.665297	-1.589412	-1.075885	-0.643291	3.237266	-1,666.00	(-1,700)	(2.0000)
3	1.4375	-4.619428	-2.717941	-1.901487	-0.825602	2.572982	-1,699.41	(-1,700)	(0.0347)
4	1.25	-6.932997	-3.961765	-2.971232	-1.069745	1.978099	-1,700.55	(-1,700)	(0.0324)
5	1.0625	-9.723388	-5.310882	-4.412506	-1.441274	1.473873	-1,699.40	(-1,700)	(0.0353)
6	0.875	-13.185676	-6.725294	-6.460382	-2.047876	1.037772	-1,700.18	(-1,700)	(0.0106)
7	0.6875	-17.669449	-8.071176	-9.598273	-3.137891	0.677379	-1,700.43	(-1,700)	(0.0253)
8	0.5	-23.976415	-9.214706	-14.761709	-5.163436	0.411674	-1,700.52	(-1,700)	(0.0306)

Note from the last column of table 17 that the errors (in view of applied torque, $T = -1{,}700$ in-lb) for the estimated T-induced operational torques, T_i^T, are in the negligible range of (0.0106 ~ 3.9188) percent. The values of T_i^T listed in table 17 are plotted in figure 28 for graphical comparison with the applied torque, $T = -1{,}700$ in-lb. Note that, except for the fixed end region where the estimated data points are slightly off, the rest of the data points of the estimated T-induced operational torques T_i^T (dashed curve with open circular symbols) pictorially fell on top of the $T = -1{,}700$ in-lb applied torque line (solid line with solid circular symbols), giving confidence in using the new method for structure operational loads (torques) estimations.

4.2. *P*-Induced Torques, T_i^P

As shown in figure 21, the swept effect caused the point load, $P = 200$ lb, at wing-box tip to induce counterclockwise cross-sectional rotations (that is, $\phi_i^P < 0$). Therefore, in this section, the pre-determined apparent $(GK)_i$ (table 16) will be used to calculate the P-induced operational torques, T_i^P. The P-induced applied torques, T_i^P, can be expressed as equations (15) and (16):

For T_i^P at domain junctures:

$$T_i^P = -P(l\sin\beta)\left(1-\frac{i}{n}\right) = -3{,}472.96\times\left(1-\frac{i}{n}\right) \text{ (in-lb)} \qquad (i = 0,1,2,3,....,n) \tag{15}$$

For T_i^P at domain centers (T_i^P constant over the domain):

$$T_i^P = -P(l\sin\beta)\frac{1}{2}\left[\left(1-\frac{i}{n}\right)+\left(1-\frac{i-1}{n}\right)\right] = -3{,}472.96\times\frac{1}{2}\left[\left(1-\frac{i}{n}\right)+\left(1-\frac{i-1}{n}\right)\right] \text{ (in-lb)} \qquad (i = 1,2,3,....,n) \tag{16}$$

Using the strain-determined apparent $(GK)_i$ of table 16 and the P-induced cross-sectional twist angle, ϕ_i^P, of figure 21, one can calculate the P-induced operational torques, T_i^P, using equation (9). The results are listed in table 18.

Table 18. Estimated P-induced operational torques, T_i^P, induced by point load, $P = 200$ lb, at tip of depth-tapered swept wing box; $n = 8$, $l = 100$ in, $\Delta l = l/n = 12.5$ in.

i	c_i, in	$\phi_i^P, \times 10^{-3}$ rad (P only, table 11)	$\left(\phi_i^P - \phi_{i-1}^P\right), \times 10^{-3}$ rad (differential)	$(GK)_i, \times 10^7$ lb-in^2 (from table 16)	T_i^P, in-lb (estimated)	[applied, eq. (16)]	(error, %)
0	2.000	0.000000	0.000000	5.073052	--------	(-3,472.96)	(--------)
1	1.8125	-0.602941	-0.602941	5.073052	-2,447.00	(-3,255.90)	(24.8441)
2	1.625	-1.589412	-0.986471	3.237266	-2,554.78	(-2,821.78)	(9.4621)
3	1.4375	-2.717941	-1.128529	2.572982	-2,322.95	(-2,387.66)	(2.7102)
4	1.25	-3.961765	-1.243824	1.987099	-1,977.28	(-1,953.54)	(1.2152)
5	1.0625	-5.310882	-1.349117	1.473873	-1,590.74	(-1,519.42)	(4.6939)
6	0.875	-6.725294	-1.414412	1.037772	-1,174.28	(-1,085.30)	(8.1987)
7	0.6875	-8.071176	-1.345882	0.677379	-729.34	(-651.18)	(12.0028)
8	0.5	-9.214706	-1.143530	0.411674	-376.61	(-217.06)	(73.5050)

Note from table 18 that the estimation errors for T_i^P (last column) are somewhat discouraging near the wing-box root and tip regions.

4.3. Combined-Load-Induced Torques, T_i^{P+T}

In this section, the pre-determined apparent $(GK)_i$ (table 16) will be used to estimate the operational torques, T_i^{P+T}, for a loading case of the depth-tapered wing box subjected to combined point load, $P = 200$ lb, and counterclockwise torque, $T = -100 \times w = -1{,}700$ in-lb, at the wing-box tip. The operational torques, T_i^{P+T}, contain P-induced torque components, T_i^P, and T-induced torque components, T_i^T (that is, $T_i^{P+T} = T_i^P + T_i^T$). For a current combined loading case, the combined applied torques can be expressed as equations (17) and (18) :

For T_i^{P+T} at domain junctures:

$$T_i^{P+T} = T_i^P + T_i^T = \underbrace{-Pl(\sin\beta)\left(1-\frac{i}{n}\right)}_{P\text{-induced torque}} + \underbrace{T_i^T}_{\substack{T-\text{induced}\\ \text{torque}}} = -3{,}472.96 \times \left(1-\frac{i}{n}\right) - 1{,}700 \ \text{(in-lb)} \qquad (i = 0,1,2,3,\ldots,n) \tag{17}$$

For T_i^{P+T} at domain centers (T_i^{P+T} constant over the domain):

$$T_i^{P+T} = T_i^P + T_i^T = \underbrace{-Pl(\sin\beta)\frac{1}{2}\left[\left(1-\frac{i}{n}\right)+\left(1-\frac{i-1}{n}\right)\right]}_{P\text{-induced torque}} + \underbrace{T_i^T}_{\substack{T-\text{induced}\\ \text{torque}}} = -3{,}472.96 \times \left(\frac{1}{2}\right)\left[\left(1-\frac{i}{n}\right)+\left(1-\frac{i-1}{n}\right)\right] - 1{,}700 \ \text{(in-lb)} \qquad (i = 1,2,3,\ldots,n) \tag{18}$$

For the current combined loading case of bending load, $P = 200$ lb, and counter-clock-wise torque, $T = -100 \times w = 1{,}700$ in-lb, at the swept wing-box tip, the values of the strain-determined apparent $(GK)_i$ of table 16 and the cross-sectional twist angle, $\phi_i^{P+T} (< 0)$, of figure 23 can be used to calculate the total operational torque, T_i^{P+T}, using equation (9). The results are listed in table 19.

Table 19. Estimated operational torque, T_i^{P+T}, based on strain-determined $(GK)_i$ for depth-tapered swept wing box subjected to combined bending load, $P = 200$ lb, and counter-clock-wise torque, $T = -100 \times w = -1{,}700$ in-lb, at wing tip; $n = 8$, $l = 100$ in, $\Delta l = l/n = 12.5$ in.

i	c_i, in	ϕ_i^{P+T}, $\times 10^{-3}$ rad ($P+T$)	$\left(\phi_i^{P+T} - \phi_{i-1}^{P+T}\right)$, $\times 10^{-3}$ rad (differential)	$(GK)_i$, $\times 10^7$ lb-in^2 (from table 16)	T_i^{P+T}, in-lb (estimated)	[applied, eq. (18)]	(error, %)
0	2.0	0.000000	0.000000	5.073052	----------	(-5,172.96)	(--------)
1	1.8125	-1.038235	-1.038235	5.073052	-4,213.62	(-4,955.90)	(14.9777)
2	1.625	-2.665297	-1.627062	3.237266	-4,213.79	(-4,521.78)	(6.8113)
3	1.4375	-4.619428	-1.954131	2.572982	-4,022.36	(-4,087.66)	(1.5975)
4	1.25	-6.932997	-2.313569	1.987099	-3,677.83	(-3,653.54)	(0.6648)
5	1.0625	-9.723388	-2.790391	1.473873	-3,290.15	(-3,219.42)	(2.1970)
6	0.875	-13.185676	-3.462288	1.037772	-2,874.45	(-2,785.30)	(3.2007)
7	0.6875	-17.669449	-4.483773	0.677379	-2,429.77	(-2,351.18)	(3.3426)
8	0.5	-23.976415	-6.306966	0.411674	-2,077.13	(-1,917.06)	(8.3498)

Note from table 19 that the errors of estimated operational torques, T_i^{P+T}, are fairly good except for the regions near the fixed and free ends.

Figure 29 shows the plots of estimated T_i^{P+T} (table 18) and estimated T_i^P (table 17). The applied $\{T_i^{P+T}, T_i^P\}$ curves (straight lines) (tables 17, and 18) are also shown for comparison. The estimated values of $\{T_i^{P+T}, T_i^P\}$ compare fairly well with the applied $\{T_i^{P+T}, T_i^P\}$ curves (straight lines) in the outboard region. However, the two estimated $\{T_i^{P+T}, T_i^P\}$ curves started to divert from the applied $\{T_i^{P+T}, T_i^P\}$ curves as the wing root is approached. This data deviation could be attributed to the increasing errors of ϕ_i near the wing root. Remember that ϕ_i is calculated from equation (6) using the deflection-differential, $\{y_i - y_i'\}$, between the front and rear strain-sensing lines. As the wing root is approached, both $\{y_i, y_i'\}$ become very small, causing the error of $\{y_i - y_i'\}$ (small number minus another small number) to increase and, therefore, affect the accuracy of ϕ_i. Increasing the strain-sensing stations could improve the accuracies of ϕ_i. More study of this accuracy problem is currently under way.

Note from figure 29 that the vertical distances between T_i^P and T_i^{P+T} curves will graphically give the T-induced component torque, T_i^T 1,700 in-lb.

From tables 17, 18, and 19, one can verify that the summations of the component torques, $\{T_i^P, T_i^T\}$, indeed, equal to the total operational torques, T_i^{P+T} (that is, $T_i^{P+T} = T_i^P + T_i^T$).

Generic Long-Span Wing

The fifth structure considered was a generic long-span wing, which is a doubly- (horizontally and vertically) tapered long cantilever beam-like structure (fig. 30). The dimensions of the generic long-span wing with length, l, chord-wise separation distances of strain-sensing stations at wing root and wing tip, $\{w_0, w_n\}$ (fig. 31), and wing root and wing tip maximum depths, $\{(h_0)_{max}, (h_n)_{max}\}$, are listed in table 20.

Table 20. Dimensions of generic long-span wing.

l, in	w_0, in	w_n, in	$(h_o)_{max}$, in	$(h_n)_{max}$, in
360.0	64.8	28.8	12.96	5.76

Figure 30 shows the SPAR finite-element model generated for the double-tapered generic long-span wing. This SPAR model has 3,636 nodes and 6,917 four-node bending elements. For each skin (lower or upper), there are 101 nodes in the span-wise direction, and 18 nodes in the chord-wise direction. The model is subjected to a typical combined loading condition of bending load, $P = 200$ lb, and clockwise torque, $T = 1{,}000 \times w_n = 1{,}000 \times 28.8 = 28{,}800$ in-lb, at the wing tip (fig. 30).

As shown in figure 31, the two-line strain-sensing system is on the upper convex surface. The dimensions of the depth factors, $\{c_i, c_i'\}$, respectively along the front and rear strain-sensing lines are assumed to be linearly decreasing from the wing root toward the wing tip. Each strain-sensing line has $n = 8$ evenly spaced strain-sensing intervals. The dimensions of the wing root and wing tip depth factors $[\{c_0, c_0'\}, \{c_n, c_n'\}]$ are listed in table 21.

Table 21. Depth factors associated with front and rear strain-sensing stations at wing root and wing tip for generic long-span wing.

Wing root		Wing tip	
c_0, in (front)	c_0', in (rear)	c_n, in (front)	c_n', in (rear)
6.4051 (= 0.5380 h_0)	7.3899 (= 0.5912 h_0')	2.8467 (= 0.5380 h_n)	3.2844 (= 0.5912 h_n')

In table 21, $\{h_0, h_0'\}$ and $\{h_n, h_n'\}$ are the wing root depth and wing tip depths associated respectively with the front and rear strain-sensing stations (fig. 31).

1. Determination of Bending Stiffness, $(EI)_i$

In step 1 of determining the bending stiffness, $(EI)_i$, a point load, $P = 200$ lb, was applied at the generic wing tip (between front and rear strain-sensing lines, fig. 30). For the present loading case, the applied moments, M_i, will be $M_i = M_0(1 - i/n) = 72{,}000 \times (1 - i/n)$ in-lb [eq. (3)]. Because the strain-sensing lines are located on the upper surface, the positive moment, M_i, will induce negative surface strains. In order to use equations (1) – (4) in the subsequent operational load estimations, negative signs of the surface strains were neglected. Figure 32 shows the plots of the induced surface strains, $\{\varepsilon_i, \varepsilon_i'\}$, and deflections, $\{y_i, y_i'\}$, along the two strain-sensing lines. The magnitudes of the front and rear strains, $\{\varepsilon_i, \varepsilon_i'\}$, are slightly different even under bending loading because of different depth factors for the front and rear strain-sensing lines (that is, $c_i \neq c_i'$, table 21). However, the deflections, $\{y_i, y_i'\}$, respectively along the front and rear strain-sensing lines are practically coincidental. Two methods were used to determine the values of $(EI)_i$ for the generic long-span wing as described in the following sections.

1.1. Method 1–Averaged Geometry and Strains

Method 1 is comprised of using the averaged depth factor, $\bar{c}_i \equiv (c_i + c_i')/2$, and the averaged strains, $\bar{\varepsilon}_i \equiv (\varepsilon_i + \varepsilon_i')/2$ (absolute values), obtained from figure 32, and the known cross-sectional moment, $M_i [= 72{,}000 \times (1 - i/n)]$ in-lb. The values of the bending stiffness, $(EI)_i$, were then calculated from equation (2) by replacing $\{\varepsilon_i, c_i\}$ with $\{\bar{\varepsilon}_i, \bar{c}_i\}$. The results are listed in table 22.

Table 22. Bending stiffness, $(EI)_i$, calculated from eq. (2) using averaged depth factors, $\bar{c}_i$, and averaged strains, $\bar{\varepsilon}_i$, for generic long-span wing subjected to bending load, $P = 200$ lb, at wing tip; $n = 8$, $l = 360$ in, $\Delta l = l/n = 45$ in, $M_0 = Pl = 72{,}000$ in-lb.

i	c_i, in	c_i', in	$\bar{c}_i$, in (averaged)	ε_i, $\times 10^{-3}$ in/in (SPAR)	ε_i', $\times 10^{-3}$ in/in (SPAR)	$\bar{\varepsilon}_i$, $\times 10^{-3}$ in/in (averaged)	M_i/M_0 (known)	$(EI)_i[= M_i(\bar{c}_i/\bar{\varepsilon}_i)]$, $\times 10^7$, lb-in^2 [eq. (2)]
0	6.4051	7.3899	6.8975	0.551429	0.643810	0.597620	8/8	83.0997
1	5.9693	6.8767	6.4230	0.564762	0.639048	0.601905	7/8	67.2281
2	5.5155	6.3635	5.9395	0.566190	0.641429	0.603810	6/8	53.1182
3	5.0707	5.8503	5.4605	0.558095	0.632381	0.595238	5/8	41.2814
4	4.6259	5.3371	4.9815	0.536190	0.607143	0.571667	4/8	31.3704
5	4.1811	4.8240	4.5026	0.492381	0.557143	0.524762	3/8	23.1667
6	3.7363	4.3108	4.0236	0.410000	0.464762	0.437381	2/8	16.5587
7	3.2915	3.7976	3.5446	0.263810	0.299048	0.281429	1/8	11.3355
8	2.8467	3.2844	3.0656	0.000000	0.000000	0.000000	0/8	7.4971*

*Three-points extrapolation [eq. (10)].

1.2. Method 2–Averaged Bending Stiffness

Method 2 is to determine the individual bending stiffness, $\{(EI)_i, (EI)_i'\}$ from equation (2) using $[\{\varepsilon_i, c_i\}, \{\varepsilon_i', c_i'\}]$ respectively for the front and rear strain-sensing lines, and the known cross-sectional moments, $M_i[= 72{,}000\times(1 - i/n)]$. The calculated individual bending stiffness, $\{(EI)_i, (EI)_i'\}$ and the averaged bending stiffness $(\overline{EI})_i\{\equiv [(EI)_i + (EI)_i']/2\}$ are listed in table 23.

Table 23. Averaged bending stiffness, $(\overline{EI})_i$, for generic long-span wing subjected to bending load, $P = 200$ lb, at the wing tip; $l = 360$ in, $\Delta l = l/n = 45$ in, $M_0 = Pl = 72{,}000$ in-lb.

i	c_i, in	c_i', in	ε_i, $\times 10^{-3}$ in/in (SPAR)	ε_i', $\times 10^{-3}$ in/in (SPAR)	M_i/M_0 (known)	$(EI)_i$, $\times 10^7$ lb-in^2 |-----calculated from eq. (2)-----|	$(EI)_i'$, $\times 10^7$ lb-in^2	$(\overline{EI})_i$, $\times 10^7$ lb-in^2 (averaged)
0	6.4051	7.3899	0.551429	0.643810	8/8	83.6313		82.6444	83.1379
1	5.9693	6.8767	0.564762	0.639048	7/8	66.5884		67.7934	67.1909
2	5.5155	6.3635	0.566190	0.641429	6/8	52.6037		53.5724	53.0881
3	5.0707	5.8503	0.558095	0.632381	5/8	40.8858		41.6305	41.2582
4	4.6259	5.3371	0.536190	0.607143	4/8	31.0585		31.6459	31.3522
5	4.1811	4.8240	0.492381	0.557143	3/8	22.9273		23.3778	23.1526
6	3.7363	4.3108	0.410000	0.464762	2/8	16.4033		16.7234	16.5634
7	3.2915	3.7976	0.263810	0.299048	1/8	11.2291		11.4291	11.3291
8	2.8467	3.2844	0.000000	0.000000	0/8	7.4047*		7.4949*	7.4498*

*Three-points extrapolation [eq. (10)].

The values of strain-determined bending stiffness, $(EI)_i$, listed in table 22 and the averaged bending stiffness, $(\overline{EI})_i$, listed in table 23 are plotted in figure 33. Note that the bending stiffness $\{(EI)_i, (\overline{EI})_i\}$ decreased nonlinearly toward the wingtip because of the doubly-tapered structure. The two bending stiffness curves are graphically coincidental. Therefore, in the following operational load predictions, only the values of $(EI)_i$ determined by method 1 (table 22) were used.

2. Estimations of Operational Moments and Shear Loads, $\{M_i, P_i\}$

In the following sections, the strain-determined bending stiffness, $(EI)_i$, will be used to estimate operational loads, $\{M_i, P_i\}$, associated with other types of loading conditions. The loading conditions considered were concentrated loads and distributed loads.

2.1. Concentrated Loads

The strain-determined $(EI)_i$ of table 22 were used in the estimations of the operational moments and shear loads, $\{M_i, P_i\}$, for the loading case of combined bending load, $P = 200$ lb, and clockwise torque, $T = 1000 \times 28.8 = 28{,}800$ in-lb, at the wingtip. For the present loading case, the applied moments, M_i, will be $M_i[= 72{,}000 \times (1 - i/n)]$ in-lb.

Figure 34 shows the plots of the magnitudes of the induced surface strains, $\{\varepsilon_i, \varepsilon_i'\}$, and deflections, $\{y_i, y_i'\}$, for the current combined loading case.

Using the known depth factors, $\{c_i, c_i'\}$, the surface strains, $\{\varepsilon_i, \varepsilon_i'\}$, of figure 34, and the strain-determined $(EI)_i$ in table 22, the estimated operational bending and shear loads, $\{M_i, P_i\}$, were calculated respectively from equations (1) and (4). The results are listed in table 24.

Table 24. Estimated operational moments and shear loads $\{M_i, P_i\}$ calculated from eq. (4) based on the strain-determined $(EI)_i$ for generic long-span wing subjected to combined bending load, $P = 200$ lb, and torque, $T = 1{,}000 \times w_n = 28{,}800$ in-lb, at wing tip; $n = 8$, $l = 360$ in, $\Delta l = l/n = 45$ in, applied $M_i = 72{,}000 \times (1 - i/n)$ in-lb.

i	c_i, in	c_i', in	$\bar{c}_i$, in	$\varepsilon_i, \times 10^{-3}$ in/in (SPAR)	$\varepsilon_i', \times x10^{-3}$ in/in (SPAR)	$\bar{\varepsilon}_i, \times 10^{-3}$ in/in (averaged)	$(EI)_i, \times 10^7$ lb-in^2 (from table 22)	$M_i \left[= (EI)_i \left(\frac{\bar{\varepsilon}_i}{\bar{c}_i}\right)\right]$, $\times 10^4$ in-lb (predicted) (error, %)	M_i (applied)	P_i, lb (predicted) (% error)	P_i (applied)
0	6.4051	7.3899	6.8795	0.592000	0.623810	0.607905	83.0997	7.3239 (1.7200)	(7.2000)	214.67 (7.3350)	(200.00)
1	5.9693	6.8767	6.4230	0.582071	0.632724	0.607398	67.2281	6.3575 (0.9127)	(6.3000)	214.67 (7.3350)	(200.00)
2	5.5155	6.3635	5.9395	0.573333	0.646667	0.610000	53.1182	5.4554 (1.0259)	(5.4000)	200.47 (0.2350)	(200.00)
3	5.0707	5.8503	5.4605	0.568571	0.637143	0.602857	41.2814	4.5576 (1.2800)	(4.5000)	199.52 (0.2400)	(200.00)
4	4.6259	5.3371	4.9815	0.551429	0.612857	0.582143	31.3704	3.6660 (1.8333)	(3.6000)	198.13 (0.9350)	(200.00)
5	4.1811	4.8240	4.5026	0.507619	0.563810	0.535715	23.1667	2.7564 (2.0889)	(2.7000)	202.13 (1.0650)	(200.00)
6	3.7363	4.3108	4.0236	0.429524	0.473333	0.451429	16.5587	1.8578 (3.2111)	(1.8000)	199.69 (0.1550)	(200.00)
7	3.2915	3.7976	3.5446	0.300000	0.300952	0.300476	11.3355	0.9609 (6.7667)	(0.9000)	199.31 (0.3460)	(200.00)
8	2.8467	3.2844	3.0656	0.000000	0.000000	0.000000	7.4971*	0.0000 (0.0000)	(0.0000)	213.53 (6.7650)	(200.00)

* Three-points extrapolation [eq. (10)].

Note from table 24 that the estimation errors of M_i are in the negligible ranges of (0 ~ 1.7200) percent except for near tip region (6.7667 percent error). The estimation errors of P_i are also in a small range of (0.2400 ~ 2.1550) percent excluding the wing root (7.3350 percent error) and wing tip (6.7650 percent error).

In figure 35, the values of the estimated operational moments and shear loads, $\{M_i, P_i\}$, listed in table 24 are plotted for graphical visualizations. The estimated operational moments, M_i (dashed curve with open circular symbols), compared quite well with the applied moments, M_i (solid line with solid circular symbols). The estimated operational shear loads, P_i (dashed curve with open diamond symbols),

compared nicely with the applied load, $P = 200$ lb (horizontal solid line with solid diamond symbols), except for the free end and the fixed end regions where the P_i data points are slightly off.

2.2. Distributed Loads

The values of strain-determined $(EI)_i$ from table 22 were also used to estimate the operational moments and shear loads, $\{M_i, P_i\}$, for the case of a distributed load of 1 lb at each node of the wing lower skin. The distributed load-induced applied moment and shear load, $\{M_i, P_i\}$, at wing cross-section, i, can be written as equations (19) and (20):

$$M_i = \underbrace{F_i}_{\text{Force}} \times \underbrace{\frac{l}{2}\left(1-\frac{i}{n}\right)}_{\text{Moment arm}} = \underbrace{\left[1{,}818\times\left(1-\frac{i}{n}\right)\right]}_{F_i} \times \underbrace{\left[180\times\left(1-\frac{i}{n}\right)\right]}_{\text{Moment arm}} \quad \text{(in-lb)} \qquad (19)$$

$$(i = 0,1,2,3,\ldots,n)$$

$$P_i = \underbrace{\left[1{,}818\times\left(1-\frac{i}{n}\right)\right]}_{\text{Number of nodes}} \times \underbrace{1.0\,\text{lb}}_{\substack{\text{Nodal}\\ \text{force}}} = 1{,}818\times\left(1-\frac{i}{n}\right) \quad \text{(lb)} \qquad (20)$$

$$(i = 0,1,2,3,\ldots,n)$$

In figure 36, the induced surface strains, $\{\varepsilon_i, \varepsilon_i'\}$, and deflections, $\{y_i, y_i'\}$, for the distributed loading case are plotted. Similar to the bending under concentrated load (fig. 32), the rear strains, ε_i', are slightly larger than the associated front strains, ε_i, because of unequal depth ratios (that is, $c_i' > c_i$). The values of the operational moments and shear loads, $\{M_i, P_i\}$, calculated based on the strains, $\{\varepsilon_i, \varepsilon_i'\}$, from figure 36, are listed in table 25. For the distributed load case, the operational moments and shear loads, $\{M_i, P_i\}$, are located at the midpoint of each domain.

Table 25. Estimated moments and shear loads, $\{M_i, P_i\}$, calculated from eq. (4) based on strain determined $(EI)_i$ for generic long-span wing subjected to distributed load of $P = 1$ lb at each lower surface node; $n = 8$, $l = 360$ in, $\Delta l = l/n = 45$ in.

i	$\overline{c}_i$, in	$\varepsilon_i, \times 10^{-3}$ in/in (SPAR)	$\varepsilon_i', \times 10^{-3}$ in/in (SPAR)	$\overline{\varepsilon}_i, \times 10^{-3}$ in/in (averaged)	$(EI)_i, \times 10^7$ lb-in^2 (from table 22)	$M_i[=(EI)_i(\overline{\varepsilon}_i/\overline{c}_i)], \times 10^4$ in-lb (estimated)	(applied)	(error, %)	P_i, lb (estimated)	(applied)	(error, %)
0	6.8975	2.447619	2.910476	2.679084	83.0997	32.2771	(32.7240)	(1.3657)	---------	(1,818.00)	(--------)
									1,614.78	(1,704.38)	(5.2570)
1	6.4230	2.240952	2.538095	2.389524	67.2281	25.0106	(25.0643)	(0.2142)			
									1,467.22	(1,477.13)	(0.6709)
2	5.9395	1.928571	2.188095	2.058333	53.1182	18.4081	(18.4073)	(0.0043)			
									1,243.09	(1,249.88)	(0.5433)
3	5.4605	1.588095	1.801905	1.695000	41.2814	12.8142	(12.7828)	(0.2456)			
									1,018.02	(1,022.63)	(0.4508)
4	4.9815	1.224762	1.390000	1.307381	31.3704	8.2331	(8.1810)	(0.6368)			
									795.38	(796.38)	(0.1256)
5	4.5026	0.847143	0.961905	0.904524	23.1667	4.6539	(4.6018)	(1.1322)			
									569.09	(568.13)	(0.1690)
6	4.0236	0.476191	0.540952	0.508572	16.5587	2.0930	(2.0453)	(2.3322)			
									345.31	(340.88)	(1.2996)
7	3.5446	0.158095	0.179048	0.168572	11.3355	0.5391	(0.5113)	(5.4371)			
									119.80	(113.63)	(5.4299)
8	3.0656	0.000952	0.001905	0.001429	7.4971*	0.0003	(0.0000)	(--------)	--------	(0.00)	(--------)

* Three-points extrapolation [eq. (10)].

In table 25, the values of the applied moments and applied shear loads, $\{M_i, P_i\}$, were calculated respectively from equations (19) and (20). Note from table 25 that the estimation errors of operational M_i^P are in the ranges of (0.0043 ~ 5.4371) percent, and the estimation errors of operational P_i^P are in the small range of (0.6709 ~ 1.2996) percent excluding the wing root region (5.2570 percent error) and the wing tip region (5.4299 percent error).

Figure 37 shows the plots of the estimated and applied operational moments and shear loads, $\{M_i, P_i\}$, for graphical comparisons. Note from figure 37 that the estimated M_i curve (dashed curve with open circular symbols) compares nicely with the applied M_i curve (solid curve with solid circular symbol). The estimated P_i curve (dashed curve with open diamond symbols) also compares nicely with the applied P_i curve (straight line with solid diamond symbols) except for the wing root region where the estimated P_i data point are slightly lower than the corresponding applied P_i value.

3. Determinations of Torsion Stiffness $(GK)_i$

To determine the torsional stiffness $(GK)_i$ of the generic long span wing, a clockwise torque, $T = 1{,}000 \times w_n = 1{,}000 \times 28.8 = 28{,}800$ in-lb, was applied at the wing tip.

Figure 38 shows the plots of the deflections, $\{y_i, y_i'\}$, and cross-sectional twist angle, ϕ_i, induced by the current torsion loading. For the current torsion loading case, the operational torque, T_i, is equal to the applied torque (that is, $T_i = T$).

Using the known torque, $T_i (= T)$, and the cross-sectional twist angles, ϕ_i (fig. 38), the values of $(GK)_i$ were calculated from equation (5) and are listed in table 26.

Table 26. Domain torsional stiffness, $(GK)_i$, of generic long-span wing determined from loading condition of clockwise torque, $T = 1{,}000 \times w_n = 28{,}800$ in-lb, at wing tip; $n = 8$, $l = 360$ in, $\Delta l = l/n = 45$ in.

i	$\phi_i, \times 10^{-3}$ rad [eq. (6)]	$(\phi_i - \phi_{i-1}), \times 10^{-3}$ rad	$(GK)_i, \times 10^7$ lb-in^2 [eq. (5)]	T_i, in-lb [calculated, eq. (9) = applied]
0	0.000000	----------	47.915314	28,800
1	2.704772	2.704772	47.915314	28,800
2	6.572264	3.867492	33.510089	28,800
3	11.209831	4.637567	27.945688	28,800
4	17.206154	5.996323	21.613245	28,800
5	25.224999	8.018845	16.161929	28,800
6	36.266667	11.041668	11.737357	28,800
7	51.924330	15.657663	8.277097	28,800
8	74.440002	22.515672	5.755991	28,800

In the last column of table 26, the values of $T_i = 28{,}800$ in-lb were calculated from equation (9) using the strain-determined $(GK)_i$, and are exactly the same as the applied torques, $T = 28{,}800$ in-lb, confirming the accuracies of the strain-determined $(GK)_i$.

Figure 39 shows the plot of the strain-determined $(GK)_i$ data listed in table 26. The $(GK)_i$ curve for the generic long-span wing is a concave downward because of the doubly-tapered structure.

4. Estimations of Operational Torque, T_i

The pre-determined $(GK)_i$ listed in table 26 were used to estimate the operational torques, T_i, for the combined loading case, for which the generic long-span wing was subjected to bending load, $P = 200$ lb, and clockwise torque, $T = 1{,}000 \times w_n = 28{,}800$ in-lb, at the wing tip.

Figure 40 shows the plots of the displacements, $\{y_i, y_i'\}$, and the cross-sectional twist angles, ϕ_i, induced by the current combined loading.

Using the strain-determined $(GK)_i$ listed in table 26, and the values of ϕ_i shown in figure 40, the operational torque, T_i, were calculated from equation (9). The results are listed in table 27.

Table 27. Estimated operational torques T_i based on strain-determined $(GK)_i$ for generic long-span wing subjected to combined bending load, $P = 200$ lb, and torque, $T = 1{,}000 \times w_n = 28{,}800$ in-lb, at wing tip; $n = 8$, $l = 360$ in, $\Delta l = l/n = 45$ in.

i	c_i, in	ϕ_i, $\times 10^{-3}$ rad [eq. (6)]	$(\phi_i - \phi_{i-1})$, $\times 10^{-3}$ rad	$(GK)_i$, $\times 10^7$ lb-in^2 (from table 26)	T_i, in-lb (estimated)	(applied)	(% error)
0	4.000	0.000000	----------	47.915314	28,161.27	(28,800)	(2.2178)
1	3.625	2.644785	2.644785	47.915314	28,161.27	(28,800)	(2.2178)
2	3.250	6.550378	3.905593	33.510089	29,083.72	(28,800)	(0.9851)
3	2.875	11.239536	4.689158	27.945688	29,120.39	(28,800)	(1.1125)
4	2.500	17.291623	6.052087	21.613245	29,067.83	(28,800)	(0.9300)
5	2.125	25.374644	8.083021	16.161929	29,030.49	(28,800)	(0.8003)
6	1.750	36.493822	11.119178	11.737357	29,002.17	(28,800)	(0.7020)
7	1.375	52.249712	15.755890	8.277097	28,980.67	(28,800)	(0.6273)
8	1.000	74.821043	22.571331	5.755991	28,871.19	(28,800)	(0.2472)

Note from table 27 that the estimated operational torques, T_i, have negligible errors in the range of (0.2472 ~ 2.2178) percent.

In figure 41, the estimated and applied operational torque, T_i, listed in table 27 are plotted for graphical comparisons. Note the estimated data points of T_i (dashed curve with open circular symbols) practically fell on top of the applied torque line, $T = 28{,}800$ in-lb (solid horizontal line with solid circular symbols). The proximity between the estimated and applied torques validated the accuracies of the new method for operational load estimations using distributed surface strains.

CONCLUDING REMARKS

A new method for estimating the operational loads (moments, shear loads, and torques) using distributed surface strains (unidirectional) was presented. The embodied stiffness and load transfer functions were developed for converting surface strains into structural stiffness (bending, torsion) and operational loads. The operational loads estimations require pre-determinations of structural stiffness (true or apparent). Several slender structures (under different loading conditions) were chosen for finite-element accuracy studies of the new method. The key results are listed below:

1. For the slender structures, the bending stiffness determined using distributed surface strains (step one of the new method) agreed quite nicely with the values calculated from the theory of elasticity.
2. The strain-determined stiffness is merely a stepping stone needed for the calculations of the operational loads (moments, shear loads, and torques), and it can be a true stiffness, or an apparent stiffness associated with a particular strain-sensing station configuration.
3. The same strain-sensing configuration must be used to determine both the structural stiffness (step one) and the operational loads (step 2).
4. By using the two-line strain-sensing system with embodied Displacement Transfer Functions, it is possible to determine torsion stiffness and operational torques, and thus eliminate the need for distortion strain gages to sense torsions.
5. For a slender structure with known neutral surface location, the two-line strain-sensing system can be used to estimate all components of the operational loads (bending moments, shear loads, and torques) with sufficient accuracies.
6. For the tapered tube (using a single strain-sensing line) the strain-determined bending stiffness and the estimated operational loads (moments, shear loads) agreed quite nicely with the associated theoretically calculated values.

7. For the un-swept wing box, and the generic long-span wing, the estimated operational loads (bending moments, shear loads, and torques) agreed fairly well with actual applied loads (theoretically calculated loads).
8. For the swept wing box, bending and torsion are coupled (that is, bending induces torsion, and vice versa), and the coupling effect increases with the swept angle. Bending induced a considerable amount of torsion, however, torsion induced only a low level of pure bending, which generates no shear loads.
9. Overall, the new method for estimating operational loads (moments, shear loads, and torques) was found to be fairly accurate, and is very promising for applications to flight load monitoring of aircraft with slender wings.

FIGURES

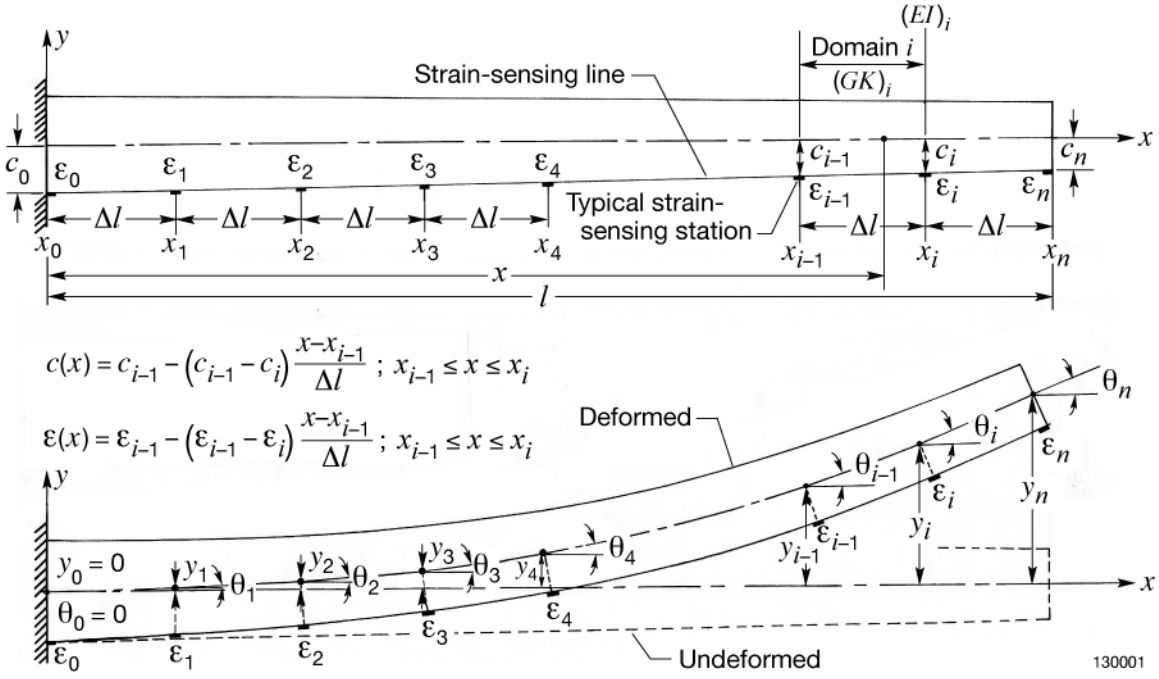

Figure 1. Embedded beam (cross section of any structure) along the strain-sensing line with evenly distributed strain-sensing stations.

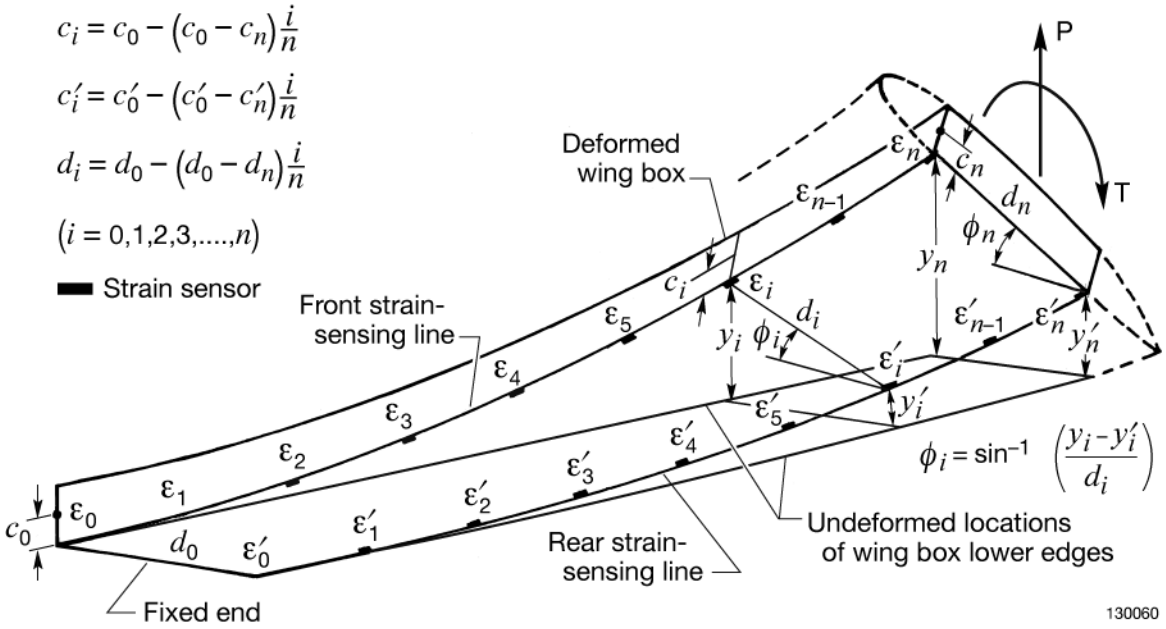

Figure 2. Two-line strain-sensing system for sensing multiple surface strains for deformed shape calculations of tapered cantilever wing box subjected to bending and torsion.

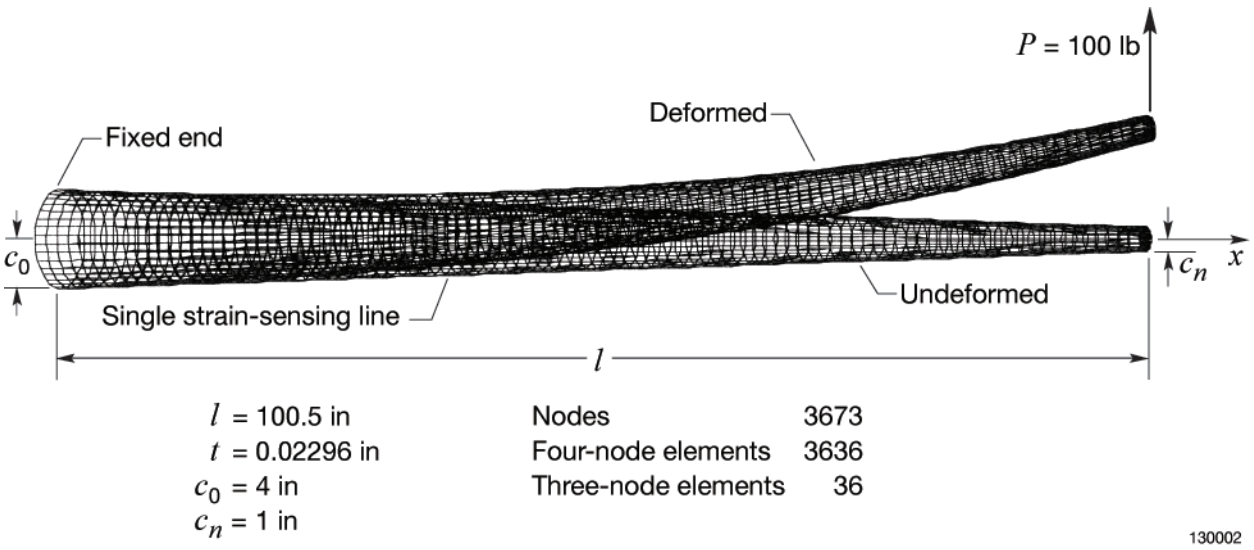

Figure 3. SPAR finite-element model generated for tapered cantilever tubular beam subjected to upward vertical load, P = 100 lb, at beam tip.

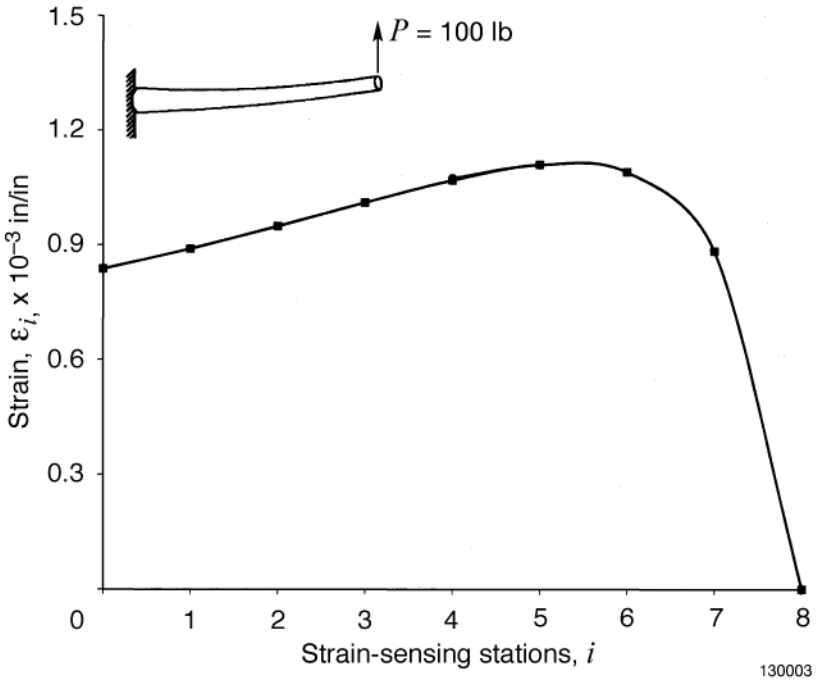

Figure 4. SPAR-generated surface bending strains, ε_i, for tapered cantilever tubular beam subjected to point load, P = 100 lb, at the beam tip.

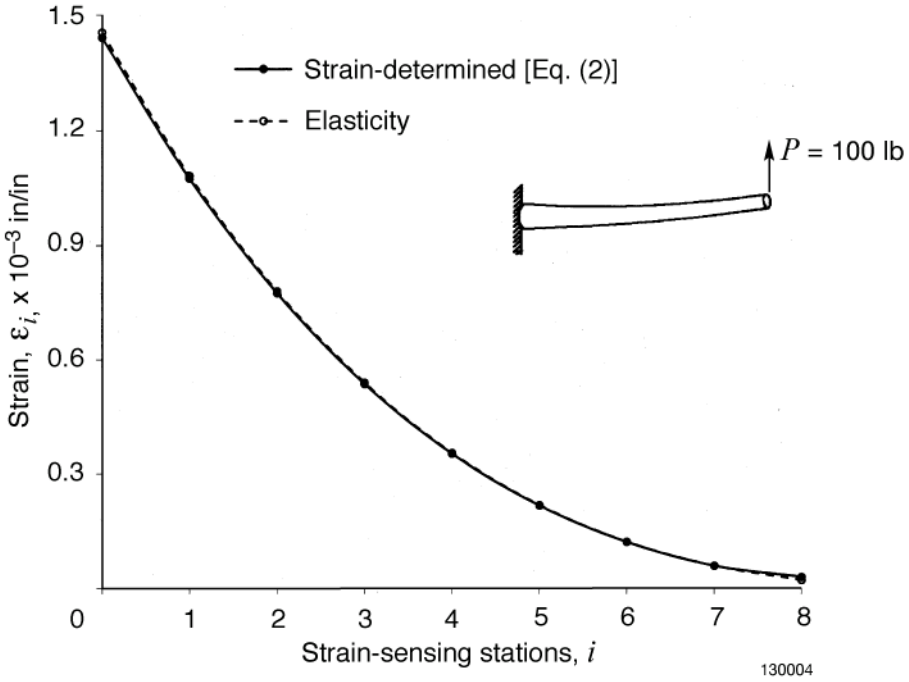

Figure 5. Span-wise plots of strain-determined bending stiffness, $(EI)_i$, and elasticity-calculated bending stiffness, $(EI)_i$, for tapered cantilever tubular beam.

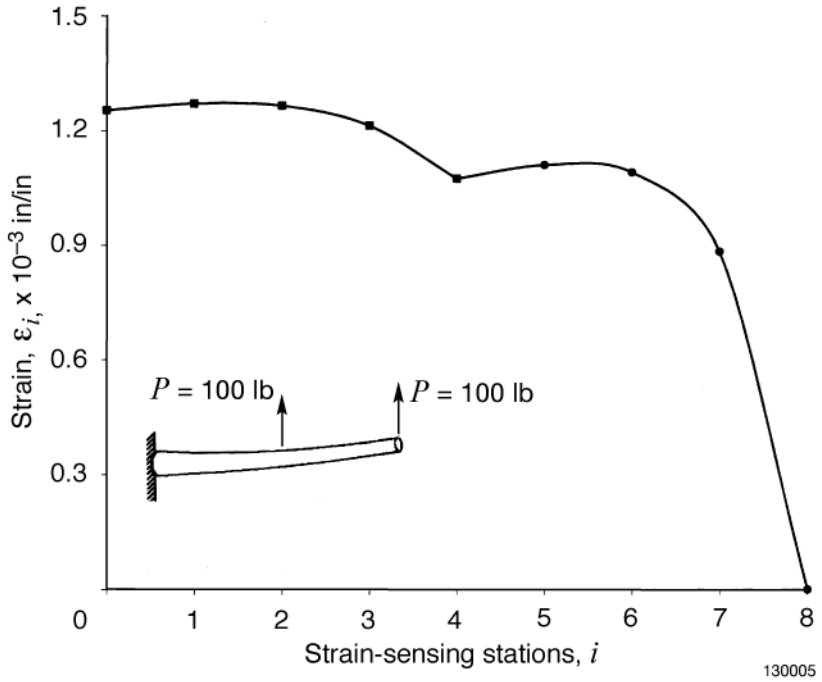

Figure 6. SPAR-generated surface bending strains, ε_i, for tapered cantilever tubular beam subjected to point load, P = 100 lb, at the beam tip and second point load, P = 100 lb, at mid-span.

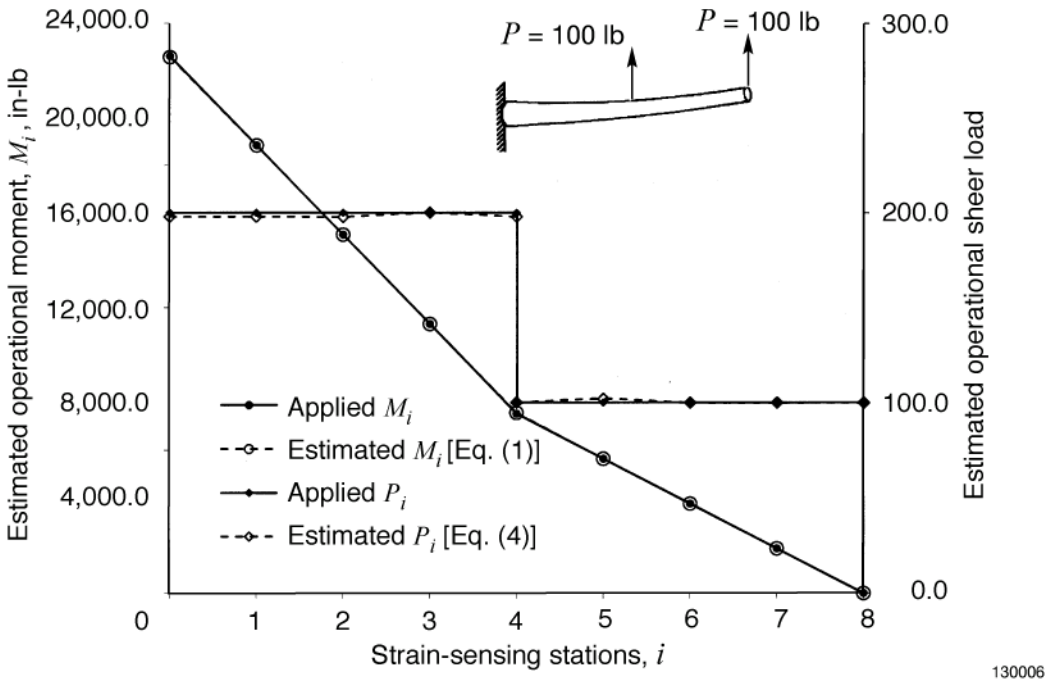

Figure 7. Plots of estimated operational moments and shear load, $\{M_i, P_i\}$, for tapered cantilever tubular beam subjected to point load, P = 100 lb, at the beam tip and second point load, P = 100 lb, at mid-span.

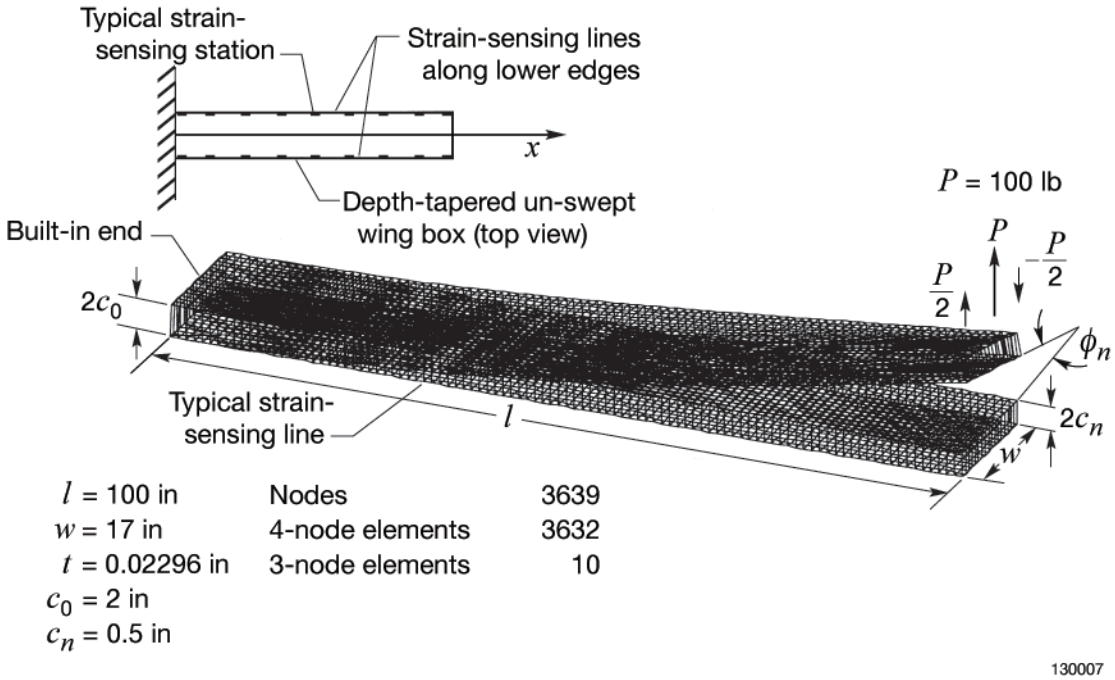

Figure 8. SPAR finite-element model generated for depth-tapered wing box subjected to typical bending load, P = 100 lb, and clockwise torque, $T = 50 \times w$ = 850 in-lb.

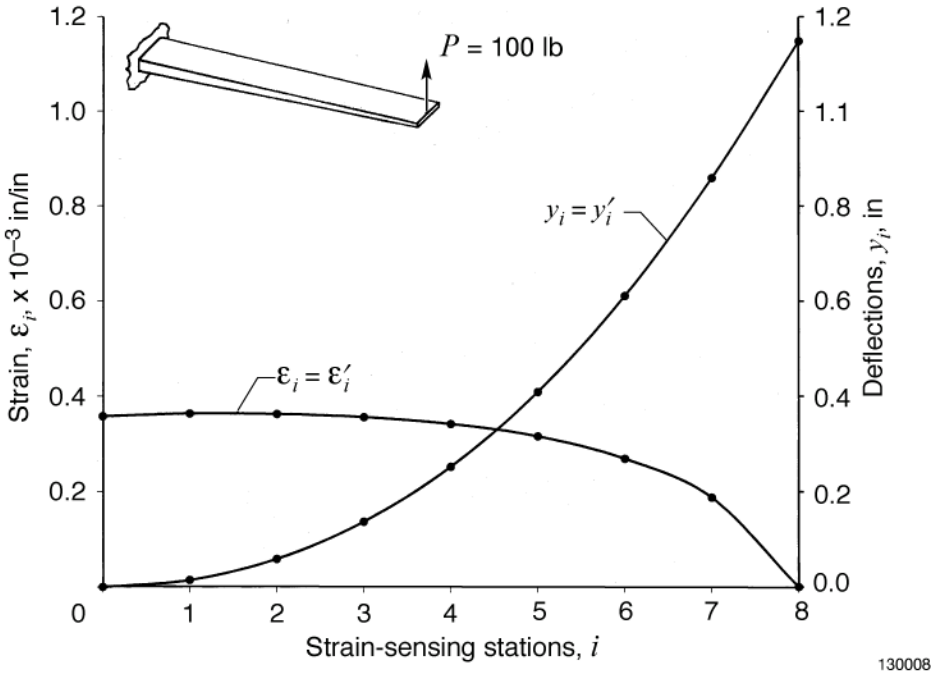

Figure 9. SPAR-generated surface bending strains, $\varepsilon_i(= \varepsilon_i')$, and deflections, $y_i(= y_i')$, for depth-tapered un-swept wing box subjected to point load, P − 100 lb, at wing box tip for determination of bending stiffness, $(EI)_i$.

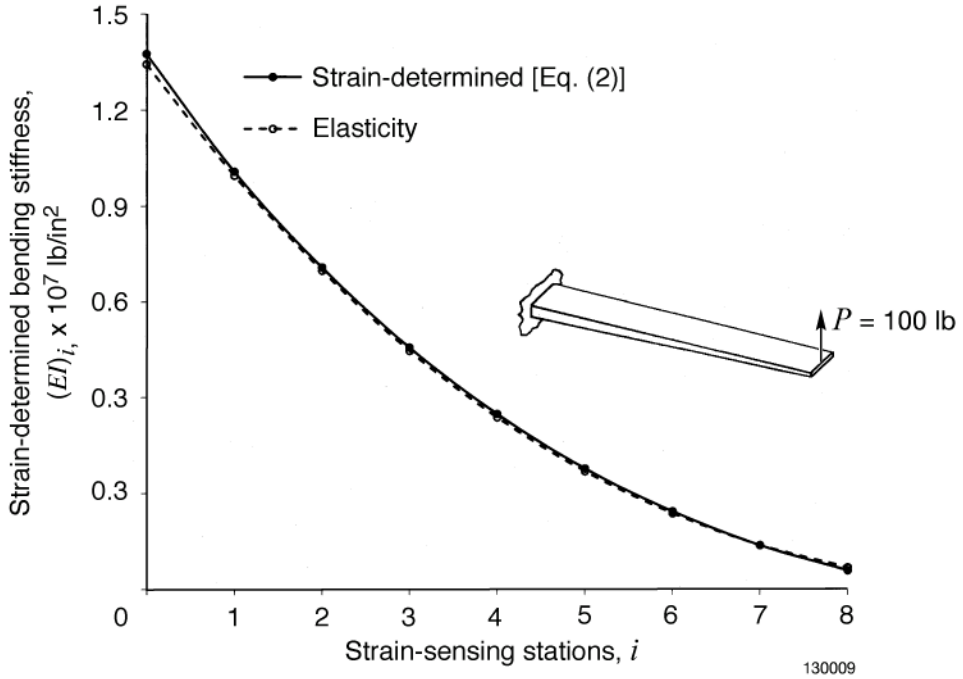

Figure 10. Span-wise plots of strain-determined bending stiffness, $(EI)_i$, for depth-tapered un-swept wing box.

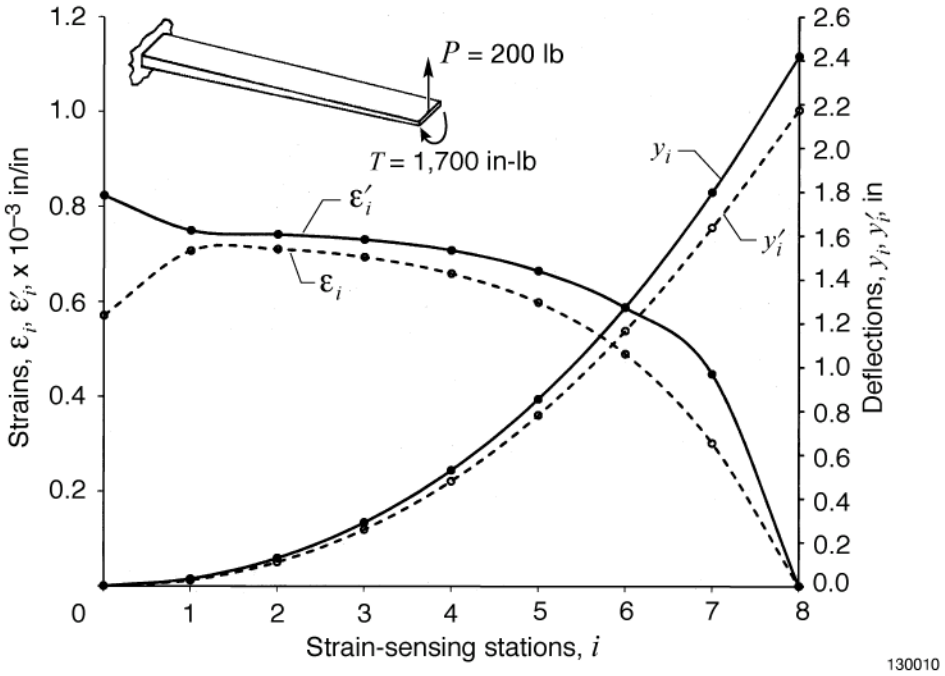

Figure 11. SPAR-generated surface bending strain, $\{\varepsilon_i, \varepsilon_i^{'}\}$and deflections, $\{y_i, y_i^{'}\}$, for depth-tapered un-swept wing box subjected to point load, P = 200 lb, and clockwise torque, $T = 100 \times w$ = 1,700 in-lb, at un-swept wing box tip.

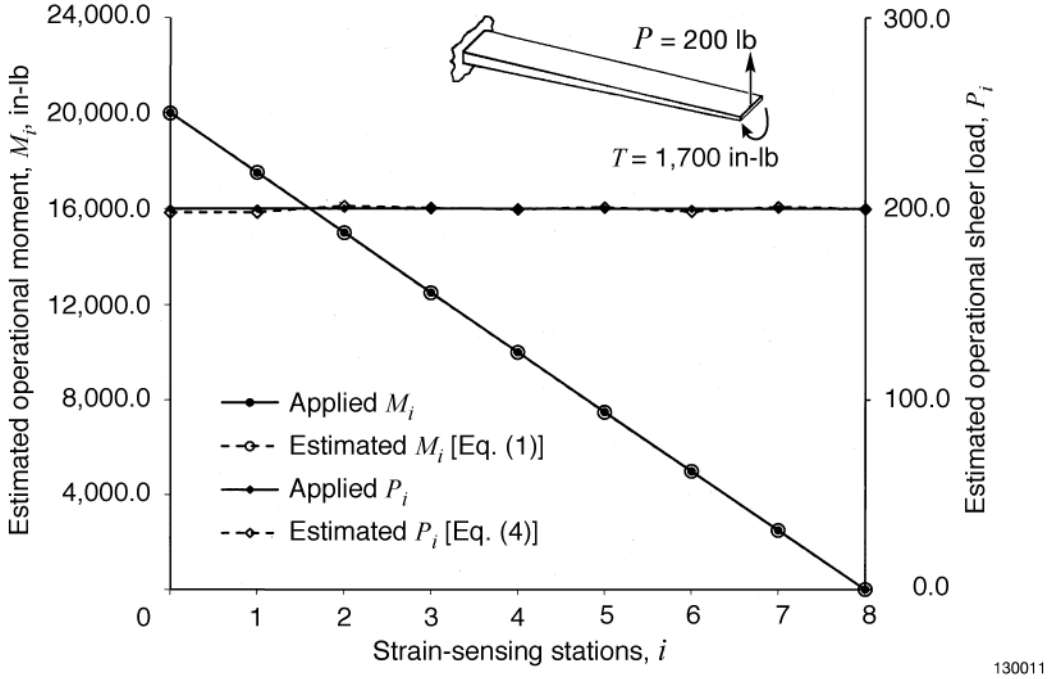

Figure 12. Plots of estimated operational moments and shear loads, $\{M_i, P_i\}$, for depth- tapered un-swept wing box subjected to point load, P = 200 lb, and clockwise torque, $T = 100 \times w$ = 1,700 in-lb, at wing box tip.

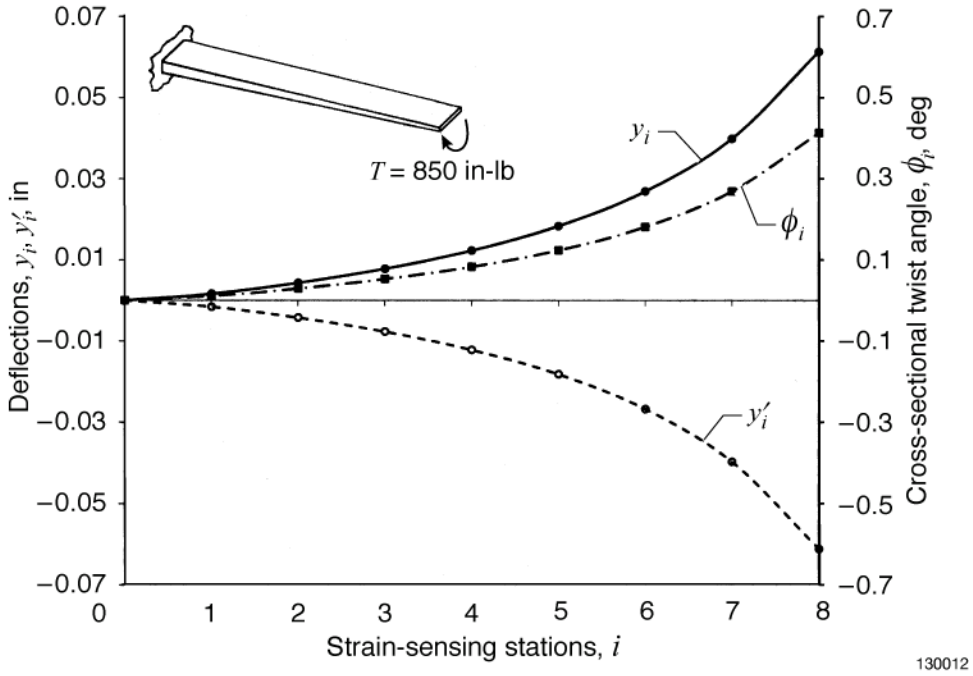

Figure 14. Span-wise plot of strain-determined torsional stiffness, $(GK)_i$, for depth-tapered un-swept wing box.

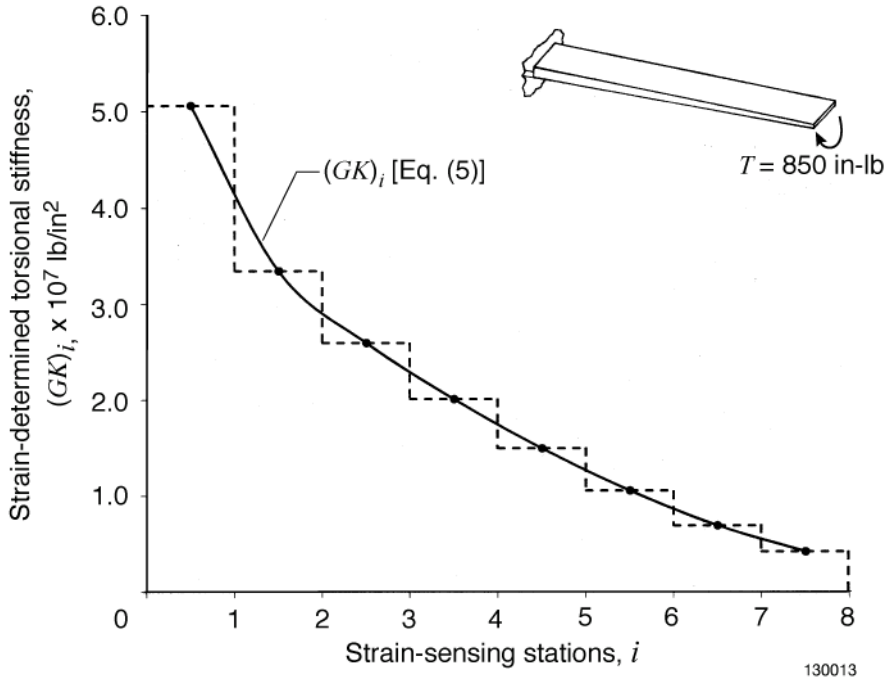

Figure 14. Span-wise plot of strain-determined torsional stiffness, $(GK)_i$, for depth-tapered un-swept wing box.

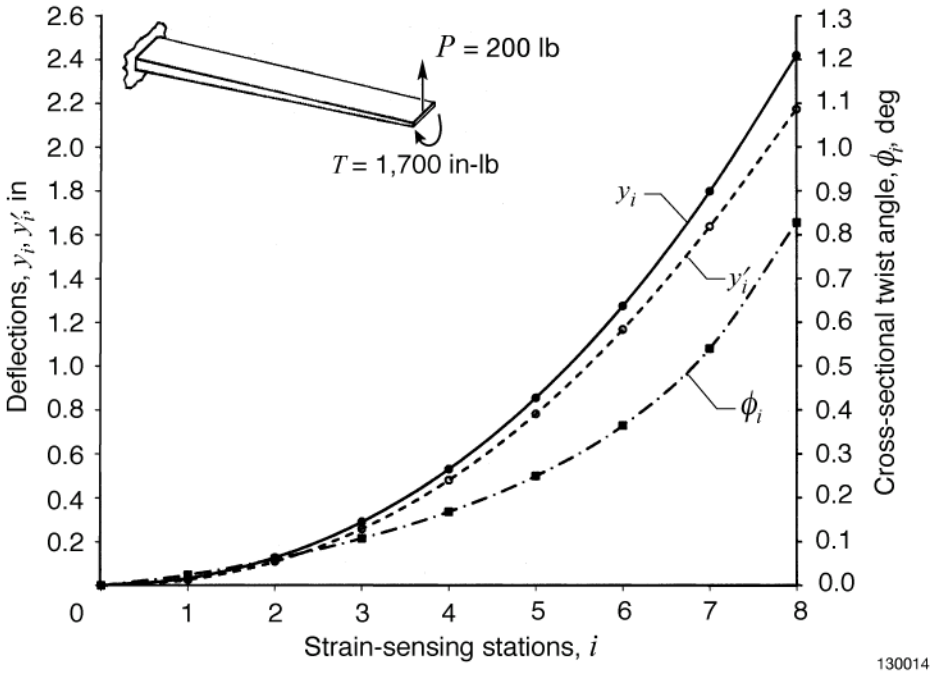

Figure 15. SPAR-generated deflections, $\{y_i, y_i'\}$, and cross-sectional twist angle, ϕ_i, for depth-tapered un-swept wing box subjected to point load, P = 200 lb, and clockwise torque, $T = 100 \times w$ = 1,700 in-lb, at wing box tip.

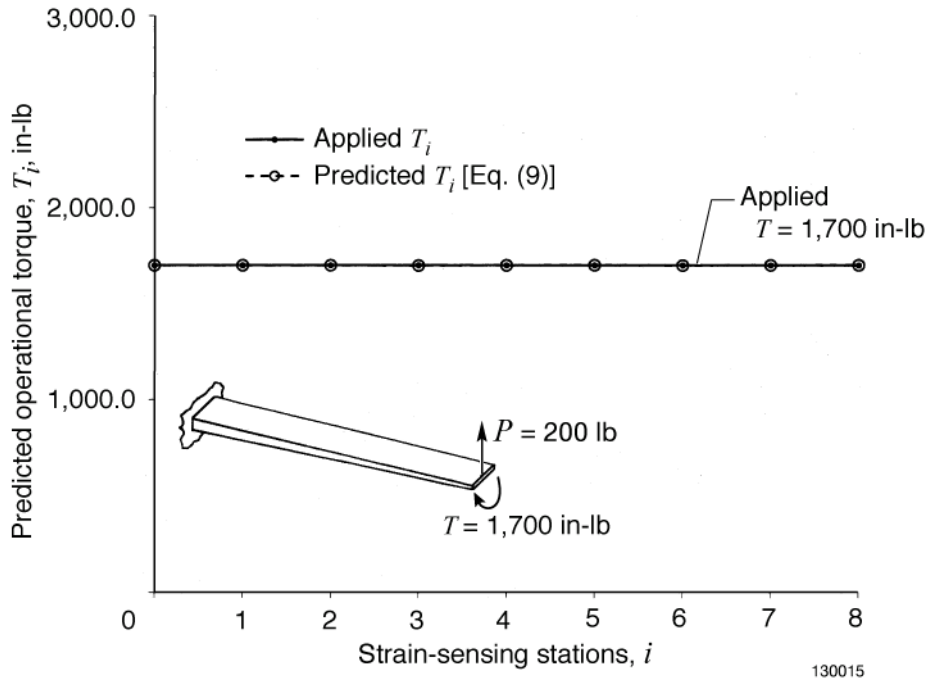

Figure 16. Plots of estimated operational torques, T_i, for depth-tapered un-swept wing box subjected to point load, P = 200 lb, and clockwise torque, $T = 100 \times w$ = 1,700 in-lb, at wing box tip.

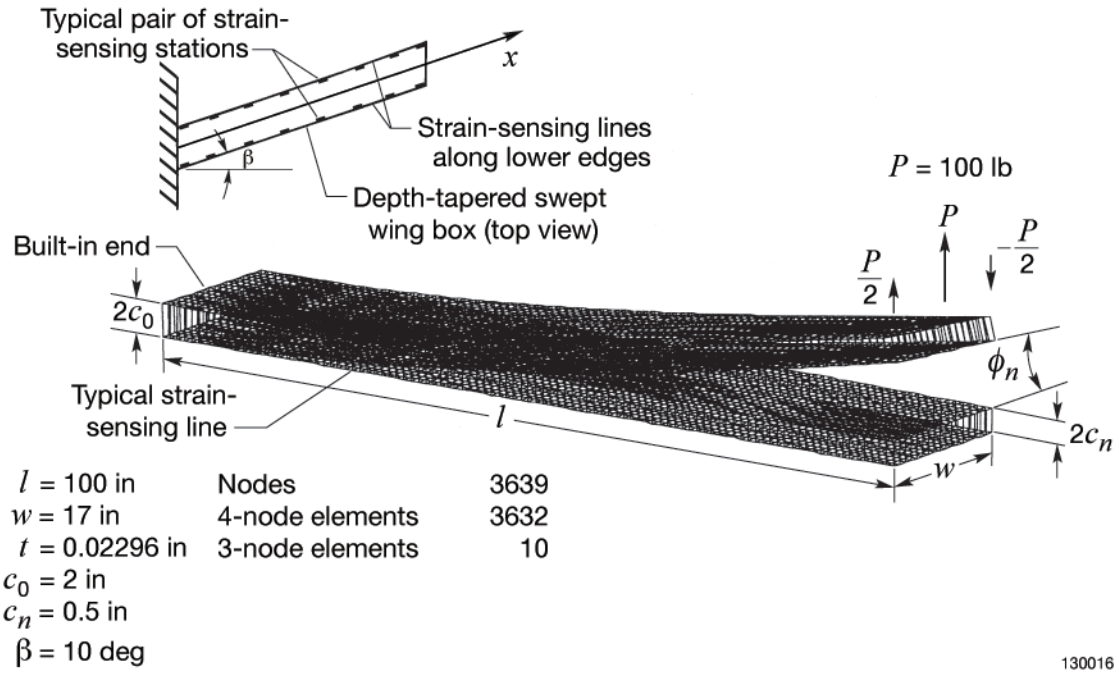

Figure 17. SPAR finite-element model generated for depth-tapered swept wing box subjected to a typical combined bending load, P = 100 lb, and clockwise torque, $T = 50 \times w$ = 850 in-lb at wing box tip.

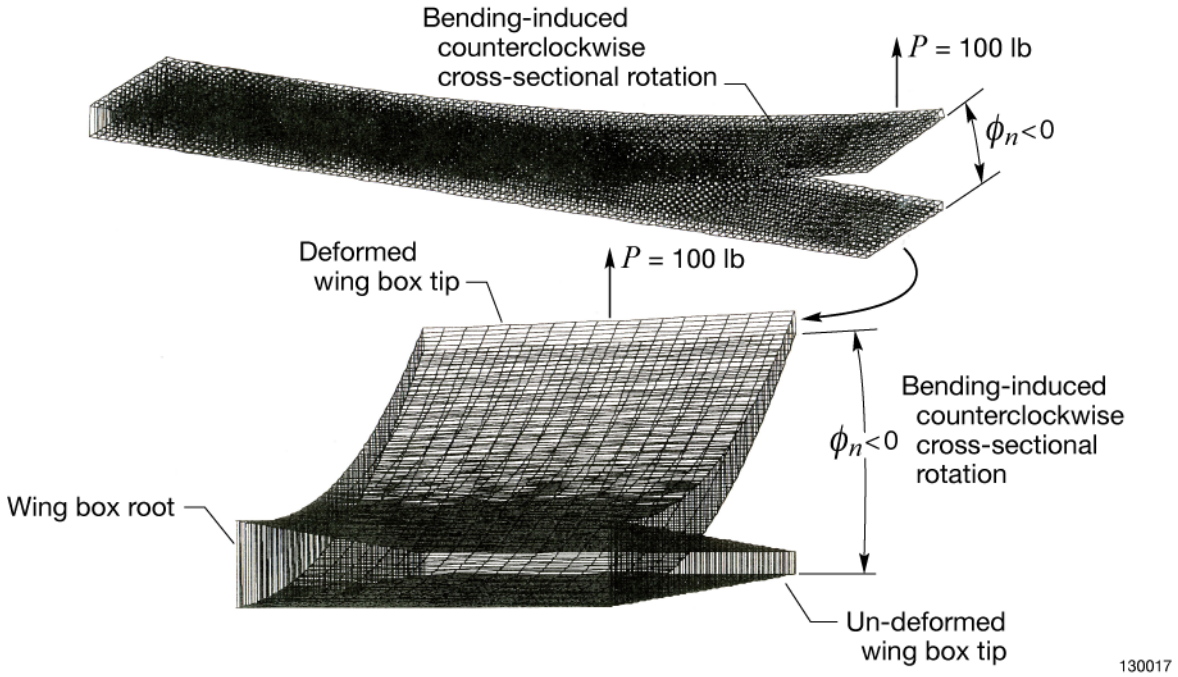

Figure 18. Counterclockwise rotation (decreasing angle of attack) of depth-tapered swept wing box induced by bending load, P = 100 lb at wing box tip.

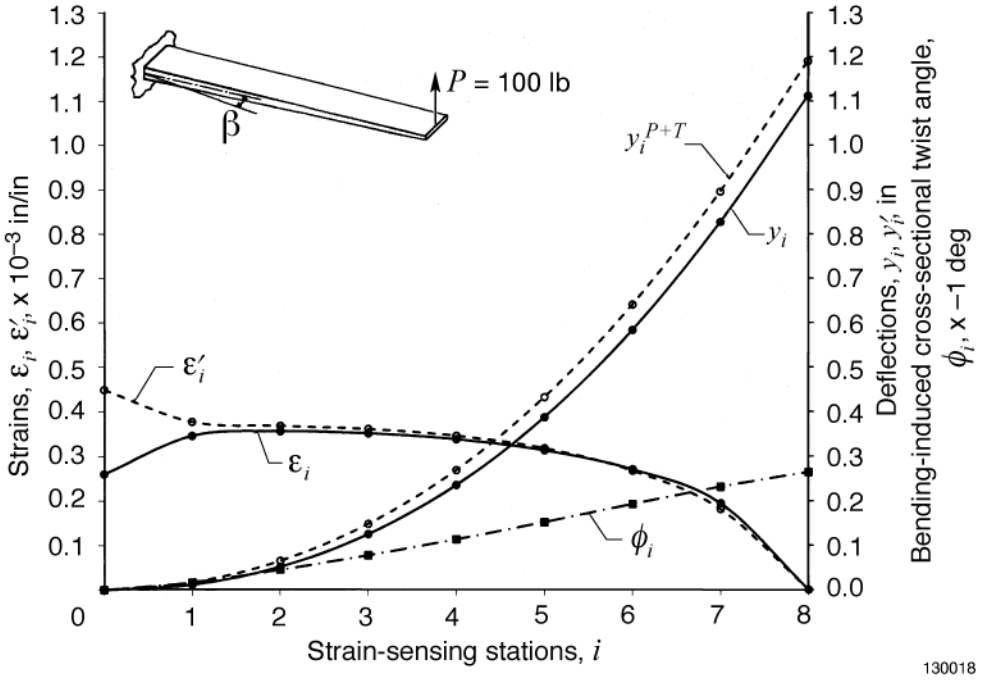

Figure 19. SPAR-generated surface bending strains, $\{\varepsilon_i, \varepsilon_i'\}$, deflections, $\{y_i, y_i'\}$, and bending induced cross-sectional twist angle, $\phi_n(< 0)$, for depth tapered swept wing box subjected to bending load, P = 100 lb, at wing box tip for determination of bending stiffness, $(EI)_i$.

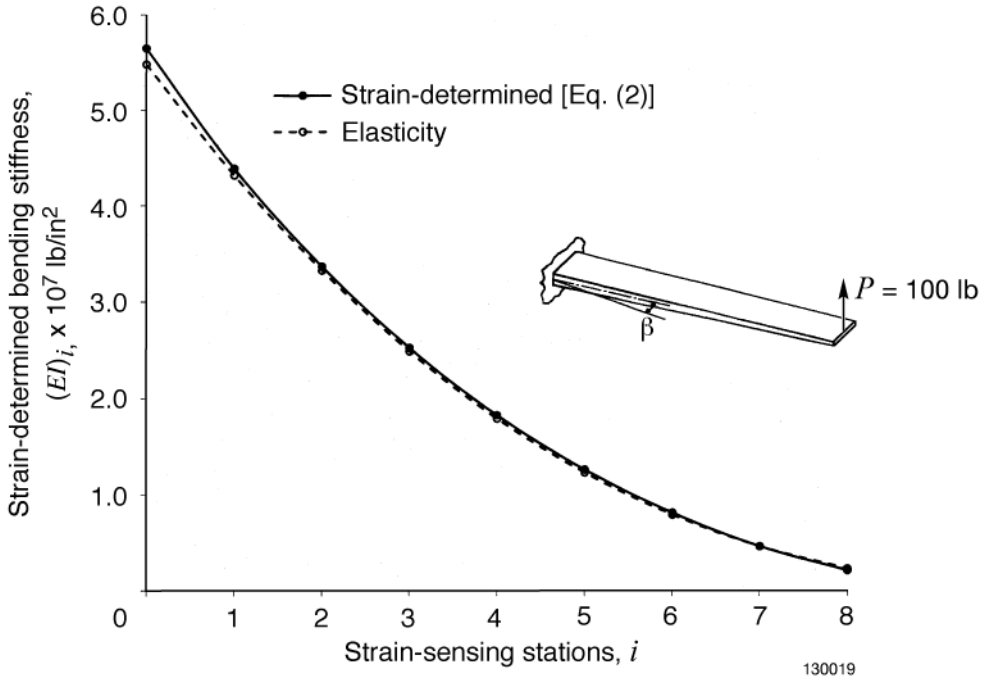

Figure 20. Span-wise plots of strain-determined apparent bending stiffness, $(EI)_i$, for depth-tapered un-swept wing box.

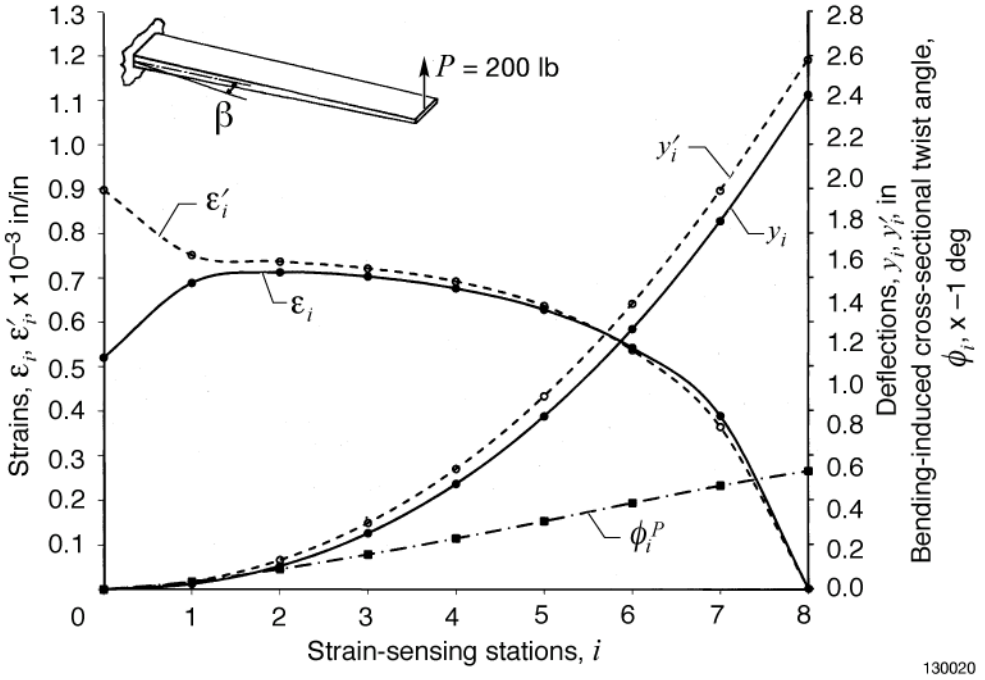

Figure 21. SPAR-generated surface bending strains, $\{\varepsilon_i, \varepsilon_i'\}$, deflections, $\{y_i, y_i'\}$, and bending induced cross-sectional twist angles, $\phi_i^P (< 0)$, for depth-tapered swept wing box subjected to point load, P = 200 lb, at wing box tip.

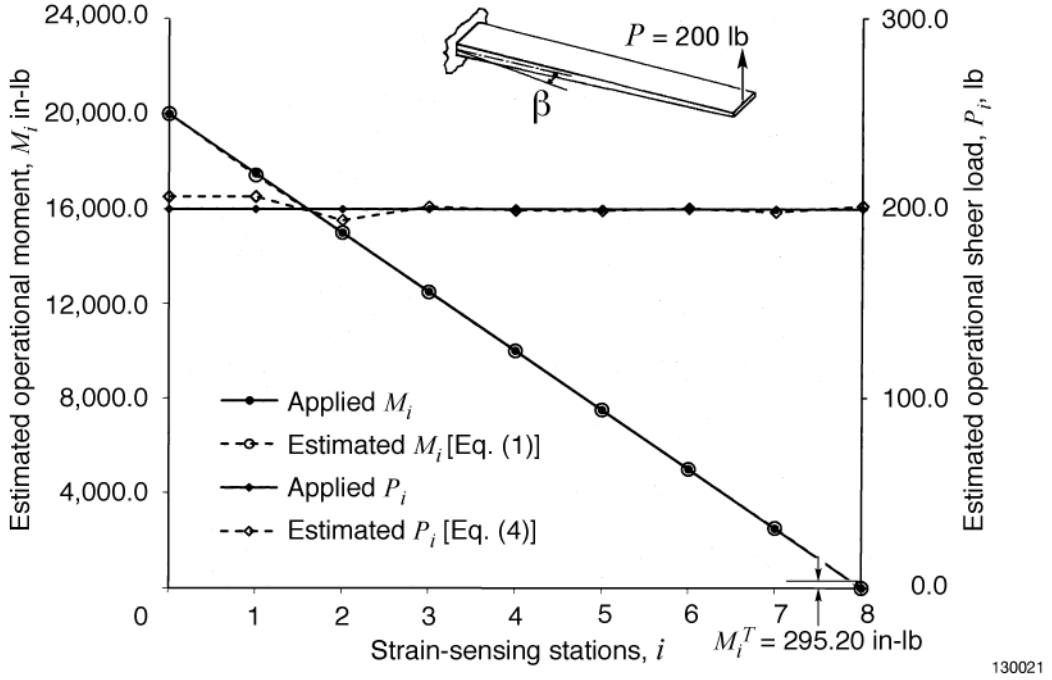

Figure 22. Plots of estimated operational moments and shear load, $\{M_i, P_i\}$, for depth-tapered swept wing box subjected to point load, P = 200 lb, at wing box tip.

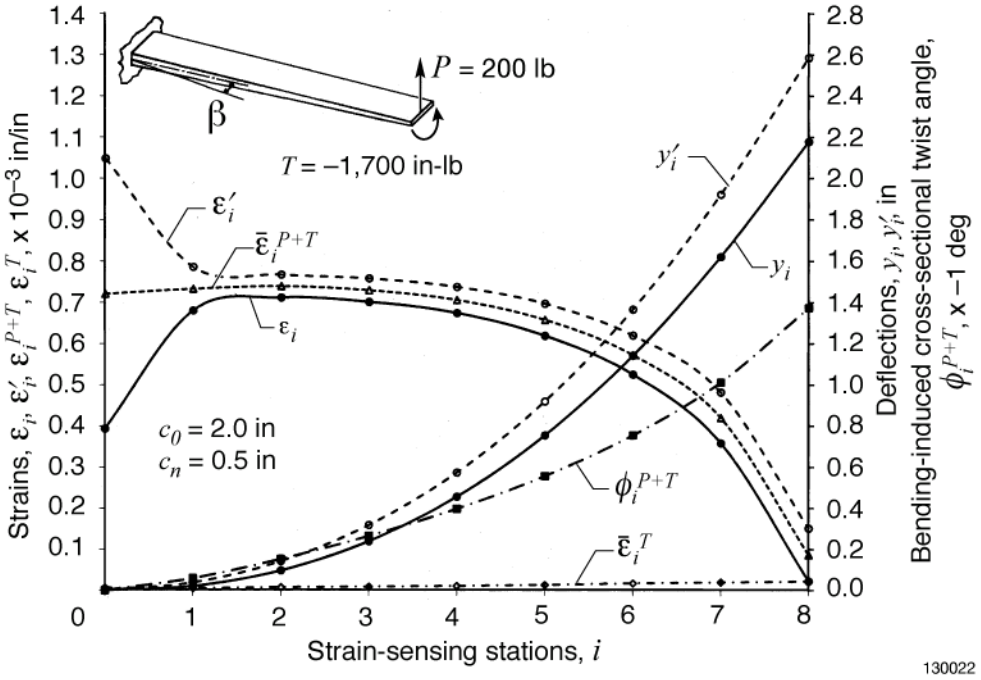

Figure 23. SPAR-generated surface bending strains $\{\varepsilon_i, \varepsilon_i', \bar{\varepsilon}_i^{P+T}\}$ deflections, $\{y_i, y_i'\}$, and cross-sectional twist angles, ϕ_i^{P+T}, for depth-tapered swept wing box subjected to point load, P = 200 lb, and counterclockwise torque, $T = -100 \times w = -1{,}700$ in-lb, at wing box tip ε_i^T; is induced by $T = -100 \times w = -1{,}700$ in-lb only.

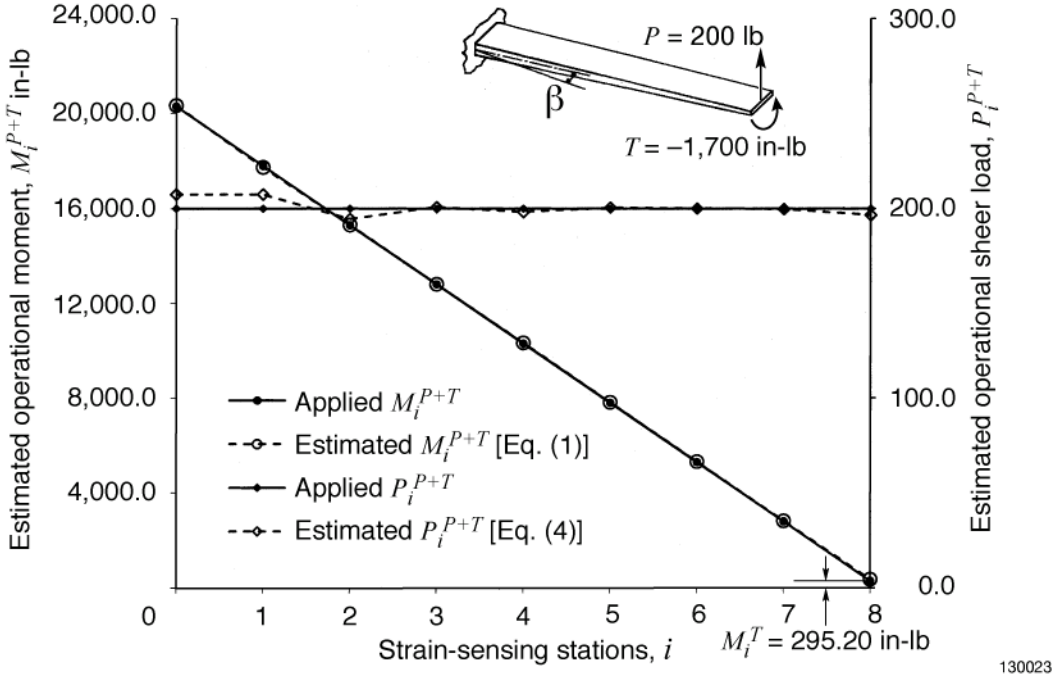

Figure 24. Plots of estimated operational moments and shear loads, $\{M_i, P_i\}$, for depth-tapered swept wing box subjected to point load, P = 200 lb, and counterclockwise torque, $T = -100 \times w = -1{,}700$ in-lb, at wing box tip.

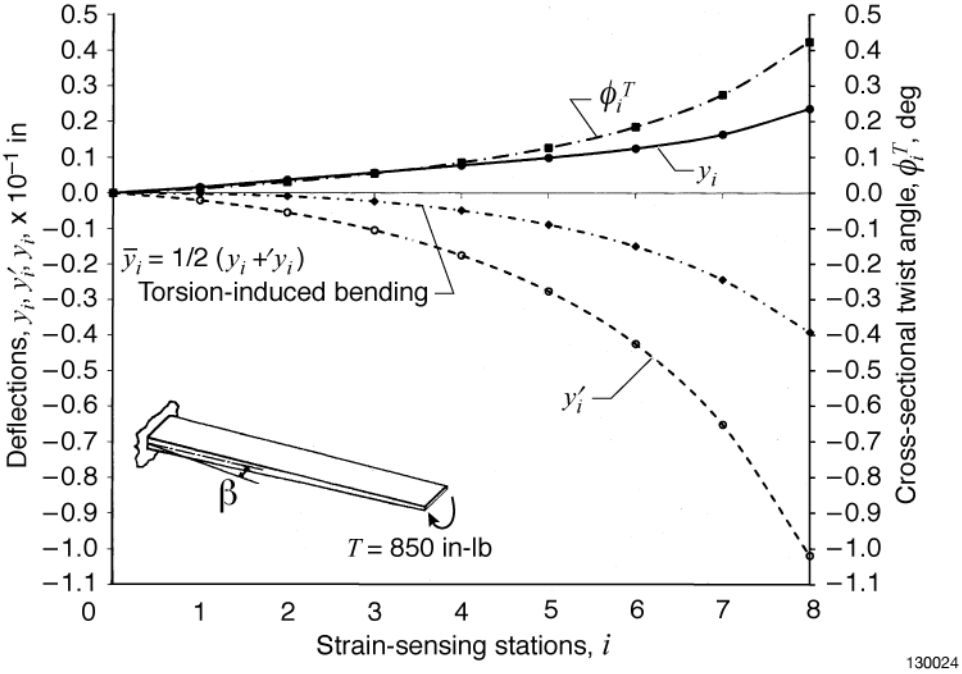

Figure 25. SPAR-generated deflections, $\{y_i,\ y_i'\}$, and cross-sectional twist angle, ϕ_i^T, for depth-tapered swept wing box subjected to clockwise torque, $T = 50 \times w = 850$ in-lb, at wing box tip for determination of torsion stiffness, $(GK)_i$.

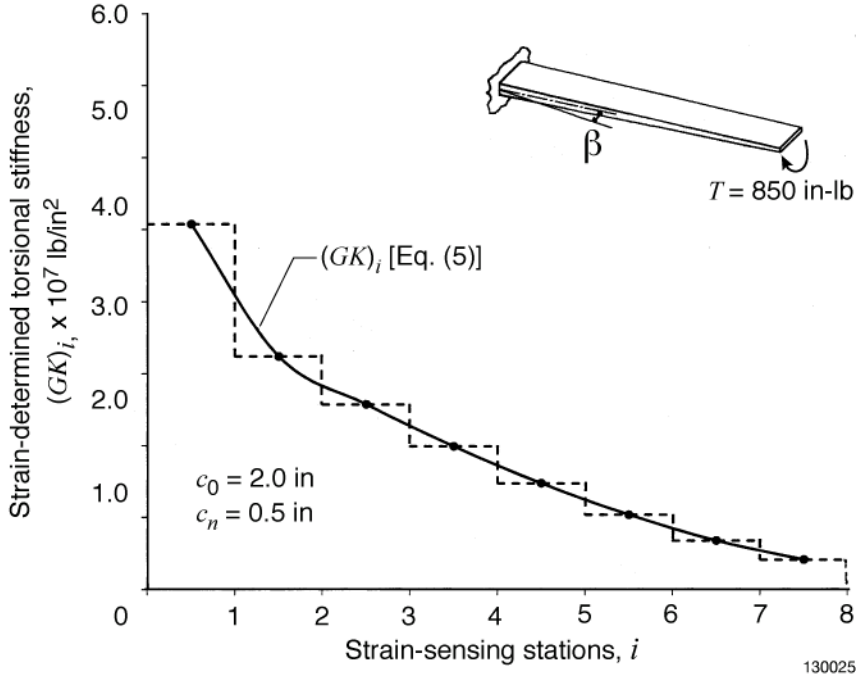

Figure 26. Span-wise plots of strain-determined torsional stiffness, $(GK)_i$, for depth-tapered swept wing box.

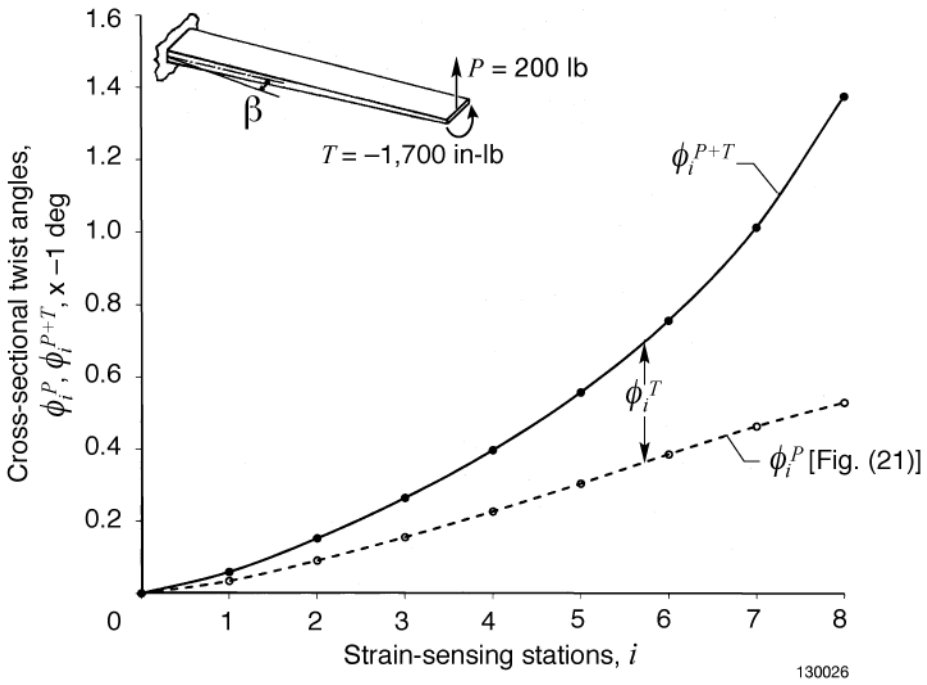

Figure 27. SPAR-generated cross-sectional twist angles, ϕ_i^{P+T}, for depth-tapered swept wing box subjected to point load, P = 200 lb, and counterclockwise torque, $T = -100 \times w = -1{,}700$ in-lb, at wing box tip; ϕ_i^P is induced by P = 200 in-lb only.

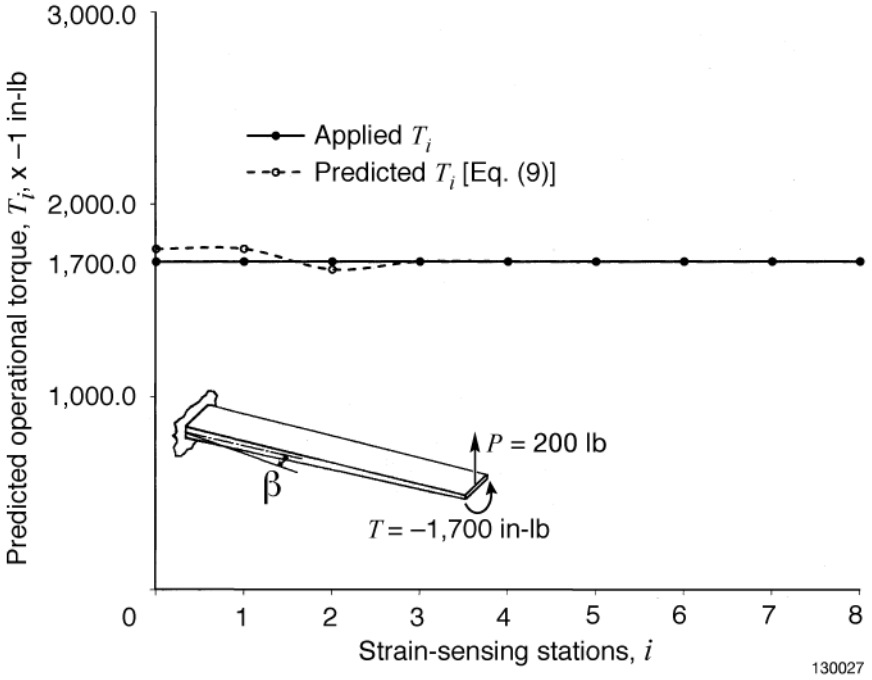

Figure 28. Plots of estimated operational torques, T_i , for depth-tapered swept wing box subjected to point load, P = 200 lb, and clockwise torque, $T = -100 \times w = -1{,}700$ in-lb, at wing box tip.

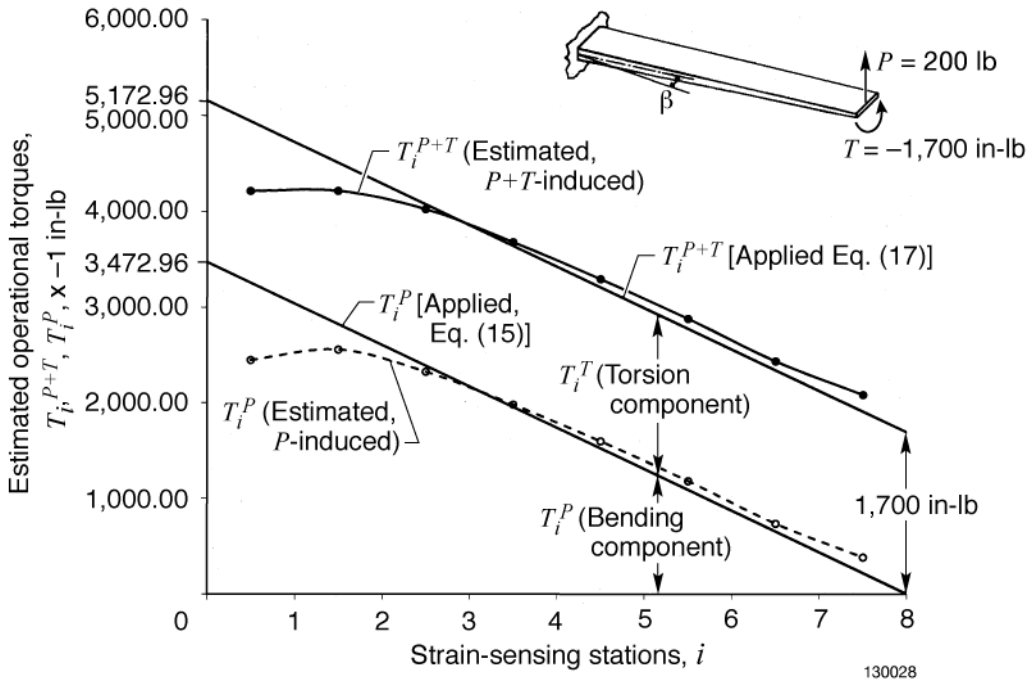

Figure 29. Plots of estimated operational torques, T_i^{P+T}, for depth-tapered swept wing box subjected to point load, P = 200 lb, and clockwise torque, $T = -100 \times w = -1{,}700$ in-lb, at wing box tip; operational torque components, T_i^P, induced by P = 200 lb only.

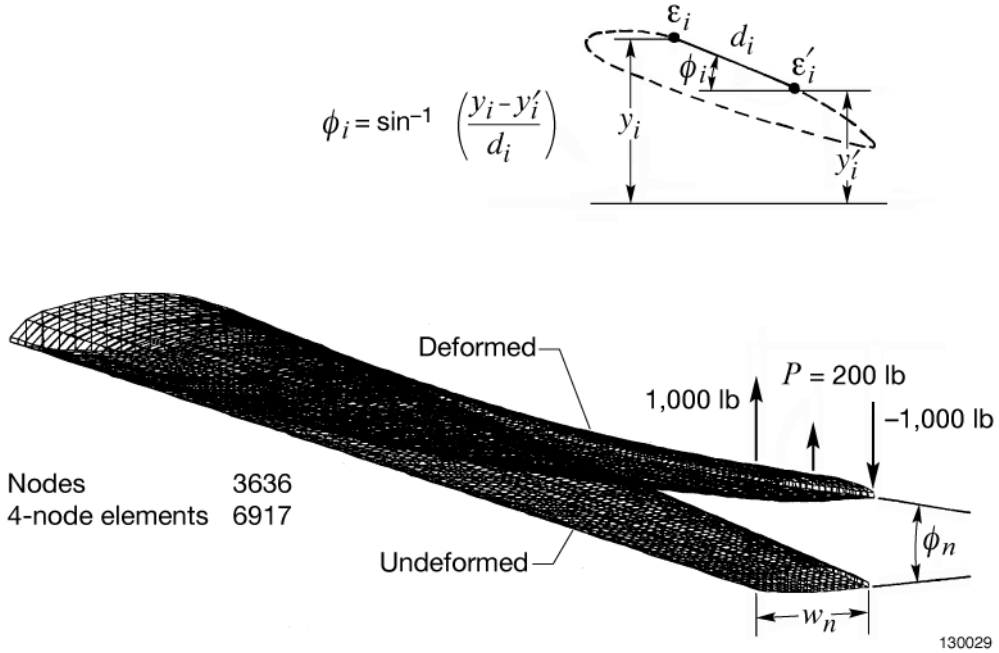

Figure 30. SPAR finite-element model generated for doubly-tapered generic long-span wing subjected to combined bending and torsion; P = 200 lb, T=2,000×w_n in-lb.

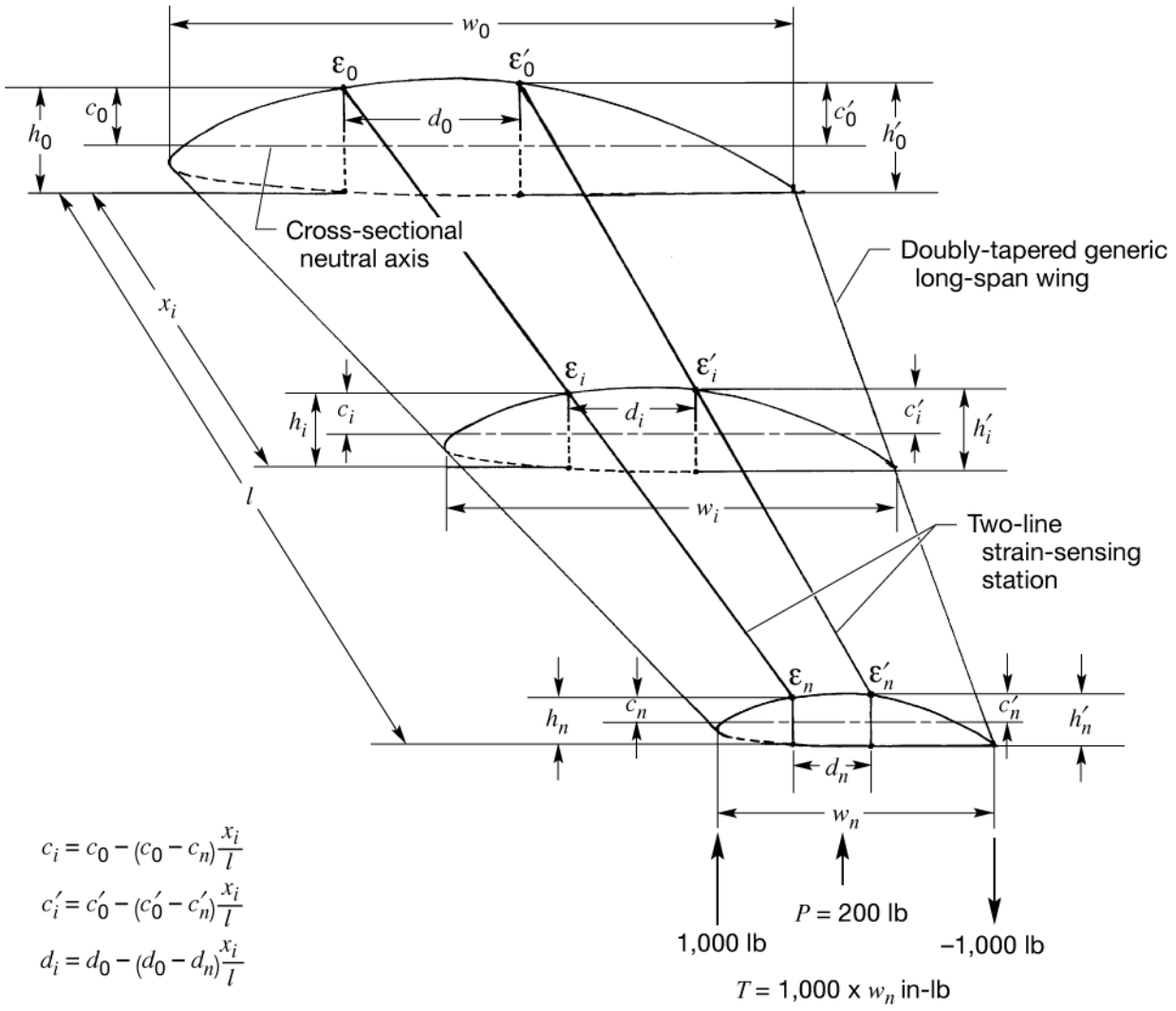

Figure 31. Two-line strain-sensing system on upper surface of doubly-tapered generic long-span wing for sensing surface bending strains.

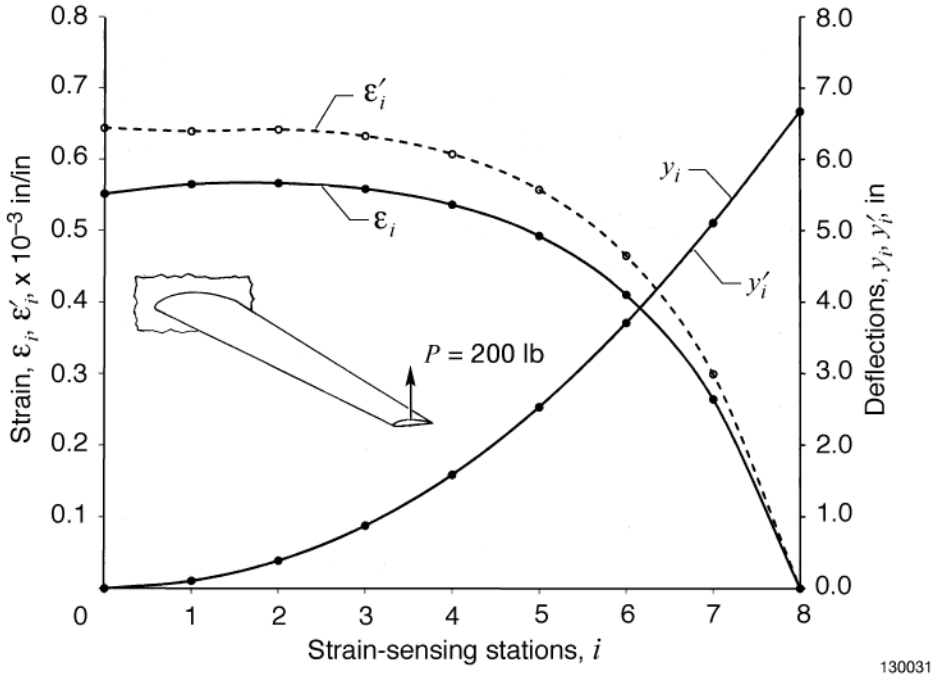

Figure 32. SPAR-generated surface bending strains, $\{\varepsilon_i, \varepsilon_i'\}$, deflections, $\{y_i, y_i'\}$, for doubly-tapered generic long-span wing subjected to point load, P = 200 lb, at wing tip for determination of bending stiffness, $(EI)_i$.

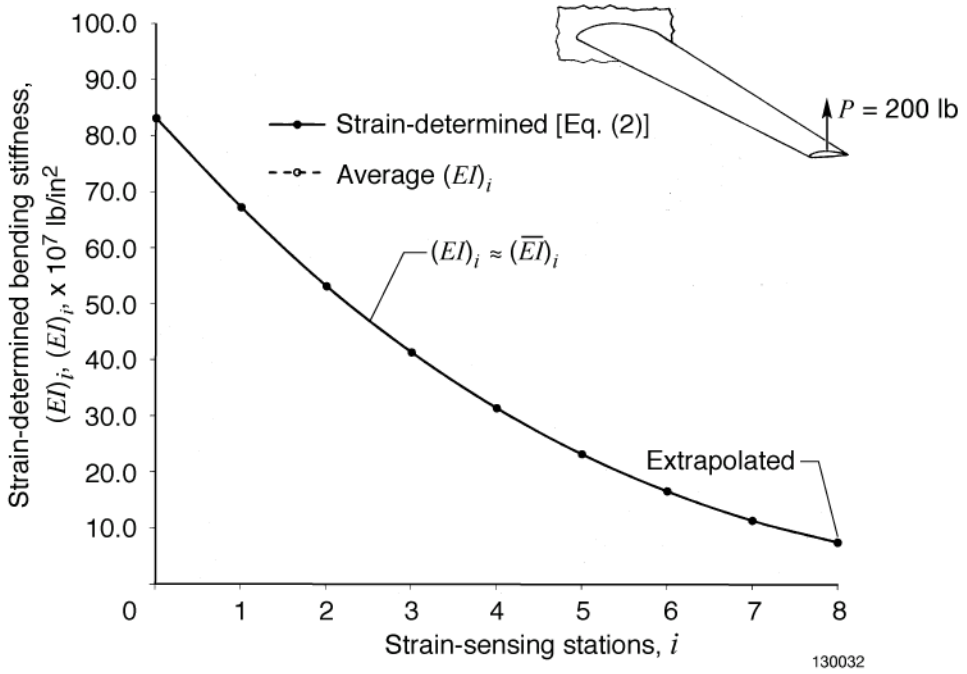

Figure 33. Span-wise plots of strain-determined bending stiffness, $\{(EI)_i, (\overline{EI})_i\}$ for doubly-tapered generic long-span wing.

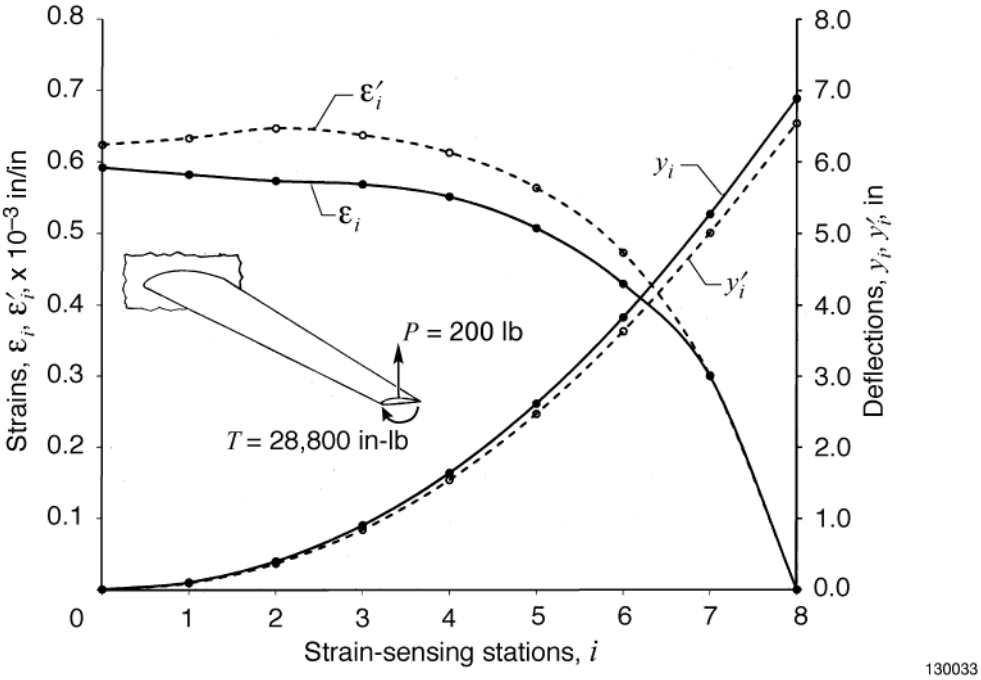

Figure 34. SPAR-generated surface bending strains, $\{\varepsilon_i, \varepsilon_i'\}$, and deflections, $\{y_i, y_i'\}$, for doubly-tapered generic long-span wing subjected to point load, P = 200 lb, and clockwise torque, $T = 1{,}000 \times w_n$ = 28,800 in-lb, at wing tip.

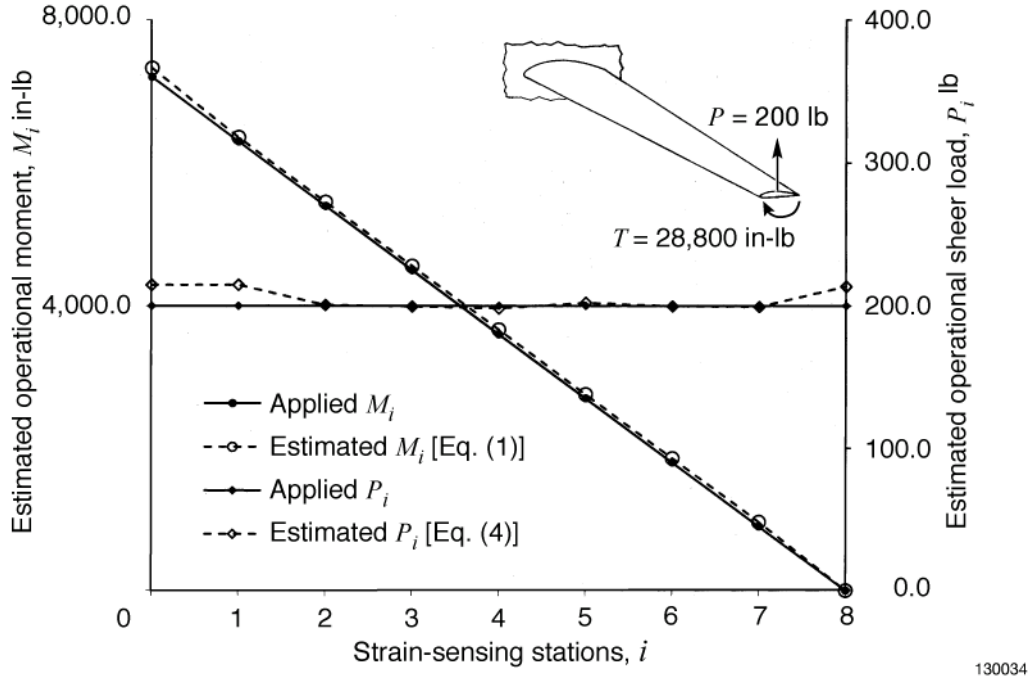

Figure 35. Plots of estimated operational moments and shear loads, $\{M_i, P_i\}$, for doubly-tapered generic long-span wing subjected to point load, P = 200 lb, and clockwise torque, $T = 1{,}000 \times w_n$ = 28,800 in-lb, at wing tip.

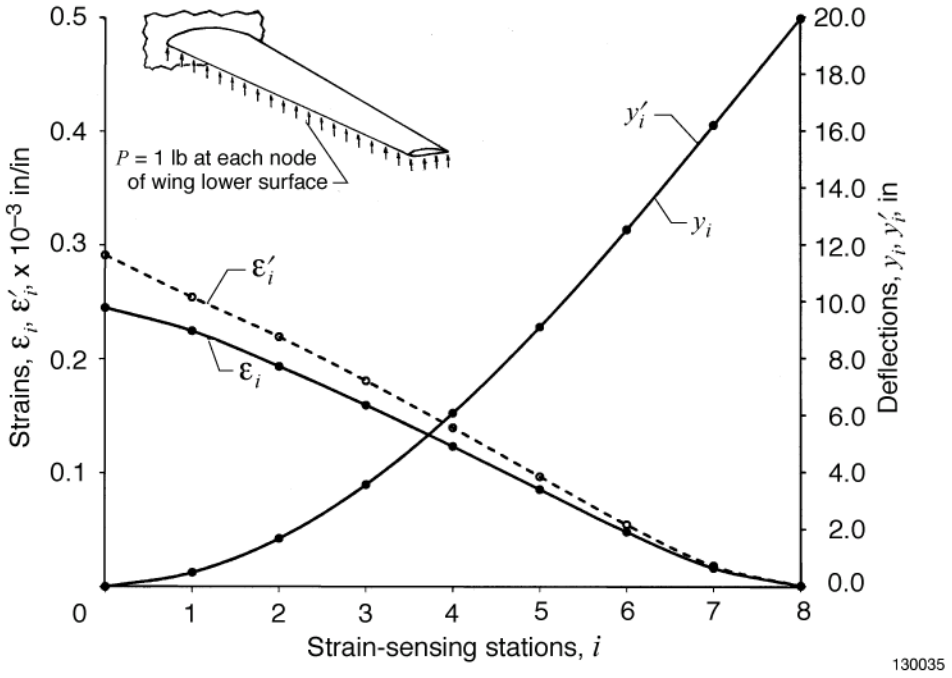

Figure 36. SPAR-generated surface bending strains, $\{\varepsilon_i, \varepsilon_i'\}$, and deflections, $\{y_i, y_i'\}$, for doubly-tapered generic long-span wing subjected to distributed load of P = 1 lb at each lower surface node of SPAR model.

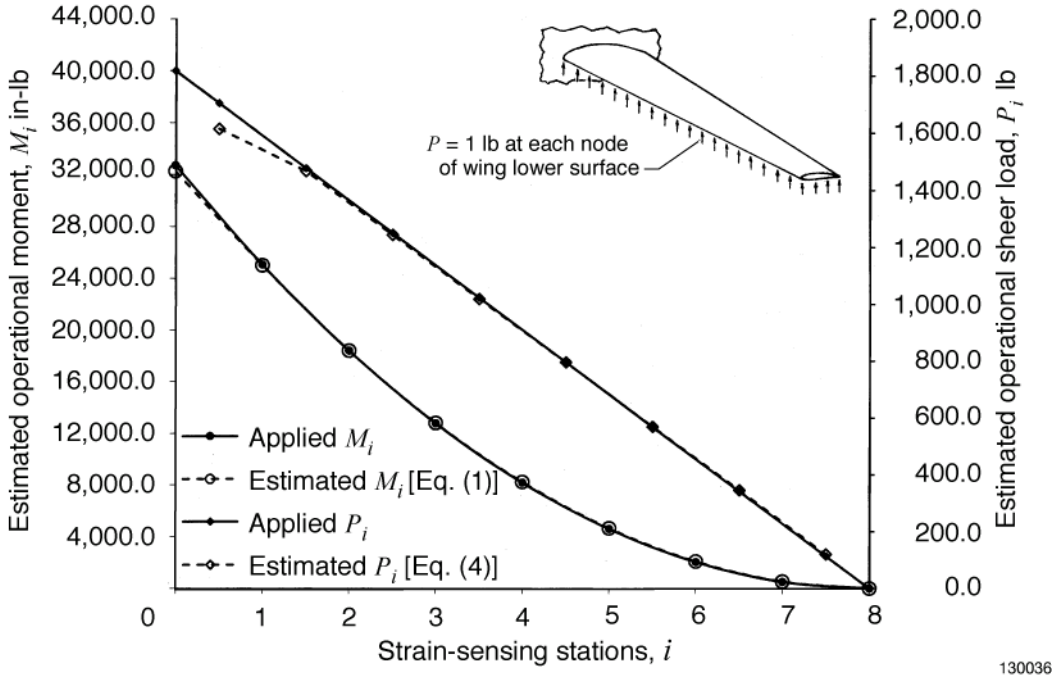

Figure 37. Comparison of applied and estimated operational moments and shear loads, $\{M_i, P_i\}$, for doubly-tapered generic long-span wing subjected to distributed load of P = 1 lb at each lower surface node of SPAR model.

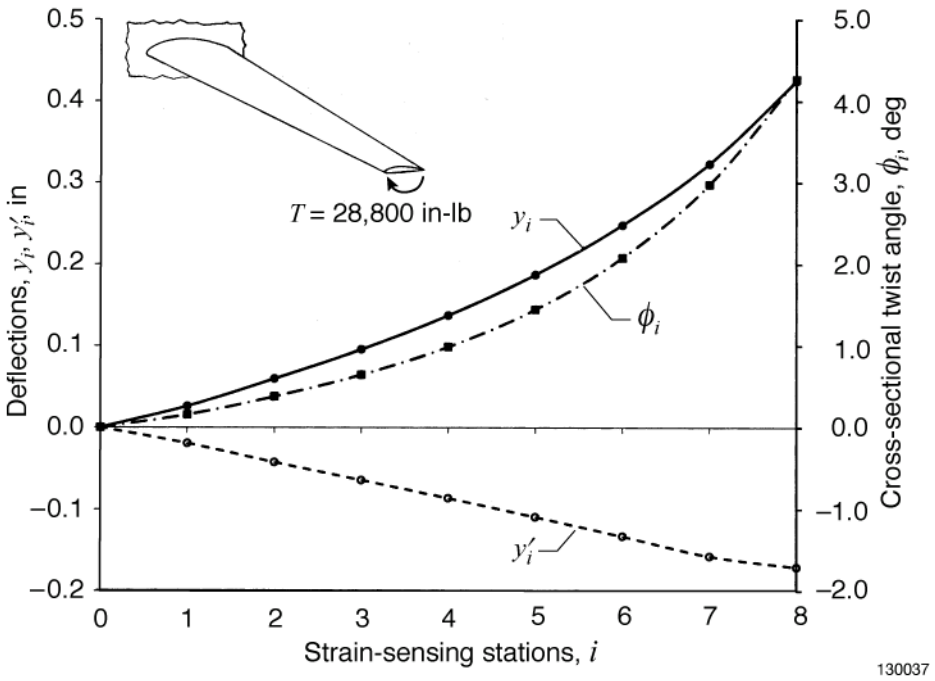

Figure 38. SPAR-generated deflections, $\{y_i, y_i'\}$, and cross-sectional twist angles, ϕ_i, for doubly-tapered generic long-span wing subjected to clockwise torque, $T = 1{,}000 \times w_n = 28{,}800$ in-lb, at wing tip for determination of torsion stiffness, $(GK)_i$.

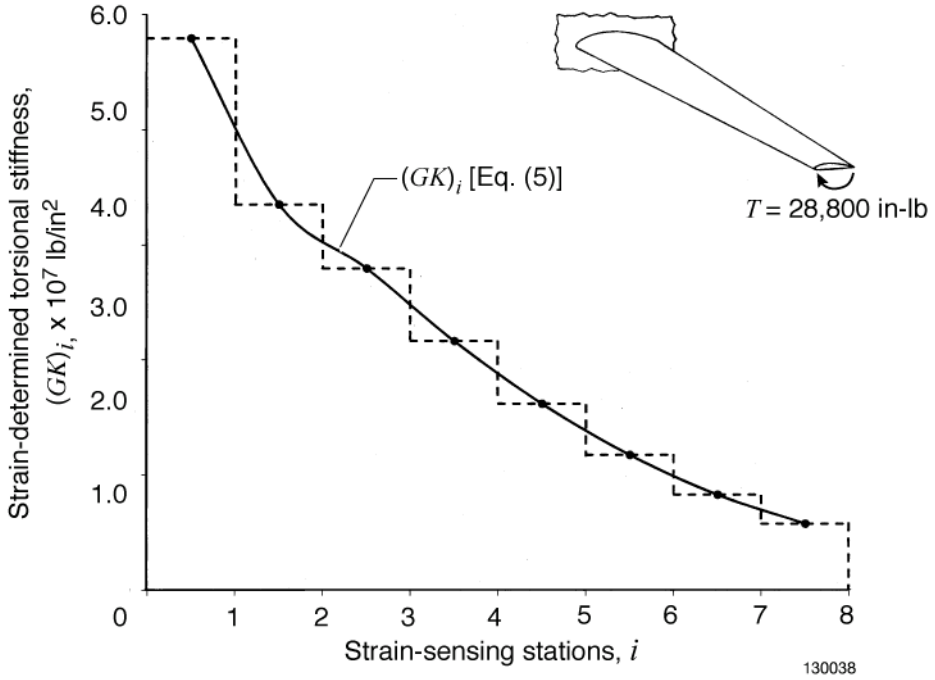

Figure 39. Span-wise plot of strain-determined torsion stiffness, $(GK)_i$, for doubly-tapered generic long-span wing.

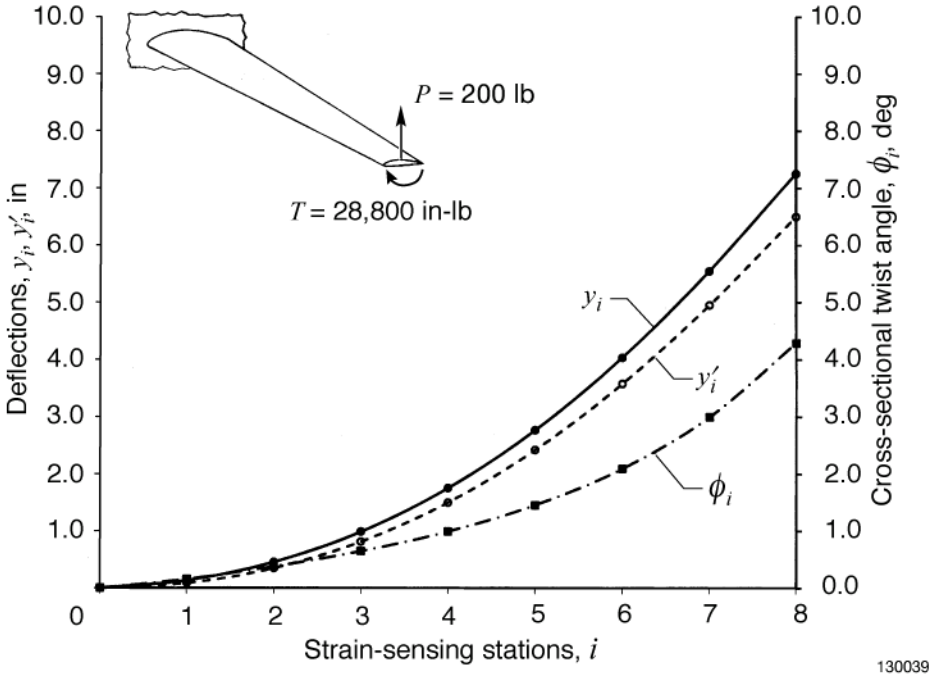

Figure 40. SPAR-generated deflections, $\{y_i, y_i'\}$, and cross-sectional twist angles, ϕ_i, for doubly-tapered generic long-span wing subjected to point load, P = 200 lb, and clockwise torque, $T = 1{,}000 \times w_n = 28{,}800$ in-lb, at wing tip.

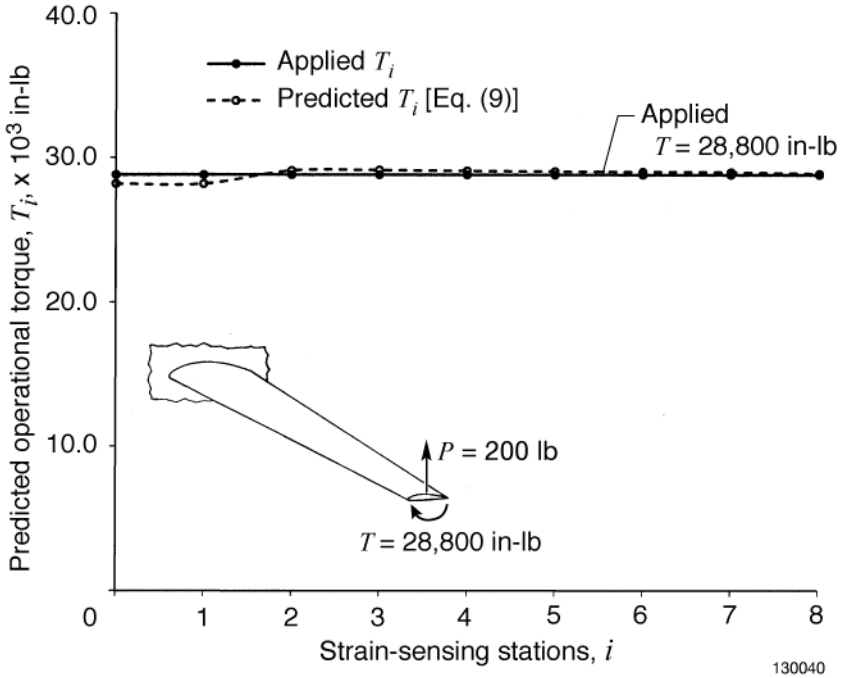

Figure 41. Comparison of applied and estimated operational torques, T_i, for doubly-tapered generic long-span wing subjected to point load, P = 200 lb, and clockwise torque, $T = 1{,}000 \times w_n = 28{,}800$ in-lb, at wing tip.

APPENDIX A

SUMMARY OF DIFFERENT DISPLACEMENT TRANSFER FUNCTIONS

Different Displacement Transfer Functions developed earlier (refs. 1 and 2) for nonuniform and slightly nonuniform and uniform straight cantilever beams, are summarized in the following for comparison of mathematical functional forms:

1. Nonuniform Displacement Transfer Functions ($c_i \neq c_{i-1}$) (ref. 2):

$$y_i = \underbrace{(\Delta l)^2 \sum_{j=1}^{i} \left\{ \frac{\varepsilon_{j-1} - \varepsilon_j}{2(c_{j-1} - c_j)} - \frac{\varepsilon_{j-1} c_j - \varepsilon_j c_{j-1}}{(c_{j-1} - c_j)^3} \left[c_j \log_e \frac{c_j}{c_{j-1}} + (c_{j-1} - c_j) \right] \right\}}_{\text{Contributions from deflection terms}}$$
$$+ \underbrace{(\Delta l)^2 \sum_{j=1}^{i-1} \left\{ (i-j) \left[\frac{\varepsilon_{j-1} - \varepsilon_j}{c_{j-1} - c_j} + \frac{\varepsilon_{j-1} c_j - \varepsilon_j c_{j-1}}{(c_{j-1} - c_j)^2} \log_e \frac{c_j}{c_{j-1}} \right] \right\}}_{\text{Contributions from slope terms}} + \underbrace{y_0 + (i)\Delta l \tan\theta_0}_{=0 \text{ for cantilever beams}} \tag{A1}$$

$(i = 1,2,3,\ldots n)$

Equation (A1) is not applicable to uniform beams because of a mathematical breakdown problem (that is, 0/0 at $c_i = c_{i-1} = c$).

2. Slightly Tapered Displacement Transfer Functions ($c_i/c_{i-1} \rightarrow 1$) (ref. 2):

$$y_i = \underbrace{\frac{(\Delta l)^2}{6} \sum_{j=1}^{i} \left\{ \frac{1}{c_{j-1}} \left[\left(3 - \frac{c_j}{c_{j-1}} \right) \varepsilon_{j-1} + \varepsilon_j \right] \right\}}_{\text{Contributions from deflection terms}} + \underbrace{\frac{(\Delta l)^2}{2} \sum_{j=1}^{i-1} \left\{ \frac{(i-j)}{c_{j-1}} \left[\left(2 - \frac{c_j}{c_{j-1}} \right) \varepsilon_{j-1} + \varepsilon_j \right] \right\}}_{\text{Contributions from slope terms}}$$
$$+ \underbrace{y_0 + \Delta l \tan\theta_0}_{=0 \text{ for cantilever beams}} \tag{A2}$$

$(i = 1,2,3,\ldots,n)$

which was obtained from equation (A1) by expanding the logarithmic terms in the neighborhood of $c_i/c_{i-1} \approx 1$.

3. First Order Displacement Transfer Function (ref. 7):

$$y_i = \underbrace{\frac{(\Delta l)^2}{12} \sum_{j=1}^{i} \frac{(\Delta l)^2}{c_{j-1}} \left[\left(5 - \frac{c_j}{c_{j-1}} \right) \varepsilon_{j-1} + \left(3 - \frac{c_j}{c_{j-1}} \right) \varepsilon_j \right]}_{\text{Contributions from deflection terms}}$$
$$+ \underbrace{\frac{(\Delta l)^2}{6} \sum_{j=1}^{i-1} \frac{(i-j)}{c_{i-1}} \left[\left(4 - \frac{c_j}{c_{j-1}} \right) \varepsilon_{j-1} + \left(5 - 2\frac{c_j}{c_{j-1}} \right) \varepsilon_j \right]}_{\text{Contributions from slope terms}} + \underbrace{y_0 + \Delta l \tan\theta_0}_{=0 \text{ for cantitever beams}} \tag{A3}$$

$(i = 1,2,3,\ldots n)$

4. Second Order Displacement Transfer Function (ref. 7):

$$y_i = \underbrace{\frac{(\Delta l)^2}{60}\sum_{j=1}^{i}\frac{1}{c_{j-1}}\left\{\left[27-9\frac{c_j}{c_{j-1}}+2\left(\frac{c_j}{c_{j-1}}\right)^2\right]\varepsilon_{j-1}+\left[18-11\frac{c_j}{c_{j-1}}+3\left(\frac{c_j}{c_{j-1}}\right)^2\right]\varepsilon_j\right\}}_{\text{Contributions from deflection terms}}$$

$$+\underbrace{\frac{(\Delta l)^2}{12}\sum_{j=1}^{i-1}\frac{(i-j)}{c_{j-1}}\left\{\left[9-4\frac{c_j}{c_{j-1}}+\left(\frac{c_j}{c_{j-1}}\right)^2\right]\varepsilon_{j-1}+\left[13-10\frac{c_j}{c_{j-1}}+3\left(\frac{c_j}{c_{j-1}}\right)^2\right]\varepsilon_j\right\}}_{\text{Contributions from slope terms}} \qquad \text{(A4)}$$

$$+\underbrace{y_0+(i)\Delta l\tan\theta_0}_{=0\text{ for cantilever beams}}$$

$$(i = 1,2,3,\ldots,n)$$

5. Uniform Displacement Transfer Function ($c_i = c_{i-1} = c$) (refs. 1, 2):

$$y_i = \underbrace{\frac{(\Delta l)^2}{6c}\sum_{j=1}^{i}(2\varepsilon_{j-1}+\varepsilon_j)}_{\text{Contributions from deflection terms}} + \underbrace{\frac{(\Delta l)^2}{2c}\sum_{j=1}^{i-1}(i-j)(\varepsilon_{j-1}+\varepsilon_j)}_{\text{Contributions from slope terms}} + \underbrace{y_0+\Delta l\tan\theta_0}_{=0\text{ for cantilever beams}} \qquad \text{(A5)}$$

$$(i = 1,2,3,\ldots,n)$$

Equation (A5) is the degenerated form of equations (A2), (A3), and (A4) for the uniform beam case ($c_i = c_{i-1} = c$).

APPENDIX B

FLOW CHART FOR STRUCTURAL STIFFNESS AND OPERATIONAL LOADS ESTIMATIONS USING DISTRIBUTED SURFACE STRAINS

(cf., U.S. Patent No. 7,715,994, issued May 11, 2010)

Flow chart for the determinations of bending and torsion stiffness, $\{(EI)_i, (GK)_i\}$, for estimations of operational moments, shear loads, and torques, $\{M_i, P_i, T_i\}$, using two-line strain-sensing system (fig. B1) is presented below.

Step 1–Determinations of $\{(EI)_i, (GK)_i\}$ Using Strains Induced by Simple (Bending, Torsion) Tests:

Simple bending test — Averaged surface strains and depth factors — Determination of $(EI)_i$

$$M_i \text{ (specified)} \rightarrow \left\{ \bar{\varepsilon}_i = \frac{\varepsilon_i + \varepsilon_i'}{2} \; ; \; \bar{c}_i = \frac{c_i + c_i'}{2} \right\} \rightarrow (EI)_i = M_i \frac{\bar{c}_i}{\bar{\varepsilon}_i}$$

Simple torsion test — Surface strains — Deflections — Cross-sectional twist angles — Determination of $(GK)_i$

$$T_i \text{ (specified)} \rightarrow \{\varepsilon_i, \varepsilon_i'\} \rightarrow \{y_i, y_i'\}^* \rightarrow \phi_i = \sin^{-1}\left(\frac{y_i - y_i'}{d_i}\right) \rightarrow (GK)_i = \frac{T_i(\Delta l)}{\phi_i - \phi_{i-1}}$$

Step 2--Estimations of $\{M_i, P_i, T_i\}$ for Other Types of Loading Based on Strain-Determined $\{(EI)_i, (GK)_i\}$:

Estimations of M_i — Estimations of P_i

$$\text{For } \begin{Bmatrix} M_i \\ P_i \end{Bmatrix}: \begin{Bmatrix} c_i, \; c_i' \\ \varepsilon_i, \; \varepsilon_i' \end{Bmatrix} \rightarrow \left\{ \bar{c}_i = \frac{c_i + c_i'}{2}; \bar{\varepsilon}_i = \frac{\varepsilon_i + \varepsilon_i'}{2} \right\} \rightarrow M_i = (EI)_i \frac{\bar{\varepsilon}_i}{\bar{c}_i} \rightarrow$$

$$P_i = \frac{1}{\Delta l}\left[(EI)_{i-1} \frac{\bar{\varepsilon}_{i-1}}{\bar{c}_{i-1}} - (EI)_i \frac{\bar{\varepsilon}_i}{\bar{c}_i} \right]$$

Calculations of ϕ_i — Estimations of T_i

$$\text{For } T_i: \quad \{\varepsilon_i, \varepsilon_i'\} \rightarrow \{y_i, y_i'\}^* \rightarrow \phi_i = \sin^{-1}\left(\frac{y_i - y_i'}{d_i}\right) \rightarrow T_i = (GK)_i \frac{\phi_i - \phi_{i-1}}{\Delta l}$$

---

* Deflections, $\{y_i, y_i'\}$ can be calculated from any of the Displacement Transfer Functions (Appendix A) using surface strains, $\{\varepsilon_i, \varepsilon_i'\}$, as inputs. For example, when the Nonuniform Displacement Transfer Functions are used, $\{y_i, y_i'\}$ have the following forms:

For front strain-sensing line:

$$y_i = \underbrace{(\Delta l)^2 \sum_{j=1}^{i} \left\{ \frac{\varepsilon_{j-1} - \varepsilon_j}{2(c_{j-1} - c_j)} - \frac{\varepsilon_{j-1} c_j - \varepsilon_j c_{j-1}}{(c_{j-1} - c_j)^3} \left[c_j \log_e \frac{c_j}{c_{j-1}} + (c_{j-1} - c_j) \right] \right\}}_{\text{Contributions from deflection terms}}$$
$$+ \underbrace{(\Delta l)^2 \sum_{j=1}^{i-1} \left\{ (i-j) \left[\frac{\varepsilon_{j-1} - \varepsilon_j}{c_{j-1} - c_j} + \frac{\varepsilon_{j-1} c_j - \varepsilon_j c_{j-1}}{(c_{j-1} - c_j)^2} \log_e \frac{c_j}{c_{j-1}} \right] \right\}}_{\text{Contributions from slope terms}} + \underbrace{y_0 + (i)\Delta l \tan \theta_0}_{=0 \text{ for cantilever beams}} \quad (B1)$$

$(i = 1,2,3,\ldots,n)$

For rear strain-sensing line:

$$y_i = \underbrace{(\Delta l)^2 \sum_{j=1}^{i} \left\{ \frac{\varepsilon'_{j-1} - \varepsilon'_j}{2(c'_{j-1} - c'_j)} - \frac{\varepsilon'_{j-1} c'_j - \varepsilon'_j c'_{j-1}}{(c'_{j-1} - c'_j)^3} \left[c'_j \log_e \frac{c'_j}{c'_{j-1}} + (c'_{j-1} - c'_j) \right] \right\}}_{\text{Contributions from deflection terms}}$$
$$+ \underbrace{(\Delta l)^2 \sum_{j=1}^{i-1} \left\{ (i-j) \left[\frac{\varepsilon'_{j-1} - \varepsilon'_j}{c'_{j-1} - c'_j} + \frac{\varepsilon'_{j-1} c'_j - \varepsilon'_j c'_{j-1}}{(c'_{j-1} - c'_j)^2} \log_e \frac{c'_j}{c'_{j-1}} \right] \right\}}_{\text{Contribution from slope terms}} + \underbrace{y'_0 + (i)\Delta l \tan \theta'_0}_{=0 \text{ for cantilever beams}} \quad (B2)$$

$(i = 1,2,3,\ldots,n)$

Figure B1. Two-line strain-sensing system for sensing multiple surface strains for deformed shape calculations of a tapered cantilever wing box subjected to combined bending and torsion (ref. 2).

REFERENCES

1. Ko, William L., W. L. Richards, and Van T. Tran, *Displacement Theories for In-Flight Deformed Shape Predictions of Aerospace Structures*, NASA/TP-2007-214612, October 2007.

2. Ko, William L., and Van Tran Fleischer, *Further Development of Ko Displacement Theory for Deformed Shape Predictions of Nonuniform Aerospace Structures*, NASA/TP-2009-214643, September 2009.

3. Ko, William L., *Collection of Memoranda on Applications of Ko Displacement Theory to Deformed Shape Predictions of Aerospace Structures*, NASA BR-119, Aerostructures Branch, Dryden Flight Research Center, Edwards, CA, April 2008.

4. Ko, William L., W. L. Richards, and Van Tran Fleischer, *Applications of Ko Displacement Theory to the Deformed Shape Predictions of Doubly-Tapered Ikhana Wing*, NASA/TP-2009-214652, October 2009.

5. Ko, William L., and Van T. Fleischer, *Methods for In-Flight Wing Shape Predictions of Highly Flexible Unmanned Aerial Vehicles: Formulation of Ko Displacement Theory*, NASA/TP-2010-214656, April 2010.

6. Ko, William L., and Van Tran Fleischer, *Extension of Ko Straight-Beam Displacement Theory to Deformed Shape Predictions of Slender Curved Structures*, NASA/TP-2011-214567, April 2011.

7. Ko, William L., and Van Tran Fleischer, *First- and Second- Order Displacement Transfer Functions for Structural Shape Calculations Using Analytically Predicted Surface Strains*, NASA/TP-2011-215976, March 2012.

8. Ko, William L., and Van Tran Fleischer, *Improved Displacement Transfer Functions for Structure Deformed Shape Predictions Using Discretely Distributed Surface Strains,* NASA/TP-2012-216060, November 2012.

9. Ko, William L., and Van Tran Fleischer*, Large-Deformation Displacement Transfer Functions for Shape Predictions of Highly Flexible Slender Aerospace Structures*, NASA/TP-2013-unnumbered (to be published).

10. Ko, William L., and W. Lance Richards, *Method for Real-Time Structure Shape-Sensing,* U.S. Patent No. 7,520,176, issued April 21, 2009.

11. Richards, W. Lance, and William L. Ko, *Process for Using Surface Strain Measurements to Obtain Operational Loads for Complex Structures,* U.S. Patent No. 7,715,994, issued May 11, 2010.

12. Roark, Raymond J., *Formulas for Stress and Strain*, McGraw-Hill Book Company, Inc., New York, 1954.

13. Whetstone, W. D., *SPAR Structural Analysis System Reference Manual, System Level 13A,Vol. 1, Program Execution*, NASA CR-158970-1, December 1978.

14. Jutte, Christine, William L. Ko, Craig A. Stephens, John A. Bakalyar, W. Lance Richards, and Allen R. Parker, *Deformed Shape Calculation of a Full-Scale Wing Using Fiber Optic Strain Data from a Ground Loads Test*, NASA/TP-2011-215975, December 2011.